

Gradient-Based Multi-Component Topology Optimization for Manufacturability

by

Yuqing Zhou

A dissertation submitted in partial fulfillment
of the requirements for the degree of
Doctor of Philosophy
(Mechanical Engineering)
in the University of Michigan
2018

Doctoral Committee:

Professor Kazuhiro Saitou, Chair
Professor Greg Hulbert
Professor Sridhar Kota
Professor Joaquim R.R.A. Martins

©Yuqing Zhou

yuqingz@umich.edu

ORCID: [0000-0002-1812-068X](https://orcid.org/0000-0002-1812-068X)

2018

Acknowledgments

I would like to first thank Prof. Kazuhiro Saitou for his discovery of my potentials at the beginning of this journey and the continuous support since then. He once told me that the journey of PhD is like exploring the zoo. Even though the advisor may know where to find dogs and cats, he would rather not tell me. Instead, I should always look for new paths and be ready to come back with nothing. I am not sure whether I've found the big tiger in the zoo after all these years, but I am confident to say that I am well prepared to fearlessly step into any new territories in front of me. I would also like to express my thankfulness to all my other committee members, Prof. Greg Hulbert, Prof. Sridhar Kota, and Prof. Joaquim R.R.A. Martins for their valuable input to this dissertation. The quality of this dissertation has been much improved thanks to the collaboration (2017–18) with Doc. Tsuyoshi Nomura from Toyota Research Institute of North America. During my PhD study, I've also assisted an undergraduate class: Design and Manufacturing I, as a Graduate Student Instructor. I would like to thank my previous students for sharing all those exciting moments. The co-instructor Mr. Michael Umbriac has really showed me what a true educator should look like. My research has received financial support from U.S. Department of Energy, Toyota Research Institute of North America, and Rackham Graduate School. These sources of supports are gratefully acknowledged. Finally, I would like to thank my friends, my parents, and my wife for their endless encouragement and support.

TABLE OF CONTENTS

Acknowledgments	ii
List of Figures	v
List of Tables	x
List of Abbreviations	xi
Abstract	xii
Chapter	
1 Introduction	1
1.1 Motivation	1
1.2 Background	2
1.2.1 Topology optimization	2
1.2.2 Topology optimization for manufacturability	5
1.2.3 Multi-component topology optimization	7
1.3 Dissertation goal	8
1.4 Dissertation outline	8
2 A general gradient-based continuous formulation for multi-component topology optimization	9
2.1 Prior art: non-gradient discrete formulation	9
2.2 Continuously relaxed design field	11
2.3 Continuously relaxed formulation	12
2.4 Chapter summary	13
3 Multi-component topology optimization for stamping	14
3.1 Why multiple components for stamped sheet metal structures	14
3.2 Domain discretization and design variable configuration	15
3.3 Continuously-relaxed mesh-dependent joint model	16
3.4 Structural compliance objective considering the joint property	18
3.5 Manufacturing constraint modeling for stamping	19
3.5.1 Die-set material cost	19
3.5.2 Die machining cost	22
3.6 Optimization formulation	22
3.7 Numerical results	23

3.7.1	Iterative details: cantilever	25
3.7.2	Die machining cost: Messerschmidt-Bölkow-Blohm beam	27
3.8	Chapter summary	28
4	Multi-component topology optimization for composite manufacturing	31
4.1	Why multiple components for composite structures	31
4.2	Prior art: anisotropic topology optimization	33
4.3	Design field configuration and regularization	34
4.3.1	Density field	36
4.3.2	Material orientation vector field	36
4.3.3	Component membership vector field	37
4.4	Cube-to-simplex projection method	38
4.5	Elasticity tensor composition	39
4.6	Optimization formulation	41
4.7	Numerical results	42
4.7.1	Single load: cantilever	43
4.7.2	Multi-load: tandem bicycle frame	52
4.8	Chapter summary	54
5	Multi-component topology optimization for additive manufacturing	57
5.1	Why multiple components for powder bed additively manufactured structures	57
5.2	Design field configuration	58
5.3	Manufacturing constraint modeling for powder bed additive manufacturing	59
5.3.1	Maximum allowable build volume	60
5.3.2	Elimination of enclosed holes	62
5.4	Optimization formulation	63
5.5	Numerical results	66
5.5.1	Iterative details: Messerschmidt-Bölkow-Blohm beam	67
5.5.2	Different build volume limits: cantilever	70
5.5.3	3D example: simply-supported center loading	74
5.6	Chapter summary	75
6	Summary	77
6.1	Dissertation conclusion	77
6.2	Contributions	78
6.3	Future research	79
	Bibliography	82

LIST OF FIGURES

1.1	Example current state-of-the-art structures designed by topology optimization. (a) Concept aircraft wing (Technical University of Denmark); (b) automotive body structure (Altair Engineering); (c) motorcycle frame structure (Airbus APWorks); (d) structural steel component (Arup); (e) lightweight car seat prototype (Toyota Central R&D Labs); (f) Generico chair (Marco Hemmerling and Ulrich Nether). (Online images)	3
1.2	A conventional chair assembly designed for economical production. (Online images)	4
1.3	Conventional, single-piece continuum topology optimization problem description.	5
2.1	The non-gradient discrete framework for multi-component topology optimization. Different colors indicate different components. The thin black elements indicate joint locations. (a) Design domain; (b) discretized design domain; (c) ground topology graph; (d) topology graph of a certain design; (e) realized multi-component design; (f) repaired multi-component design.	10
2.2	Demonstration of the two-layer design field, and the resulting simulation model for an example case of number of components $K = 3$. (a) Simulation model; (b) density field ρ ; (c) membership field $m^{(k)}$	12
3.1	Definition of the design variables, structural element, and two joint element types.	16
3.2	Sample extreme scenarios for Type A joints. Black, gray and white colors represent the structural materials, joint materials, and voids, respectively. Other colors represent different components with structural materials. (a) Between two, fully dense structural elements that belong to the same component; (b) between two, fully dense structural elements that belong to different components; (c) between two voids; and (d) between a fully dense structural element and a void.	17

3.3	Sample extreme scenarios for type B joints. Black, gray, and white colors represent the structural materials, joint materials, and voids, respectively. Other colors represent different components with structural materials. (a) Between four, fully dense structural elements that belong to the same component; (b) between four voids; (c-d) between four, fully dense structural elements that belong to two different components; (e-f) between two, fully dense structural elements that belong to the same component and two voids; (g) between three, fully dense structural elements that belong to the same component and one void; (h) between four, fully dense structural elements that belong to three different components; and (i) between four, fully dense structural elements that belong to four different components.	18
3.4	Computation of the bounding box with the continuously relaxed design variables. This is a mesh-dependent formulation. (The mesh-independent formulation is presented in Figure 5.1.)	21
3.5	Design domain and boundary condition settings for the (a) cantilever example; (b) Messerschmidt-Bölkow-Blohm beam example.	24
3.6	Optimization iterative details for the cantilever example at (a) iteration 1; (b) iteration 5; (c) iteration 10; (d) iteration 15; (e) iteration 30; and (f) iteration 74.	26
3.7	A comparison between the multi-component topology and conventional, single-piece topology for the cantilever example. (a) The optimized multi-component cantilever topology design. The gray regions indicate joint locations (assuming spot-welding joints) with the smaller Young’s modulus than base structural materials; (b) the conventional, single-piece cantilever topology design.	27
3.8	Convergence history of the cantilever example. Due to the relatively coarse mesh in this example, the complexity (die machining cost) constraint was not included.	28
3.9	Multi-component topology designs of the Messerschmidt-Bölkow-Blohm beam example with different levels of complexity control. (a) High die machining cost (complexity index: 3.99); (b) moderate die machining cost (complexity index: 3.45); (c) low die machining cost (complexity index: 3.03). From left to right: multi-component topology, “true” bounding box, and “true” perimeter.	29
4.1	A qualitative comparison of different composite manufacturing processes in terms of the production cost in large quantities (vertical axis) and freedom in orientation control (horizontal axis). As a manufacturing process becomes more economical for mass production, it sacrifices freedom in controlling fiber orientations. The suitability of different topology design methods is also plotted. (SFIM: short fiber injection molding; ATL: automated tape layout; TFP: tailored fiber placement; CFP: continuous fiber printing)	32

4.2	Demonstration of the three-layer design field and the resulting simulation model for an example case of number of components $K = 3$. (a) Simulation model; (b) density field ρ ; (c) membership field $m^{(k)}$; (d) orientation field $\vartheta^{(k)}$. (The material orientation for each component can be either unidirectional or curvilinear based on the regularization filter radius used. This figure only shows the unidirectional case.)	35
4.3	Coordinate transformation for the Cartesian orientation representation through an isoparametric projection method.	37
4.4	Coordinate transformation for the component membership design field through a K -dimensional cube-to-simplex projection for an example case of $K = 3$	38
4.5	The cube-to-simplex projection examples for cases of (a) $K = 2$ and (b) $K = 3$	39
4.6	Design domain and boundary conditions for the single load cantilever problem.	44
4.7	Iterative details of all design fields for the single load cantilever problem with $K = 3$ at (a) iteration 1; (b) iteration 5; (c) iteration 50; and (d) iteration 200.	45
4.8	Iterative details for the convergence of the component membership field at (a) iteration 1; (b) iteration 5; (c) iteration 50; and (d) iteration 200.	47
4.9	The optimized three-component topology with component-wise unidirectional orientations. Its optimized structural compliance is 6.21.	48
4.10	Convergence history for the single load cantilever problem with $K = 3$. (a) Compliance (objective function); (b) volume constraint; (c) membership unity measure; (d) material anisotropy constraints. (The membership unity measure is plotted for the monitoring purpose, which is not included as a constraint in the optimization.)	49
4.11	(a) Optimized single-piece topology with an isotropic material. Its optimized structural compliance is 9.92; (b) optimized single-piece topology with continuous material orientation. Its optimized structural compliance is 4.07.	50
4.12	The optimized three-component design allowing component-wise curvilinear orientations. Its optimized structural compliance is 5.65. (a) The optimized multi-component topology; (b) the optimized density field ρ ; (c) from left to right: the optimized membership field $m^{(k)}$, the optimized component field (product of the two) $\rho m^{(k)}$, and the optimized material orientation field $\vartheta^{(k)}$	51
4.13	The optimized multi-component topologies with different number of components K settings. (a) $K = 1$; (b) $K = 2$; (c) $K = 3$; (d) $K = 4$	52

4.14	Design domain and boundary conditions for the multi-load tandem bicycle frame example, where $t_x^{(p)} = -1.5$; $t_y^{(p)} = -1.0$; $t_x^{(h)} = 1.0$; $t_y^{(h)} = -1.0$; $w_x = \{-1.0, -0.25\}$; and $w_y = \{-6.0, -1.5\}$. At location (0.0, 2.0), both degrees of freedom in x and y are fixed. At location (63.5, 16.0), only the degree of freedom in y is fixed. The lower left corner of the design domain is set as location (0.0, 0.0).	53
4.15	(a) The optimized single-piece tandem bicycle frame structure with an isotropic material; (b) the deformed structure under the heavy front loading condition; (c) the deformed structure under the heavy rear loading condition. Its optimized multi-load structural compliance is 4952.	54
4.16	The optimized multi-component tandem bicycle frame structure with component-wise unidirectional material orientations. Its optimized multi-load structural compliance is 3312. (a) The optimized multi-component topology; (b) the optimized density field ρ ; (c) from left to right: the optimized membership field $m^{(k)}$, the optimized component field (product of the two) $\rho m^{(k)}$, and the orientation field $\vartheta^{(k)}$	55
5.1	Computation of the bounding box. This is a mesh-independent formulation. (The mesh-dependent formulation was presented in Figure 3.4.)	61
5.2	Problem description of multi-component topology optimization for powder bed additive manufacturing.	64
5.3	Design domain and boundary condition settings for the (a) Messerschmidt-Bölkow-Blohm beam example; (b) cantilever example.	67
5.4	Design field iterative details for the Messerschmidt-Bölkow-Blohm beam example at (a) iteration 1; (b) iteration 35; (c) iteration 80; and (d) iteration 311.	69
5.5	Component interface explanation. The gray zone between component boundaries is less stiff than regular base materials in the simulation model. Different colors indicate different components.	70
5.6	Manufacturing constraint iterative details for the Messerschmidt-Bölkow-Blohm beam example at (a) Iteration 1; (b) iteration 35; (c) iteration 80; and (d) iteration 311.	71
5.7	The optimized multi-component topology for the MBB beam example. The prescribed, maximum allowable build volume is plotted for each component. Different colors indicate different components.	72
5.8	The optimized topologies for the cantilever example with different prescribed maximum allowable build volume: (a) 2.0×1.0 ; (b) 1.5×0.6 ; (c) 1.0×0.4 ; (d) 2.5×0.3 ; (e) the prescribed maximum allowable build volume for (a-d).	73
5.9	Design domain and boundary condition settings for the 3D simply-supported center loading example.	74
5.10	The conventional, single-piece optimized topology for the 3D simply-supported center loading example without applying manufacturing constraints. (a) The quarter domain optimized structure; (b) the mirrored half domain structure.	75

5.11 The full domain optimized multi-component topology for the 3D simply-supported center loading example with manufacturing constraints. (a) The full domain optimized multi-component structure; (b) the sliced half domain multi-component structure. 76

LIST OF TABLES

4.1	Material properties for the numerical examples.	42
4.2	Summary of the structural performance and estimated mass-production cost of cantilever designs discussed in Section 4.7.1.	52
5.1	Material properties and parameters for numerical examples.	66

LIST OF ABBREVIATIONS

ABB	Axis-aligned Bounding Box
ATL	Automated Tape Layout
BIW	Body In White
BFGS	Broyden–Fletcher–Goldfarb–Shanno
CFP	Continuous Fiber Printing
DMO	Discrete Material Optimization
ESO	Evolutionary Structural Optimization
M3TO	Multi-component Multi-material Multi-process Topology Optimization
MABB	Minimum Area Bounding Box
MBB	Messerschmidt-Bölkow-Blohm
MTO	Multi-component Topology Optimization
MTO-A	Multi-component Topology Optimization for Additive manufacturing
MTO-C	Multi-component Topology Optimization for Composite manufacturing
MTO-S	Multi-component Topology Optimization for Stamping
OBB	Oriented Bounding Box
SIMP	Solid Isotropic Material with Penalization
SFIM	Short Fiber Injection Molding
TFP	Tailored Fiber Placement
VAC	Variable Axial Composite

ABSTRACT

Topology optimization is a method where the distribution of materials within a design domain is optimized for a structural performance. Since the geometry is represented non-parametrically, it facilitates innovative designs through the exploration of arbitrary shapes. Due to its unconstrained exploration, however, topology optimization often generates impractical designs with features that prevent economical manufacturing, e.g., complex perimeters and many holes. Above all, existing topology optimization methods assume that the optimized structure will be made as a single piece.

However, structures are usually not monolithic (i.e., single-piece), but assemblies of multiple components, e.g., cars, airplanes, or even chairs. It is mainly because producing multiple components with simple geometries is often less expensive (i.e., better manufacturability) than producing a large single-piece part with complex geometries, even with the additional cost of assembly.

This dissertation discussed a topology optimization method for designing structures assembled from components, each built by a certain manufacturing process, termed the Multi-component Topology Optimization (MTO). The prior art of MTO used discrete formulations solved by genetic algorithms. To overcome the high computational cost associated with non-gradient heuristic optimization, this dissertation proposed a continuously relaxed gradient-based formulation for MTO. The proposed formulation was demonstrated with three manufacturing processes.

For the sheet metal stamping process, by modeling stamping die cost manufacturing constraints and assuming resistant spot welding joints, the simultaneous optimization of base topology and component decomposition was, for the first time, attained using an efficient gradient-based optimization algorithm based on design sensitivities.

For the composite manufacturing process, a cube-to-simplex projection and penalization method was proposed to handle the membership unity requirement. With the multi-component concept, a unique structural design solution for economical composite manufacturing was achieved. The component-wise anisotropic material orientation design for topology optimization was presented without prescribing a set of alternative discrete angles as required by most existing material orientation methods.

For the additive manufacturing process, the MTO method enabled the design of additively manufactured structures larger than the printer's build volume. By modeling manufacturing constraints on the build volume limit and elimination of enclosed holes, the optimized structure was an assembly of multiple components, each produced by a powder bed additive manufacturing machine. The first reported 3D example of MTO was presented.

CHAPTER 1

Introduction

1.1 Motivation

Structures are usually not monolithic (i.e., single-piece), but assemblies of multiple components. For example, a car usually has about 30000 parts [1]. The Boeing 737 airplane is made up of 367000 parts [2]. Most dinosaur skeletons have several hundred individual bones [3]. Even a frying pan is made of a disc base and a handle.

This dissertation was originally motivated by a fundamental question: why so many parts for structural products? Apparently, if different materials are necessary, a product has to be decomposed into pieces. This is the case for the frying pan, which requires thermal insulation materials to prevent the handle from getting too hot and heat conduction materials to heat up food. In addition, if relative motions are required, a structure also has to be decomposed into pieces. This is the case for dinosaur skeletons, where bones, connected by muscles and joints, move relative to each other.

However, the above two arguments are not applicable to the automotive Body In White (BIW), which is usually an assembly of many sheet metal stamped components joined by resistance spot welding. An automotive BIW can be made from a single material (e.g., steel), and does not involve any relative motions. It is mainly because producing multiple components with simple geometries are less expensive than producing a single piece BIW with complex geometries, even with the additional cost of assembly. In other words, the manufacturability of multi-component structures is often much better than that of single-piece structures. The manufacturability argument for a multi-component structural product is the main motivation and focus of this dissertation while the other two, i.e., the materials and relative motions, are not.

1.2 Background

Topology optimization is a method for designing structures by optimally distributing materials within a prescribed design domain. It is an interdisciplinary research area between computational mechanics and design optimization. Unlike sizing and shape optimization, which are often based on parametric geometry representations, topology optimization describes geometries non-parametrically. It facilitates innovative designs through the exploration of arbitrary shapes.

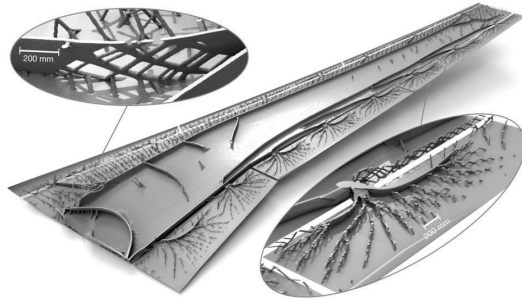
Figure 1.1 presents several state-of-the-art example structures designed by topology optimization. It is obvious to see that structures generated by topology optimization are vastly different from conventional designs. Such out-of-box designs demonstrated the benefit of topology optimization in design exploration. However, these examples also revealed another significant shortcoming of designs generated by topology optimization: lack of manufacturability. Structures shown in Figure 1.1(a–b) are 3D digital models, which are still far away from realization into airplanes and cars. Structures shown in Figure 1.1(c–f) are prototypes produced by additive manufacturing, which are clearly not ready for economical production in large quantities.

As seen in Figure 1.1, current state-of-the-art topology optimization designs share two major similarities, i.e., the complex overall geometry and the single-piece design, both of which lead to their lack of manufacturability. In contrast, structures designed for improved manufacturability or economical production in large quantities are usually assemblies of multiple components with simple component geometries. For example, Figure 1.2 shows a conventional chair assembly designed for economical production, which is composed of multiple beam and plate components assembled with fasteners.

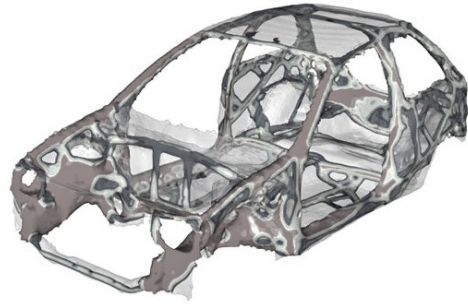
The rest of this section reviews topology optimization methods (Section 1.2.1) and two related topics about improving manufacturability for topology optimization. Section 1.2.2 discusses related works in single-piece topology optimization for manufacturability. Section 1.2.3 discusses previous works in topology optimization of multi-component structures.

1.2.1 Topology optimization

According to [4], topology optimization is a natural outcome of introducing the material micro-structure design to shape and sizing optimization. Cheng & Olhoff (1981) discussed the optimal thickness distribution for elastic plates [5]. Their work led to a series of works on optimal design problems introducing micro-structure. Kikuchi



(a)



(b)



(c)



(d)



(e)



(f)

Figure 1.1: Example current state-of-the-art structures designed by topology optimization. (a) Concept aircraft wing (Technical University of Denmark); (b) automotive body structure (Altair Engineering); (c) motorcycle frame structure (Airbus APWorks); (d) structural steel component (Arup); (e) lightweight car seat prototype (Toyota Central R&D Labs); (f) Generico chair (Marco Hemmerling and Ulrich Nether). (Online images)



Figure 1.2: A conventional chair assembly designed for economical production. (Online images)

and Bendsøe (1988) first introduced the material distribution approach for topology optimization [6].

Since the late 1980s, different methods have been developed for topology optimization, e.g., the Solid Isotropic Material with Penalization (SIMP) method [7, 8], the Evolutionary Structural Optimization (ESO) method [9], the topological derivative-based and level-set method [10, 11, 12, 13], the non-gradient method [14, 15], and the moving morphable components method [16]. For general introduction of different topology optimization methods, readers are referred to several review papers [17, 18, 19, 20].

Based on different types of design domains, topology optimization can be classified into discrete (truss/beam) approaches and continuum (pixel/voxel) approaches. The continuum approach is the focus of this dissertation. Since the optimal structures of the discrete approaches are the collections of predefined primitive members, such as trusses and beams, the continuum approaches have advantages in representing realistic products with complex geometries.

Based on different types of optimization algorithms utilized, topology optimization can be classified into gradient-based methods and non-gradient methods. The gradient-based method is the focus of this dissertation. Recently, in topology optimization community, non-gradient methods received some serious critiques regarding their applicability in continuum topology optimization problems [18, 21]. It is due, mainly, to their lack of design sensitivities (i.e., gradient information), and the associated high computational cost.

Figure 1.3 presents the conventional, single-piece continuum topology optimiza-

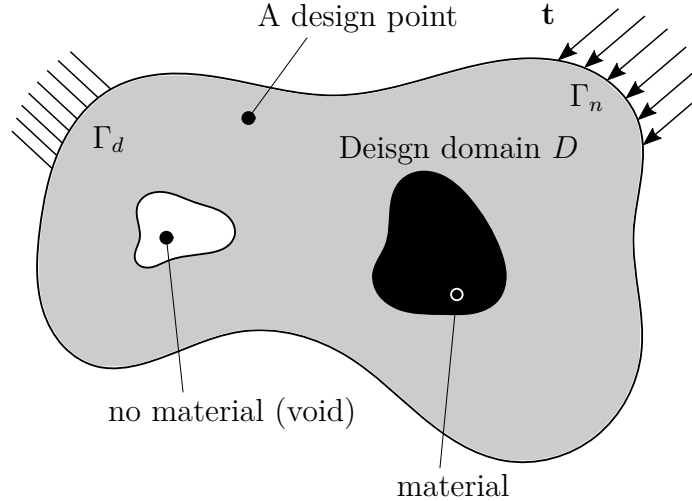


Figure 1.3: Conventional, single-piece continuum topology optimization problem description.

tion problem description. In a prescribed design domain D , under given boundary conditions (e.g., displacement boundary condition on Γ_d and traction boundary condition on Γ_n), the problem is to optimize a structural performance by designing the existence of materials in each design point, subject to some constraints (e.g., volume fraction). It can be summarized as a generalized shape design problem of finding the optimal material distribution.

Other than mechanical design problems, topology optimization has also been applied to a variety of other applications, e.g., heat transfer [22], turbulent flow [23], antennas [24], architecture [25], and micro-systems [26].

1.2.2 Topology optimization for manufacturability

This section discusses manufacturing constraints for conventional, single-piece topology optimization. Two major classes are discussed including the general-purpose manufacturing constraints and process-specific manufacturing constraints.

It is well-known that continuum topology optimization tends to generate numerous small holes, i.e., checkerboards [27, 28]. This behavior leads to mesh-dependency and non-existence of solutions. To resolve this issue, regularization schemes have been developed. They can be summarized into two main categories, the filtering methods [29, 30, 31, 32] and the constraint methods [33, 34, 28, 35, 36]. Recently, the PDE-based filtering method [37, 38] gained popularity due to its ease of implementation and superior computational efficiency. When a regularization scheme is applied to topology optimization, it not only avoids numerical instabilities, but gen-

erates results with much simpler geometries. The reduced shape complexity usually leads to better general manufacturability. Therefore, such regularization schemes are regarded as general-purpose manufacturing constraints.

Manufacturing constraints modeled for certain manufacturing processes are referred to as process-specific manufacturing constraints. Such constraints are usually imposed on part geometries. They are often more specific than general-purpose manufacturing constraints. For example, if a part is designed for molding and casting, it has to be open and lined up with the draw direction of the die. If this restriction is not applied to topology optimization, the resulting geometry is likely to have cavities and overhang features that would prohibit drawing the die. To ensure the manufacturability of structural topology designs for molding and casting, Zhou et al. (2002) [39] proposed to model the moldability constraint as additional single variable linear inequality constraints. Similar moldability manufacturing constraints were integrated into level-set topology optimization [40, 41]. Recently, methods based on fictitious physical models were developed to ensure the moldability of topology optimized structures [42, 43]. Extrusion constraints have also been proposed to enforce uniform cross-sections [39, 44]. To better conform to manufacturing processes tailored to plate structures, a geometry projection method was proposed to generate assemblies of discrete geometric components [45, 46]. For composite resin transfer molding, a data-driven model for resin filling time prediction was developed and integrated into topology optimization [47]. To reduce the amount of support materials required for additive manufacturing, different overhang manufacturing constraint methods were developed (e.g., [48, 49, 50, 51, 52, 53, 54]). For parts designed for additive manufacturing, enclosed voids should be avoided, so that the un-melted metal powders or internal support materials can be removed from the component once it has been built. A virtual temperature method was proposed to eliminate enclosed voids by constraining the maximum temperature field of a fictitious thermal analysis [55, 56]. To generate bone-like porous structures as lightweight infill for additive manufacturing, the method based on an upper bound constraint on localized material volume fraction was proposed [57, 58].

For more manufacturing oriented topology optimization methods, readers are referred to recent review papers [59, 60].

In summary, while the integration of manufacturing constraints in topology optimization can lead to better manufacturability of the optimized structure, its performance is often degraded. In some cases, the sacrifice of structural performance can be drastic. It is partially because the manufacturing constraints are always applied

to the entire single-piece structure. The single-piece assumption may overly simplify the geometries, which goes completely against the benefit of topology optimization. However, in the scope of this dissertation, when manufacturing constraints are applied to each individual component of a multi-component structure instead of the entire single-piece structure, they will gain new interpretations.

1.2.3 Multi-component topology optimization

MTO is an evolution of conventional, monolithic (i.e., single-piece) topology optimization, which not only optimizes the overall base topology, but the component decomposition. From a viewpoint of mathematical formulation, it is closely related to multi-material topology optimization (e.g., [61, 62, 63, 64, 65, 66]), where different materials in multi-material structures can be regarded as different components in multi-component structures. Unlike most topology optimization studies (including multi-material topology optimization) that focus merely on optimizing various structural performances, MTO is motivated by the need of generating ready-to-manufacture optimal structures made as assemblies of multiple components, each of which conforms geometric constraints imposed by a chosen manufacturing process.

Another related topic to MTO is the topology optimization for embedded components, also known as the component layout optimization (e.g., [67, 68, 69, 70, 71, 72, 73]). Though these works are important for certain applications, e.g., the integration of rigid objects, actuators and integrated circuits, the components are assumed with fixed geometries and only allowed floating during the course of optimization.

There are three major classes in prior art of MTO. The first class assumes a priori knowledge of joint locations [74, 75, 76, 77]. The second class assumes that component decomposition is an independent problem from base topology optimization [78, 79, 80, 81, 82]. By relaxing the above two assumptions, the third class poses the simultaneous optimization of base topology and component decomposition, which is the focus of this dissertation. It was originally formulated as discrete optimization problems and solved by genetic algorithms [83, 84, 85]. However, as discussed in Section 1.2.1, such non-gradient heuristic methods for topology optimization have received criticisms regarding their computational inefficiency for high resolution problems [18, 21]. To address the criticisms, this dissertation proposes to model the component decomposition as a relaxed continuous problem, and developed a gradient-based framework for MTO.

Instead of designing a part via conventional, single-piece topology optimization,

MTO can be directly applied to designing structures assembled from components, each built by a certain manufacturing process.

1.3 Dissertation goal

The primary goal of this dissertation is to develop a new mathematical formulation for MTO that can provide scalable multi-component structural design solutions, which also take manufacturing limitations into account. Prior MTO methods were limited to discrete formulations solved by genetic algorithms, which were not suitable for large-scale problems.

The secondary goal is to expand MTO applications to varieties of manufacturing processes. Prior MTO methods were limited to the sheet metal stamping process.

1.4 Dissertation outline

The remainder of this dissertation is organized as follows. Chapter 2 presents a general gradient-based continuous framework for MTO. Chapter 3, 4, and 5 discuss three MTO applications, including stamping, composite manufacturing, and additive manufacturing. Finally, Chapter 6 summarizes the dissertation and discusses opportunities for future research.

CHAPTER 2

A general gradient-based continuous formulation for multi-component topology optimization

This chapter introduces a new gradient-based continuous framework for MTO. It is a relaxation of the discrete formulation in [84] and [85], which is briefly reviewed first in Section 2.1 for the sake of comparison.

2.1 Prior art: non-gradient discrete formulation

As seen in Figure 2.1(b), a prescribed design domain D is discretized into finite elements such that every other adjacent structural element (square) sandwiches a joint element (thin rectangle). Discrete design variables are assigned to both structural (\mathbf{x}) and joint (\mathbf{y}) elements, where:

$$x_i = \begin{cases} 1 & \text{if structural material exists in element } i \\ 0 & \text{otherwise} \end{cases},$$

and

$$y_j = \begin{cases} 2 & \text{if joint material exists in element } j \\ 1 & \text{if structural material exists in element } j \\ 0 & \text{otherwise} \end{cases}.$$

In the case of $y_j = 2$, it indicates the existing of a joint in element j , and the neighbor two structural elements belonging to different components.

Figure 2.1(c) shows a ground topology graph such that a node represents a structural element, and an edge represents a joint element. A given combination of \mathbf{x} and \mathbf{y} can be interpreted as a unique topology graph, e.g., Figure 2.1(d). After certain repairing of invalid structures, a topology graph is realized as a multi-component

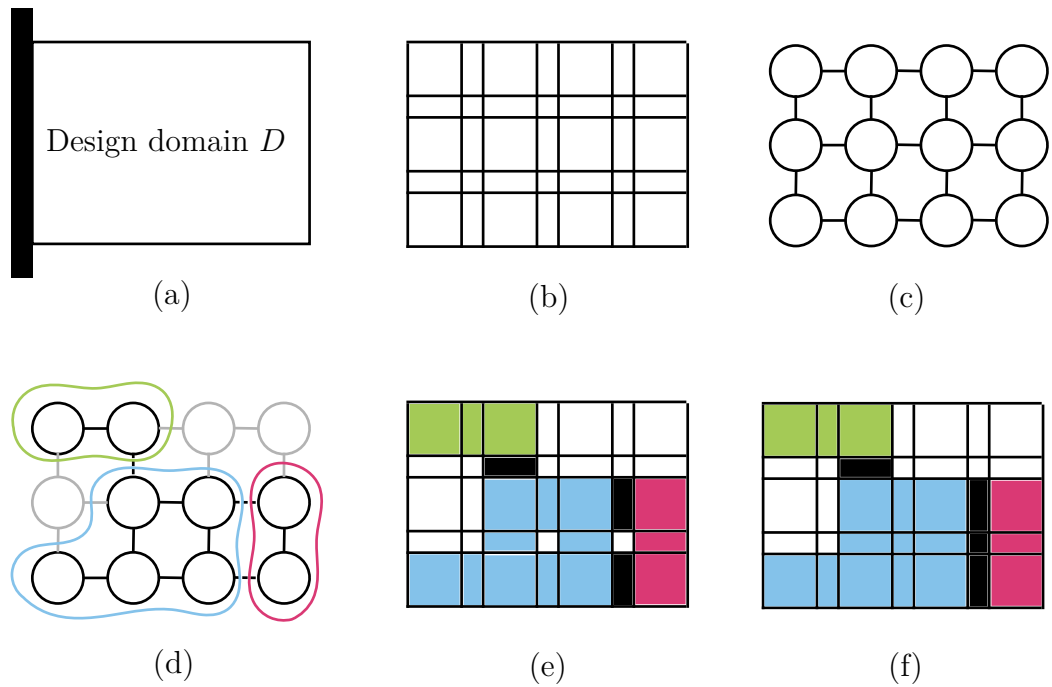


Figure 2.1: The non-gradient discrete framework for multi-component topology optimization. Different colors indicate different components. The thin black elements indicate joint locations. (a) Design domain; (b) discretized design domain; (c) ground topology graph; (d) topology graph of a certain design; (e) realized multi-component design; (f) repaired multi-component design.

topology design, e.g., Figure 2.1(f).

Using discrete variables \mathbf{x} and \mathbf{y} , a multi-objective MTO problem can be formulated with both structural performance and manufacturing costs modeled as objectives. Additional constraints can be added if needed, e.g., weight target. Because the overall optimization problem is modeled with discrete variables and manufacturing cost functions are often not directly differentiable, in [84], a multi-objective genetic algorithm was used to solve it.

As discussed in Chapter 1, such non-gradient discrete formulation will encounter computational efficiency limitations. With the Kriging-interpolated level-set extension [85], the number of design variables can be significantly reduced. However, due to the nature of non-gradient methods and lack of sensitivity information during optimization, the computational efficiency improvement is still marginal.

To overcome these challenges, this dissertation presents a continuously relaxed formulation for MTO in a gradient-based framework. For the first time, the simultaneous optimization of base topology and component decomposition is attained using an efficient gradient-based optimization algorithm based on design sensitivities.

2.2 Continuously relaxed design field

As demonstrated in Figure 2.2, in the continuous MTO formulation, there are two layers of design fields. The first layer is the material density field ρ as a common field for all components, which describes the overall base topology. The second layer is the membership vector field $\mathbf{m} = (m^{(1)}, m^{(2)}, \dots, m^{(K)})$. $m^{(k)}$ represents the fractional membership of a design point in the design domain to the k -th component, $k = 1, 2, \dots, K$, where K is the prescribed, maximum allowable number of components. The specification of K is not needed in the discrete formulation as discussed in Section 2.1. Both ρ and $m^{(k)}$ are continuous variables ranging between 0 and 1. In order to ensure the unique selection of the component for each design point, an additional important criterion needs to be satisfied at the end of optimization. The membership to only one component converges to 1 while the memberships to all other components converge to 0. In this dissertation, different methods have been proposed to meet this requirement. Chapter 3 proposes to use many equality constraints to ensure the unity of fractional component memberships. For each design point i , a linear constraint $\sum_{k=1}^K m_i^{(k)} = 1$ is added. In Chapter 4 and 5, different nonlinear projection methods are used to replace the large number of equality constraints.

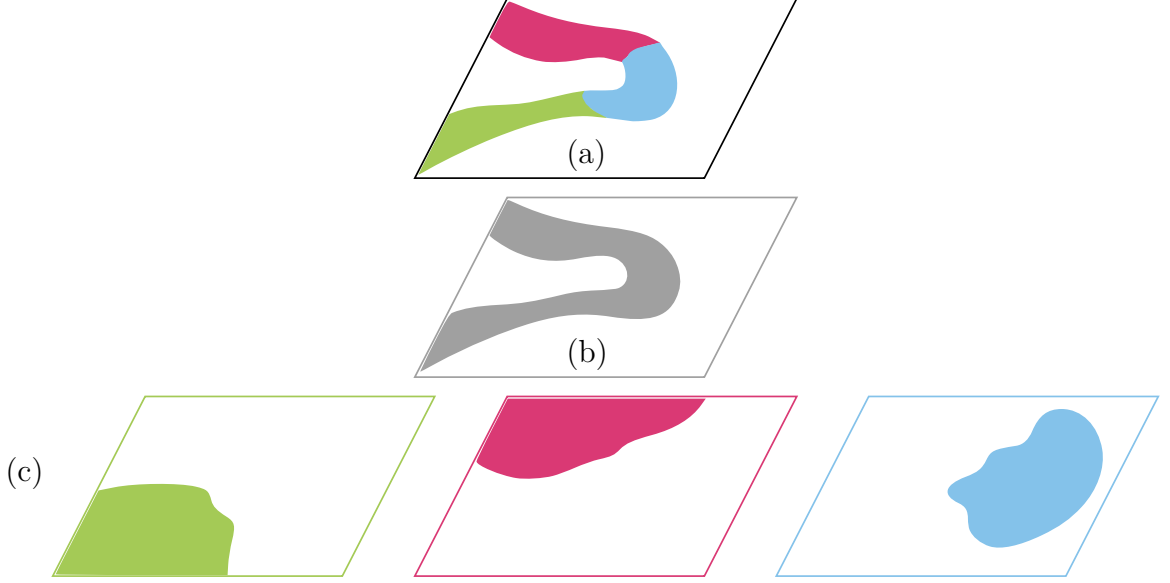


Figure 2.2: Demonstration of the two-layer design field, and the resulting simulation model for an example case of number of components $K = 3$. (a) Simulation model; (b) density field ρ ; (c) membership field $m^{(k)}$.

2.3 Continuously relaxed formulation

With the continuously relaxed design field, a general gradient-based continuous MTO formulation can be summarized as follows:

$$\begin{aligned}
 & \underset{\rho, m^{(1)}, \dots, m^{(K)}}{\text{minimize}} && F \\
 & \text{subject to} && \mathbf{h} \leq \mathbf{0} \\
 & && \rho \in [0, 1]^D, \\
 & && \text{for } k = 1, 2, \dots, K : \\
 & && \mathbf{g}^{(k)} \leq \mathbf{0} \\
 & && m^{(k)} \in [0, 1]^D
 \end{aligned} \tag{2.1}$$

where ρ and $m^{(k)}$ are the density and membership design fields; F is the structural performance objective (e.g., stiffness and strength); $\mathbf{g}^{(k)}$ is a vector of manufacturing constraints applied to each decomposed component k based on different manufacturing process applications; \mathbf{h} is a vector of other constraints based on other design requirements (e.g., volume fraction). Both the objective (F) and constraints (\mathbf{h} and $\mathbf{g}^{(k)}$) should be modeled as continuous and differentiable functions with respect to all design fields for the use of efficient gradient-based optimization.

The manufacturing constraint modeling for gradient-based topology optimization has been a challenging task due to the nature of “blurry” intermediate topologies. Relaxation and approximation are often needed. For example, [28] used the total variation of the density field to approximate the complexity of an intermediate topology when its perimeter cannot be directly quantified. The MTO adds an additional layer of difficulties to the manufacturing constraint modeling, because the “blurry” effect is also applicable to the intermediate component decomposition. The component boundaries will not be clear until the end of optimization while the geometric constraint evaluation has to be done at the component level throughout the optimization.

2.4 Chapter summary

This chapter presented a general gradient-based continuous MTO formulation that will be used for different manufacturing processes in the rest of this dissertation. The overall base topology was described with a density design field following the conventional, density-based topology optimization methods (e.g., SIMP). To model the component decomposition in a relaxed continuous manner, the concept of fractional membership of a design point to different components was introduced. After the relaxation of design fields, the gradient-based continuous MTO formulation was presented, which built a foundation for the rest of this dissertation.

CHAPTER 3

Multi-component topology optimization for stamping

This Chapter presents the MTO application to stamped sheet metal structures, termed the Multi-component Topology Optimization for Stamping (MTO-S). Stamping is the process of placing flat sheet metal into a stamping die where a tool and the die surface will form the flat sheet metal into a net shape. Stamping has been widely used across different industries due to its primary advantage of high production rate with minimum operator intervention. As discussed in Chapter 1, most structural products are assemblies of multiple components. This is especially true for stamped sheet metal products. Different welding processes have been developed to connect the components into a final product assembly. While some products with small scale and simple geometries can be made as a single piece, e.g., water sinks, most sheet metal products are designed as multi-component structures, e.g., automotive, ships.

3.1 Why multiple components for stamped sheet metal structures

The cost of stamping dies contributes to the majority of the cost for manufacturing sheet metal products, which consists of the cost of die-set materials and the cost for machining the die. As die-set raw materials are usually purchased as rectangular prisms, the cost of die-set materials can be empirically modeled as proportional to the size of the bounding box enclosing each component [86]. The cost for machining the die can be modeled as proportional to a complexity index, which is defined as the perimeter of each component normalized by its bounding box size [86].

The sheet metal assemblies are usually joined by a welding process, which will inevitably require additional assembly costs compared with a single-piece product.

However, compared with the investment in stamping dies, the assembly cost is relatively low and sometimes even negligible.

Therefore, for a complex sheet metal product, it is often more cost effective to design it as an assembly of multiple components with simple component geometries than producing a single-piece product with complex geometries, even with the additional cost of assembly.

The standard practice of designing a multi-component stamped sheet metal product is to design and optimize its overall (single-piece) base geometry first, and then decompose it to refine part boundaries and joint configurations. Such practice, known as a two-step approach, is likely to yield suboptimal solutions with respect to the overall structural performance and/or manufacturing and assembly costs, since the optimal decomposition obtained in the second step is largely dependent on the optimal overall geometry obtained in the first step. The MTO-S method proposed in this chapter intends to realize the simultaneous design of the base topology and component decomposition for stamped sheet metal multi-component structures.

3.2 Domain discretization and design variable configuration

A prescribed design domain D is discretized into finite elements in the same manner as in Figure 2.1(b). Due to this special domain discretization, the mathematical formulation presented in this Chapter is mesh-dependent. Mesh-independent formulations will be presented in Chapter 4 and 5. Design variables are only defined in structural elements as shown in Figure 3.1. Following the two-layer design variables. For a structural element i , the (fictitious) density ρ_i takes a continuous value ranging from zero to one, similar to the conventional SIMP formulation. The membership design variable \mathbf{m}_i is a vector of size K , where K is the prescribed, maximum allowable number of components. Each element $m_i^{(k)}$ of \mathbf{m}_i also takes a continuous value ranging from zero to one, representing the fractional membership of element i in component k . An additional linear constraint $\sum_{k=1}^K m_i^{(k)} = 1$ is added to each structural element i in order to ensure the unity of total fractional memberships. Similar mathematical formulations can be found in multi-material topology optimization studies (e.g., [87, 88]).

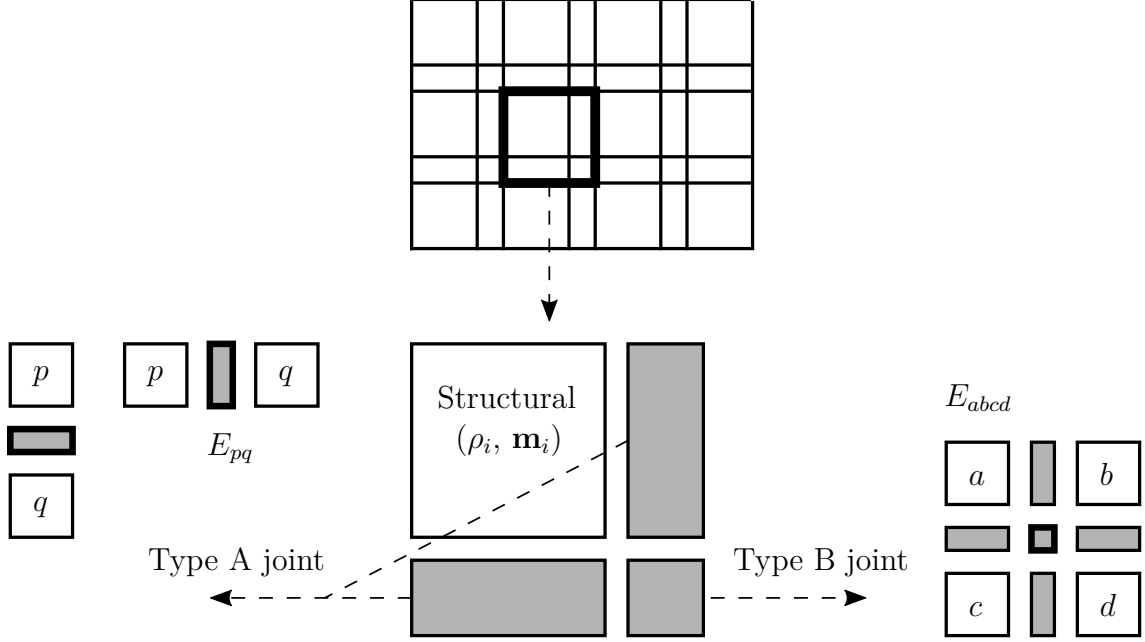


Figure 3.1: Definition of the design variables, structural element, and two joint element types.

3.3 Continuously-relaxed mesh-dependent joint model

The joint model assumes resistance spot-welding joints, which usually have less stiffness than structural members [89]. The joint model formulation, however, is general enough to be applicable to other joining processes with different material properties. There are two types of joint elements, as shown in Figure 3.1. One is the thin strip between two structural elements p and q , denoted as the Type A joint. The equivalent Young's modulus of such joint elements is determined by density ρ and membership \mathbf{m} of the two neighbor structural elements. A joint stiffness matrix \mathbf{H} is defined as a $K \times K$ symmetric matrix where all diagonal elements are Young's modulus of structural materials $E^{(S)}$, and all off-diagonal elements are Young's modulus of joint materials $E^{(J)}$ ($< E^{(S)}$ for resistance spot-welded joints). Matrix \mathbf{H} can be written as:

$$\mathbf{H} = \{h_{ij}\} = \begin{cases} E^{(S)} & \text{if } i = j \\ E^{(J)} & \text{if } i \neq j \end{cases}. \quad (3.1)$$

The equivalent Young's modulus E_{pq} of a Type A joint element between structural elements p and q is computed as:

$$E_{pq} = \rho_p \mathbf{m}_p^\top \mathbf{H} \mathbf{m}_q \rho_q, \quad (3.2)$$

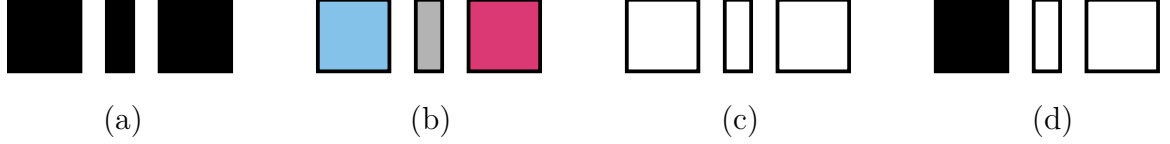


Figure 3.2: Sample extreme scenarios for Type A joints. Black, gray and white colors represent the structural materials, joint materials, and voids, respectively. Other colors represent different components with structural materials. (a) Between two, fully dense structural elements that belong to the same component; (b) between two, fully dense structural elements that belong to different components; (c) between two voids; and (d) between a fully dense structural element and a void.

where ρ_p and ρ_q are densities of structural elements p and q , and \mathbf{m}_p and \mathbf{m}_q are their corresponding memberships. Figure 3.2 shows sample extreme scenarios for Type A joints. The equivalent Young’s modulus of a Type A joint takes a value $E_{pq} = E^{(S)}$ if structural elements p and q both belong to the same component and have full density values, indicating the joint element is actually a part of a structural member (Figure 3.2(a)); $E_{pq} = E^{(J)}$ if the neighbor structural elements belong to different components and have full density values, indicating the joint element represents a welded joint (Figure 3.2(b)); and $E_{pq} = 0$ if at least one of p and q has zero density value (Figure 3.2(c–d)). Otherwise, E_{pq} takes a value between zero and $E^{(S)}$, indicating the joint element is “in a fractional state”, somewhere between void (no weld) and structural solid.

The other type of joint element is the smaller square diagonal element, denoted as Type B joint in Figure 3.1. Its equivalent Young’s modulus E_{abcd} surrounded by structural elements a , b , c , and d , is defined as the penalized average of the four neighbor Type A joint elements:

$$E_{abcd} = ((E_{ab} + E_{ac} + E_{bd} + E_{cd})/4)^{P_w}, \quad (3.3)$$

where E_{ab} , E_{ac} , E_{bd} , and E_{cd} are the equivalent Young’s moduli of Type A joint elements between structural elements a and b , a and c , b and d , and c and d , respectively. The power $P_w = \log_{(E^{(S)}+E^{(J)})/2} E^{(J)}$ ensures that E_{abcd} takes reasonable values for most conceivable circumstances.

Figure 3.3 shows sample extreme scenarios for Type B joint elements. While the penalization strategy in Equation (3.3) is tuned to cover the most common scenarios in Figure 3.3(a–d), it produces somewhat (albeit negligibly infrequent) unnatural outcomes under several other scenarios such as the ones shown in Figure 3.3(e–i). Under the scenario in Figure 3.3(e), Equation (3.3) sets $E_{abcd} = 0$, leading to a disconnected

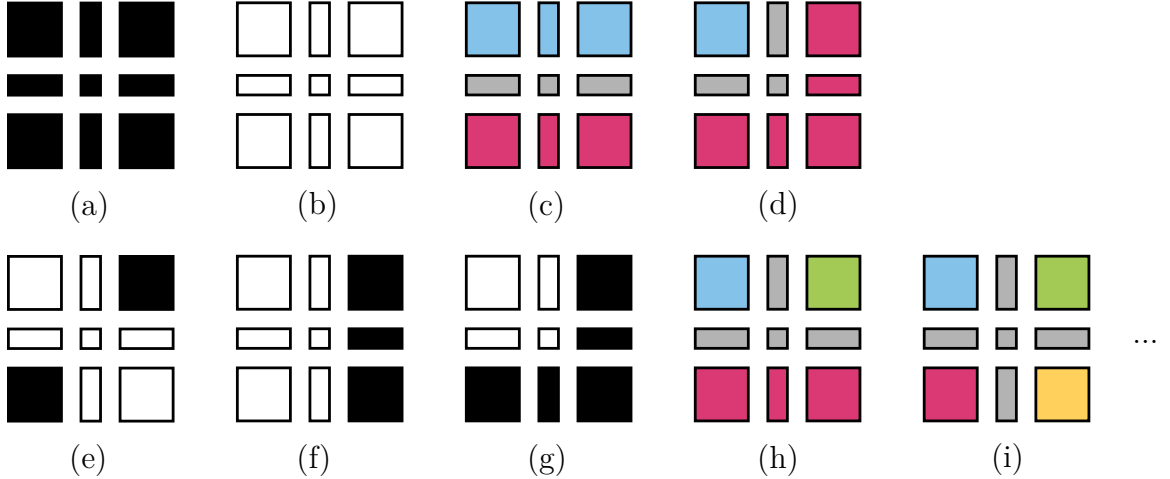


Figure 3.3: Sample extreme scenarios for type B joints. Black, gray, and white colors represent the structural materials, joint materials, and voids, respectively. Other colors represent different components with structural materials. (a) Between four, fully dense structural elements that belong to the same component; (b) between four voids; (c-d) between four, fully dense structural elements that belong to two different components; (e-f) between two, fully dense structural elements that belong to the same component and two voids; (g) between three, fully dense structural elements that belong to the same component and one void; (h) between four, fully dense structural elements that belong to three different components; and (i) between four, fully dense structural elements that belong to four different components.

component. However, this would be discouraged during the process of minimizing compliance, and also would potentially contribute to eliminating checkerboard patterns. Under the scenarios in Figure 3.3(f-g), Equation (3.3) assigns E_{abcd} with a very small value that can be virtually considered as zero. The values of E_{abcd} in conditions Figure 3.3(h-i) would be slightly smaller than $E^{(J)}$. Since such conditions rarely happen, the effect would also be negligible.

3.4 Structural compliance objective considering the joint property

As a result of the special domain discretization and the relaxed joint stiffness model discussed above, joint locations and properties can now be integrated into the overall structural compliance computation, written as:

$$F = \mathbf{f}^\top \mathbf{u} = \mathbf{u}^\top \mathbf{K}(\mathbf{E}) \mathbf{u}, \quad (3.4)$$

where \mathbf{f} is the external load and \mathbf{u} is the solved displacement. $\mathbf{K}(\mathbf{E})$ is the global stiffness matrix assembled from the element stiffness \mathbf{K}^e . $\mathbf{K}(\mathbf{E})$ is a function of \mathbf{E} containing the equivalent Young’s moduli of structural and joint elements. For structural element i , the equivalent Young’s modulus $E_i = \rho_i^{P_d} E^{(S)}$, which is the power law in the conventional SIMP formulation. P_d is the density penalty parameter. For joint elements, the equivalent Young’s moduli are calculated based on Equations (3.2) and (3.3).

3.5 Manufacturing constraint modeling for stamping

As discussed in Section 3.1, the manufacturing cost of a stamping die mainly consists of the die-set material cost and the cost for machining the die [86].

3.5.1 Die-set material cost

The cost of die-set materials is modeled as proportional to the area of the bounding box enclosing each component [86].

The computation of bounding boxes is a fundamental problem in computer graphics. Based on the tightness of the bounding box, it can be computed in several different ways. The Axis-aligned Bounding Box (ABB) can be computed efficiently by fixing the orientation of the bounding box. However, it’s not sufficiently tight for many applications. The Oriented Bounding Box (OBB) whose orientation is determined by an approximation analysis is much tighter than ABB yet still not optimal. The Minimum Area Bounding Box (MABB) is the theoretically ideal solution to describe the size of a component. Unfortunately, its high computational complexity make it virtually unusable for practical problems. OBB is used in this dissertation to quantify the component size.

Many algorithms have been developed for the bounding box computation in computer graphics (e.g., [90, 91, 92, 93]). Unfortunately, existing algorithms are not directly applicable to our problem because they all require fixed input geometries with “clear” part boundaries. To accommodate the “blurry” intermediate topologies during the course of MTO, a weighted principal component analysis is proposed to approximate the orientation of the bounding box. A weighted projection method is proposed to approximate the size of the bounding box. The weighting function contains the information of both density and membership design variables. The density design variables model the “blurry” effect on the overall base topology while the

membership design variables model the “blurry” effect regarding the intermediate component decomposition.

The orientation of the bounding box of component k is approximated using a weighted principal component analysis, where centroid \mathbf{x}_i of each structural element i in the design domain is associated with a fictitious weight $\rho_i m_i^{(k)}$ as illustrated in Figure 3.4. For each component k , the weighted covariance matrix $\Sigma^{(k)}$ can be written as follows:

$$\Sigma^{(k)} = \frac{\sum_{i=1}^N \rho_i m_i^{(k)} (\mathbf{x}_i) (\mathbf{x}_i)^\top}{\sum_{i=1}^N \rho_i m_i^{(k)}}, \quad (3.5)$$

where N is the number of structural elements. By applying the singular value decomposition on $\Sigma^{(k)}$, two orthogonal principal components $\mathbf{v}_1^{(k)}$ and $\mathbf{v}_2^{(k)}$ can be extracted, which will describe the approximate orientation of the OBB of component k .

The area of OBB of component k is approximated using the weighted projection variance, where the variances of the centroids \mathbf{x}_i , weighted with $\rho_i m_i^{(k)}$, and projected onto $\mathbf{v}_1^{(k)}$ and $\mathbf{v}_2^{(k)}$, are considered as the approximation of the length of the two sizes of the OBB. For each component k , the length (or width) of the OBB in direction $\mathbf{v}_j^{(k)}$ is approximated as a weighted projection variance:

$$l_j^{(k)} = \frac{\sum_{i=1}^N \rho_i m_i^{(k)} (z_{ij}^{(k)} - c_j^{(k)})^2}{\sum_{i=1}^N \rho_i m_i^{(k)}}, \quad (3.6)$$

where $z_{ij}^{(k)} = (\mathbf{x}_i)^\top \mathbf{v}_j^{(k)}$ is the projection of \mathbf{x}_i onto $\mathbf{v}_j^{(k)}$, and $c_j^{(k)}$ is the center of component k in the $\mathbf{v}_j^{(k)}$ direction, given as:

$$c_j^{(k)} = \frac{\sum_{i=1}^N \rho_i m_i^{(k)} z_{ij}^{(k)}}{\sum_{i=1}^N \rho_i m_i^{(k)}}. \quad (3.7)$$

By multiplying the length and width, the area of the OBB for component k can be calculated, which is used as an approximation of the cost of die-set materials:

$$A^{(k)} = \prod_{j=1}^2 l_j^{(k)}. \quad (3.8)$$

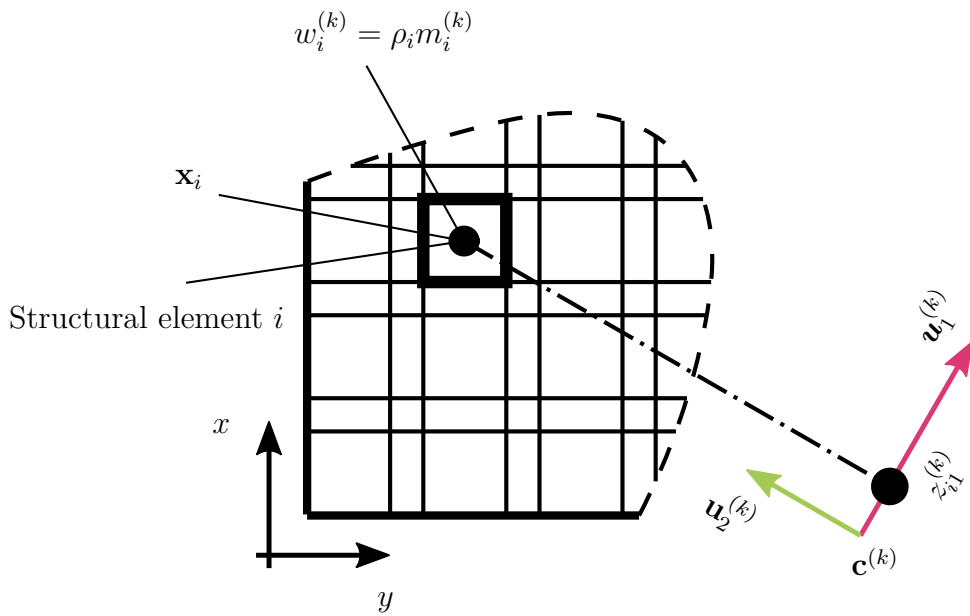


Figure 3.4: Computation of the bounding box with the continuously relaxed design variables. This is a mesh-dependent formulation. (The mesh-independent formulation is presented in Figure 5.1.)

3.5.2 Die machining cost

The die machining cost for component k is modeled as proportional to a complexity index, which is the perimeter of each component normalized by its OBB size [86]:

$$X^{(k)} = \frac{P^{(k)}}{\sqrt{A^{(k)}}}, \quad (3.9)$$

where $P^{(k)}$ is the perimeter length to be sheared during stamping. By generalizing the perimeter calculation, previously developed for single-piece topology optimization [28], $P^{(k)}$ can be approximated as the total variation of the density design variables, weighted with the membership design variables, in a matrix form:

$$P^{(k)} = \sum_{i=1}^{nely-1} \sum_{j=1}^{nelx} |m_{ij}^{(k)} \rho_{ij} - m_{i+1,j}^{(k)} \rho_{i+1,j}| + \sum_{i=1}^{nely} \sum_{j=1}^{nelx-1} |m_{ij}^{(k)} \rho_{ij} - m_{i,j+1}^{(k)} \rho_{i,j+1}|, \quad (3.10)$$

where $nelx$ and $nely$ are the number of structural elements in x - and y -axis in the design domain. Due to the need of differentiability with respect to ρ_i and \mathbf{m}_i , the absolute operator in Equation (3.10) is numerically approximated as:

$$|x| \equiv \sqrt{(1 + 2\varepsilon)x^2 + \varepsilon^2} - \varepsilon, \quad (3.11)$$

where ε is a small positive real number balancing the accuracy and smoothness of the approximation.

It is noted that the manufacturing cost models discussed in this section would not be in the dollar-to-dollar level accuracy. It is due, mainly, to the numerical approximations involved and other unknown factors, such as machine specifications and labor costs. However, in the concept generation stage, for which topology optimization is most suitable, the proposed simplified manufacturing cost models would be adequate for capturing the trend of manufacturing costs.

3.6 Optimization formulation

The overall MTO-S problem is formulated as the minimization of structural compliance subject to constraints on the cost of die-set materials and die machining,

summarized as follows:

$$\begin{aligned}
& \underset{\boldsymbol{\rho}, \mathbf{m}^{(1)}, \dots, \mathbf{m}^{(K)}}{\text{minimize}} && F(\mathbf{u}) \\
& \text{subject to} && g_1 := \sum_{k=1}^K A^{(k)}(\boldsymbol{\rho}, \mathbf{m}^{(k)}) \leq \alpha^* \\
& && g_2 := \sum_{k=1}^K \frac{P^{(k)}(\boldsymbol{\rho}, \mathbf{m}^{(k)})}{\sqrt{A^{(k)}(\boldsymbol{\rho}, \mathbf{m}^{(k)})}} \leq \beta^* \\
& && \text{for } i = 1, 2, \dots, N : \quad , \quad (3.12) \\
& && \rho_i \in [0, 1] \\
& && g_3^{(i)} := \sum_{k=1}^K m_i^{(k)} = 1 \\
& && \text{for } k = 1, 2, \dots, K \text{ and } i = 1, 2, \dots, N : \\
& && m_i^{(k)} \in [0, 1]
\end{aligned}$$

where $\boldsymbol{\rho}$ and $\mathbf{m}^{(k)}$ are the density and membership design variables; K is the prescribed, maximum allowable number of components; N is the number of structural elements; F is the structural compliance objective defined in Equation 3.4; $A^{(k)}$ is the approximate OBB area of component k ; α^* is the maximum allowable total OBB area (\approx die-set material cost); $P^{(k)}$ is the approximate perimeter of component k ; and β^* is the maximum allowable total complexity (\approx die machining cost). The traditional volume fraction constraint for topology optimization is not included, because the OBB area constraint serves a similar role as the volume fraction constraint. The additional constraint on memberships for each element i ensures the unity of the total fractional memberships. Finally, both densities and memberships take continuous values ranging from zero to one.

3.7 Numerical results

This section presents numerical results of the gradient-based MTO-S. A cantilever example is presented in Section 3.7.1 to show its detailed optimization iterations. Another Messerschmidt-Bölkow-Blohm (MBB) beam example is presented in Section 3.7.2 to demonstrate the effect of the die machining cost constraint. Their design domains and boundary conditions are summarized in Figure 3.5. Symmetry bound-

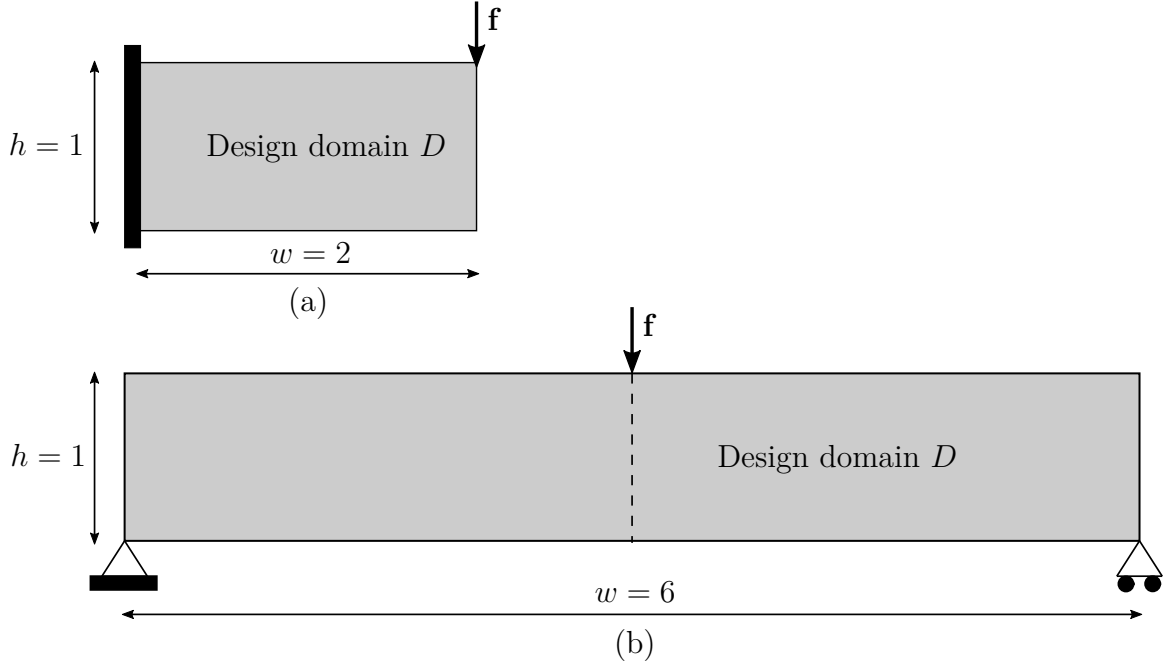


Figure 3.5: Design domain and boundary condition settings for the (a) cantilever example; (b) Messerschmidt-Bölkow-Blohm beam example.

any conditions were applied to the MBB example. The ratio of the width of Type A joint elements to the length of structural elements was set as 0.2 for the cantilever example. For problems with finer mesh, which was the case for the MBB example, this ratio was set to 1. The ratio of the Young’s modulus of joint elements to that of structural elements was set as 0.2, reflecting that spot-welding joints are less stiff than base structures. This value can also be set differently per design requirements. The convergence criteria for optimization are set as follows. The lower bounds on the size of a step and on the change in the value of the objective function were all set as $1e - 5$. The maximum number of iterations was set as 100 and 400 for the cantilever and MBB examples, respectively. The optimizer would terminate when any of the above three criteria was met.

The constrained optimization problem in Equation (3.12) was solved by the interior-point method using the Matlab `fmincon`. The first derivatives of the objective and constraints were analytically derived with the assistance of the Matlab symbolic math toolbox, whereas the Hessian was numerically approximated using a finite-difference approach. The optimization usually converges within a few hundreds of iterations. For comparison, to solve similarly sized problems, previous methods based on non-gradient discrete formulations and genetic algorithms required significantly more function evaluations, e.g., 100000 in [84], and 60000 in [85].

The finite-difference approximation of Hessian inevitably brings computational efficiency concerns for large-scale studies. More computationally efficient implementations can be achieved by, e.g., using the Broyden–Fletcher–Goldfarb–Shanno (BFGS) method to return a quasi-Newton approximation to the Hessian, deriving the Hessian analytically, and using first-order optimization solvers that do not require Hessian. In the past attempts by the authors, the BFGS required more iterations for convergence, likely due to its relatively inaccurate approximation compared with finite-differencing. Also, the algorithms that require only the first-order gradients did not perform well, due to the large number of linear equality constraints for membership unity.

3.7.1 Iterative details: cantilever

The proposed gradient-based continuous MTO-S is first applied to a 10×5 (structural element mesh) cantilever example to show its detailed optimization iterations. Its design domain D and boundary condition settings are presented in Figure 3.5(a).

The number of components was set as $K = 3$. As seen in Figure 3.6, at iteration 1, density and membership design variables ρ_i and $m_i^{(k)}$ were uniformly initialized as 0.4 and $1/K$ respectively. Due to the relatively coarse mesh in this example, the complexity (die machining cost) constraint was not included.

Figure 3.6 shows the iterative history of the density design variable ρ_i in the first row, membership design variable $m_i^{(k)}$ in the second row, and intermediate components (product of the two) $\rho_i m_i^{(k)}$ in the third row. The red and green lines indicate the orientation of bounding boxes. It can be seen that centers of the bounding boxes also update during optimization. As seen from the iterative details, membership variable $m_i^{(k)}$ started to converge to a certain component at iteration 15. At the end of optimization, component boundaries were almost black and white when optimization converged at iteration 74.

Though several elements near the component boundaries still had fractional memberships, they were resolved by assigning those elements to the component with the largest $m_i^{(k)}$. The post-processed multi-component topology design is shown in Figure 3.7(a). The thin gray elements between every two components are the resulting joint locations with the less stiff Young’s modulus. For a comparison, the optimized single-piece topology design using the conventional SIMP approach without regularization is presented in Fig. 3.7(b). Even without the complexity constraint that would penalize checkerboard patterns, they did not appear in the result in Fig. 3.7(a). It appears that the combination of having no volume constraint and the introduction

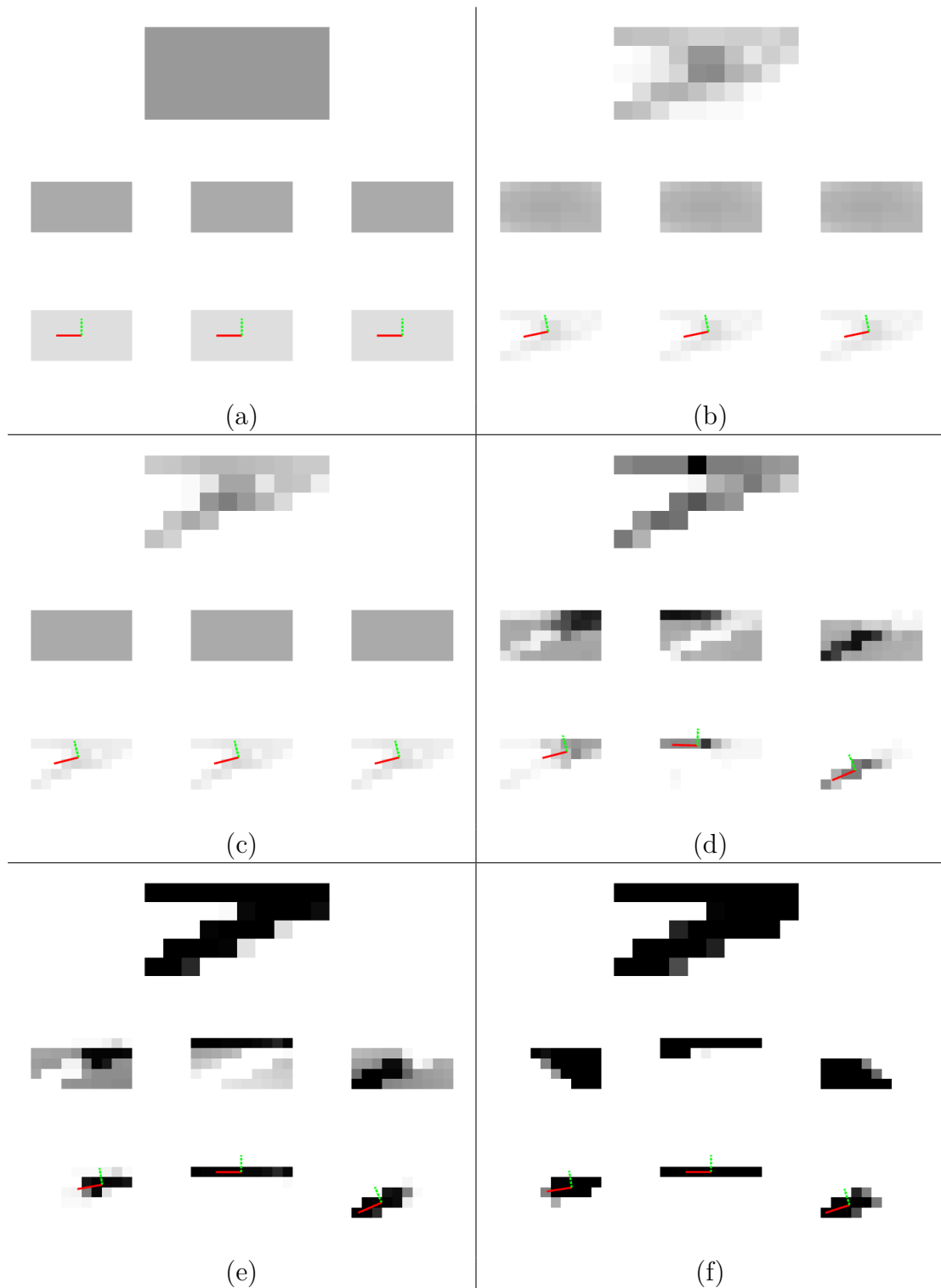


Figure 3.6: Optimization iterative details for the cantilever example at (a) iteration 1; (b) iteration 5; (c) iteration 10; (d) iteration 15; (e) iteration 30; and (f) iteration 74.



Figure 3.7: A comparison between the multi-component topology and conventional, single-piece topology for the cantilever example. (a) The optimized multi-component cantilever topology design. The gray regions indicate joint locations (assuming spot-welding joints) with the smaller Young’s modulus than base structural materials; (b) the conventional, single-piece cantilever topology design.

of the total bounding box area constraint encourages designs without checkerboard in order to have more materials. The special domain discretization also contributes to the elimination of checkerboard patterns in the optimized topology.

Figure 3.8 presents the optimization convergence history. Since the total bounding box area constraint was violated initially, the optimizer attempted to decrease the total bounding box area in early iterations while sacrificing the compliance objective. Once the total bounding box area constraint reached the prescribed limit α^* , the optimizer continued by minimizing the compliance objective, driven mainly by the compliance sensitivity while keeping the manufacturing constraint active. The optimization converged in 74 iterations when the termination criterion for the change of objective value was met.

3.7.2 Die machining cost: Messerschmidt-Bölkow-Blohm beam

This section discusses the effects of the complexity (i.e., die machining cost) constraint limit β^* through a 240×40 MBB example. Its design domain and boundary condition settings are shown in Figure 3.5(b). Only half of the design domain was optimized because of the symmetry in boundary conditions and the initial design domain. While checkerboard patterns were discouraged by the new total bounding box area constraint and the special domain discretization, undesired small features would still appear for problems with increased mesh, which in turn would increase the die machining cost. Therefore, a complexity constraint, as described in Equation (3.9),

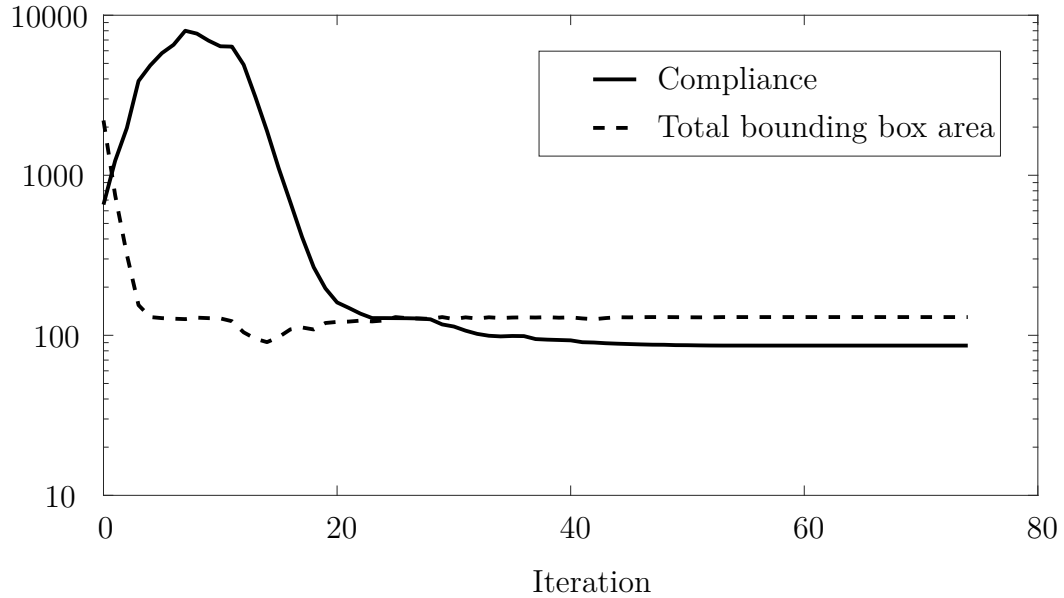


Figure 3.8: Convergence history of the cantilever example. Due to the relatively coarse mesh in this example, the complexity (die machining cost) constraint was not included.

was introduced to control the die machining cost.

Figure 3.9 shows three multi-component topology designs with different settings of the complexity constraint limit β^* . The same value of the total bounding box area constraint limit α^* was applied to all three cases. Figure 3.9 also presents the “true” bounding box and “true” perimeter for each decomposed component. Lower complexity indices 3.45 and 3.03 were achieved by decreasing the complexity constraint limit β^* compared with the baseline 3.99 with the limit $\beta^* = \infty$ (i.e., no complexity control). Once again, even without the complexity control, checkerboard patterns did not appear, as seen in Figure 3.9(a). With the decrease of β^* , the overall complexity of the optimized topology could be reduced, resulting in less expensive overall stamping die machining cost. Similar effect on the complexity control could also be achieved by filtering methods. It was observed that the complexity constraint limit β^* had little influence on the component decomposition, but greater effect on the overall base topology of the multi-component structures.

3.8 Chapter summary

This chapter proposed a topology optimization method for structures made of sheet metal components. With the continuous density and membership design variables and the cost modeling of stamping dies, simultaneous optimization of the overall

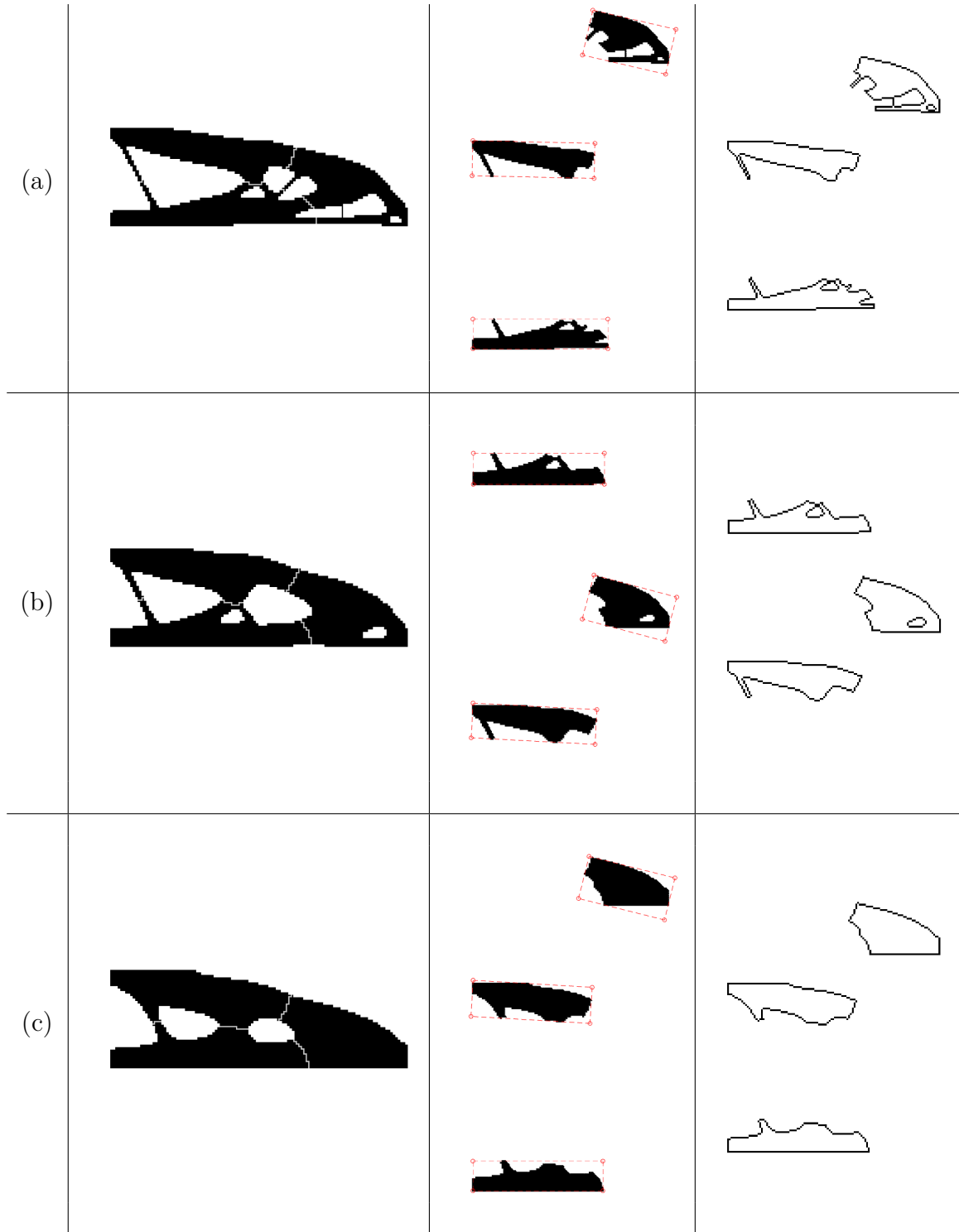


Figure 3.9: Multi-component topology designs of the Messerschmidt-Bölkow-Blohm beam example with different levels of complexity control. (a) High die machining cost (complexity index: 3.99); (b) moderate die machining cost (complexity index: 3.45); (c) low die machining cost (complexity index: 3.03). From left to right: multi-component topology, “true” bounding box, and “true” perimeter.

base topology and component decomposition was realized in a continuously relaxed manner. A continuously relaxed joint stiffness model was also developed to consider the component interface property in the structural performance analysis. The simplified cost model for stamping dies was developed based on an empirical cost model [86]. As a result, MTO was, for the first time, solved using a gradient-based method, which demonstrated promising potentials to dramatically improve the computational efficiency over previous discrete formulations solved by genetic algorithms (e.g., [84, 85]).

However, the development of the gradient-based MTO method was still in its infancy. Some major limitations of MTO-S are acknowledged as follows. Though the complexity control can help generate mesh-independent results without checkerboard patterns, due to the special domain discretization and mesh-dependent joint stiffness modeling, the overall MTO-S formulation is still deemed mesh-dependent. Moreover, to ensure the membership unity for each structural element, a large number of equality constraints are required in the MTO-S formulation. Equality constraints are generally not favored by gradient-based optimization, especially with large quantities. Therefore, the MTO-S problem was solved with the need of Hessian calculation. Accurate Hessian calculation, however, is often computationally expensive.

To address the limitations discussed above, improved MTO formulations, which are mesh-independent and do not require the many membership unity equality constraints, will be discussed in Chapter 4 and Chapter 5.

CHAPTER 4

Multi-component topology optimization for composite manufacturing

This chapter presents the MTO application to structures made of multiple composite components (substructures) with tailored material orientations, termed the Multi-component Topology Optimization for Composite manufacturing (MTO-C). Recent societal demand for energy saving has prompted increased emphasis on lightweighting in structural design. Due to its high strength-to-weight characteristic, the use of composite materials in structural applications has become a popular alternative to replace traditional materials, e.g., steel, aluminum. Advanced examples appear routinely on spacecraft and aircraft. With the latest development of economical composite manufacturing processes, e.g., resin transfer molding, the use of composite materials for high-volume products at acceptable cost becomes possible, e.g., automotive structures.

4.1 Why multiple components for composite structures

While the utilization of fiber reinforced composite materials can dramatically cut down structural weight, a significant trade-off exists between the production cost and structural performance. Variable Axial Composite (VAC) is a class of composite materials reinforced by long fibers with varying orientations, produced by advanced manufacturing processes such as Automated Tape Layout (ATL), Tailored Fiber Placement (TFP), and Continuous Fiber Printing (CFP). Generally speaking, manufacturing processes with higher freedom in orientation control can produce higher performing composites, but cost more than those with lower freedom in orientation control. For this reason, the conventional fixed-axis composites, despite their inferior performance, are widely adopted in many commercial applications, especially for large-scale and mass-produced structural products.

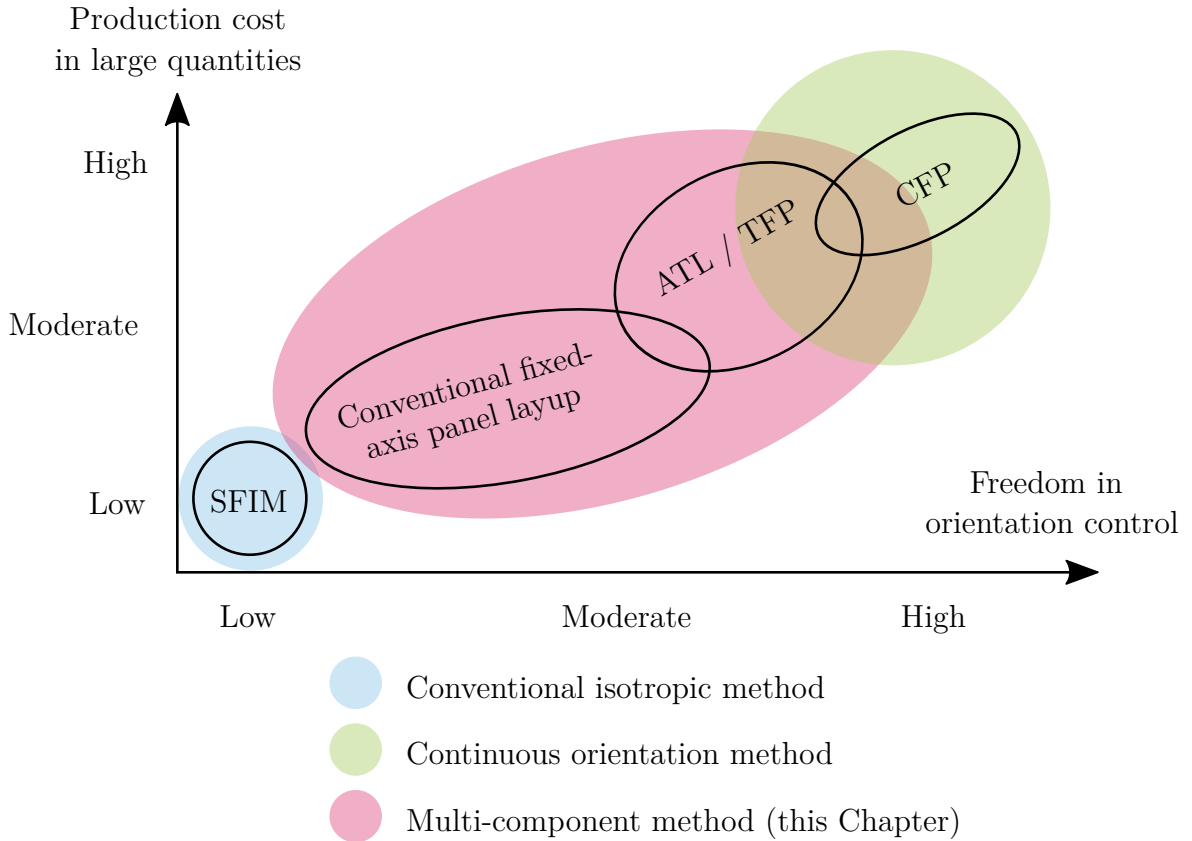


Figure 4.1: A qualitative comparison of different composite manufacturing processes in terms of the production cost in large quantities (vertical axis) and freedom in orientation control (horizontal axis). As a manufacturing process becomes more economical for mass production, it sacrifices freedom in controlling fiber orientations. The suitability of different topology design methods is also plotted. (SFIM: short fiber injection molding; ATL: automated tape layout; TFP: tailored fiber placement; CFP: continuous fiber printing)

Figure 4.1 shows a comparison of typical composite manufacturing processes in terms of their freedom in fiber orientation control and suitability for economical production in large quantities. The injection molding of resins mixed with short fibers, also known as Short Fiber Injection Molding (SFIM), is included as a baseline benchmark, which approximately performs as isotropic materials due to random and discontinuous fiber orientations. Shown also in Figure 4.1 is the suitability of different topology optimization methods for designing structures with anisotropic material orientations. Structures designed by the continuous orientation methods are most suitable for production by the manufacturing processes with the highest freedom in orientation control, e.g., CFP. Conversely, structures designed by the conventional isotropic topology optimization methods are well suited for production by the man-

ufacturing processes at the lowest end of orientation control and cost, e.g., SFIM, since materials perform almost as isotropic materials. In between these extreme is a space for the manufacturing processes with moderate orientation control and cost, e.g., conventional layup of fixed-axis composite panels, TFP, and ATL. Structures that are suitable for production by these manufacturing processes should be made of a relatively small number of distinct substructures (components), each of which has a single material orientation, possibly with small variations for TFP and ATL, tailored for overall structural performances. The MTO-C method proposed in this chapter intends to fill this gap.

4.2 Prior art: anisotropic topology optimization

Motivated by the recent advent of composite manufacturing processes, much effort has been made to develop topology optimization methods for designing anisotropic material orientations. Based on their mathematical formulations, the existing methods can be categorized into two major classes: the discrete orientation method and the continuous orientation method.

The first class optimizes the material orientations among a prescribed set of alternative discrete angles, hence termed the discrete orientation method. Haftka and colleagues developed discrete optimization formulations for selecting fiber orientation angles from a prescribed discrete set [94, 95, 96, 97], which were solved using genetic algorithms. To enable the sensitivity analysis and the efficient gradient optimization, Lund and colleagues proposed the Discrete Material Optimization (DMO) approach [62, 98, 99], which relaxed the original combinatorial problem to a continuous optimization problem through material tensor aggregation and penalization. As a result of efficient gradient optimization, the prescribed set of alternative discrete angles can be of a larger size, but it remains as an input to the optimization. Other variations following the DMO concept have also been developed, e.g., the shape function with penalization method [100] and its generalization to more choices of alternative discrete angles [101], and the peak function approach [102]. By introducing additional unity constraints on the sum of the fractional selections of alternative angles, other formulations [87, 88] have been proposed as alternatives to the DMO formulation. A large number of unity constraints associated with these formulations, however, imposes challenges on optimization solvers in large-scale problems. Despite its popularity and intuitive formulation, these discrete orientation methods suffer from a common issue: the need of a prescribed set of alternative discrete angles as an

input. While, in theory, a set of infinitely large number of alternative discrete angles can contain the true optimal angles, the methods are limited to find the best angles only among the given alternatives, which may well be suboptimal. In addition, while some extensions intend to address the selection of different angles for each substructure (typical for multi-panel construction of composite structures), the boundaries between substructures are simply determined by the prescribed division of the design domain, typically squares, without optimization processes.

The second class optimizes the material orientation within a continuous range of angles, not among alternative discrete angles, hence termed the continuous orientation method. The continuous fiber angle optimization [103, 104] is a method where the orientation angles are regarded as continuous design variables that can take range $[0, 2\pi]$. While intuitive, this angular representation suffers from the convergence to the local minima due to the periodic nature of material properties with respect to the orientation angles. To overcome this issue, Nomura et al. (2015) [105] proposed the use of Cartesian components of the orientation vector as design variables combined with an isoparametric projection, and empirically demonstrated superior convergence behaviors.

4.3 Design field configuration and regularization

As demonstrated in Figure 4.2, in addition to the original two-layer (density ρ and membership $m^{(k)}$) design field presented in the general MTO formulation, discussed in Chapter 2, a third layer of orientation design field $\vartheta^{(k)}$ is added, which is a Cartesian vector $(\zeta^{(k)}, \zeta^{(k)})$ representing the orientation of each design point in component k . Depending on the radius of the regularization filter applied to the orientation field, the resulting material orientation for each component can either be unidirectional or curvilinear. To resolve the mesh-dependent issue of the MTO-S formulation, regularizations are applied to all three-layer design field using the Helmholtz PDE filtering and Heaviside projection, detailed in [38].

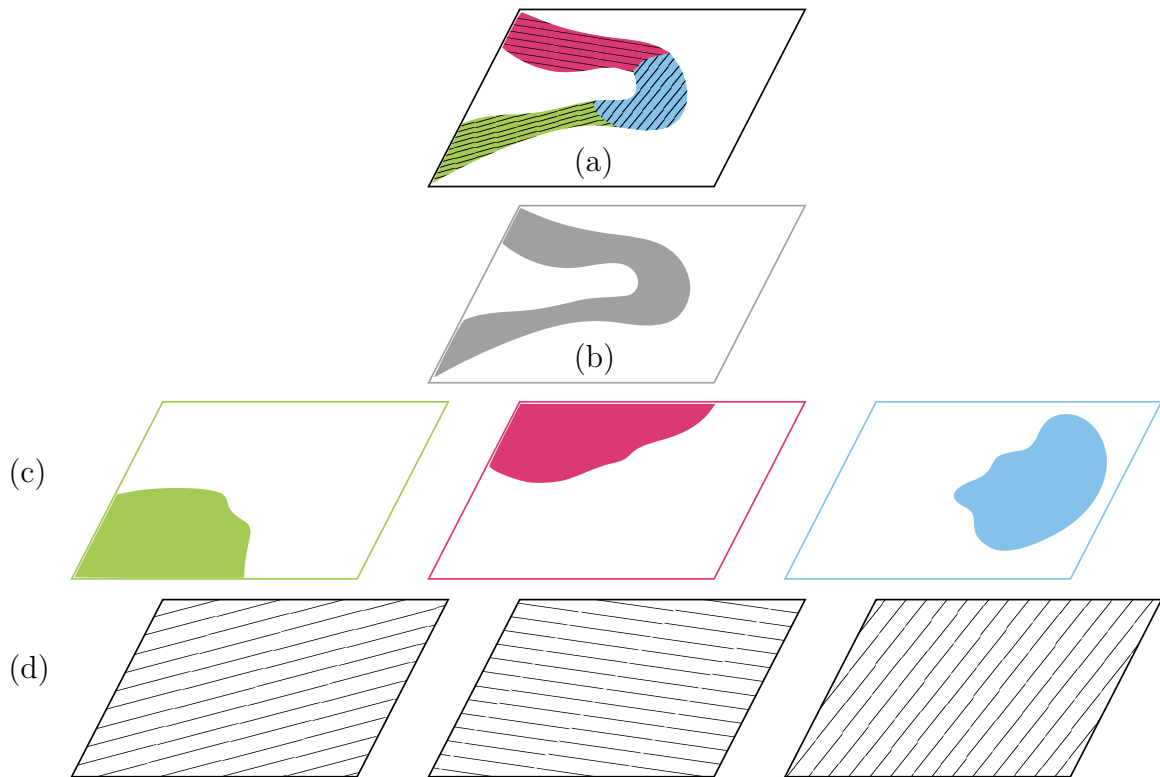


Figure 4.2: Demonstration of the three-layer design field and the resulting simulation model for an example case of number of components $K = 3$. (a) Simulation model; (b) density field ρ ; (c) membership field $m^{(k)}$; (d) orientation field $\vartheta^{(k)}$. (The material orientation for each component can be either unidirectional or curvilinear based on the regularization filter radius used. This figure only shows the unidirectional case.)

4.3.1 Density field

In a prescribed, fixed design domain D , a characteristic function χ is defined to describe the material domain Ω_d to be optimized:

$$\chi(\mathbf{x}) = \begin{cases} 0 & \text{for } \forall \mathbf{x} \in D \setminus \Omega_d, \\ 1 & \text{for } \forall \mathbf{x} \in \Omega_d \end{cases}, \quad (4.1)$$

where \mathbf{x} stands for a design point in D and $\chi(\mathbf{x})$ is defined by a scalar function ϕ and the Heaviside function H such that:

$$\chi(\mathbf{x}) = H(\phi(\mathbf{x})) = \begin{cases} 0 & \text{for } \forall \mathbf{x} \in D \setminus \Omega_d, \\ 1 & \text{for } \forall \mathbf{x} \in \Omega_d \end{cases}. \quad (4.2)$$

To eliminate checkerboard patterns therefore generating mesh-independent results, the Helmholtz PDE filter [37] is introduced to regularize ϕ :

$$-R_\phi^2 \nabla^2 \tilde{\phi} + \tilde{\phi} = \phi, \quad (4.3)$$

where R_ϕ is the filter radius, and $\tilde{\phi}$ is the filtered field. Then the density field ρ can be defined by an additional regularized Heaviside function \tilde{H} :

$$\rho = \tilde{H}(\tilde{\phi}). \quad (4.4)$$

After the series of regularization from ϕ to ρ , the resulting density field ρ is bounded between 0 and 1.

4.3.2 Material orientation vector field

Following the Cartesian representation of continuous angles proposed in [105], the original material orientation vector field $v^{(k)} = (\xi^{(k)}, \eta^{(k)})$, bounded by box constraint $v^{(k)} \in [-1, 1]^D \times [-1, 1]^D$ is first regularized by the Helmholtz PDE filter:

$$-\mathbf{R}_v \nabla^2 \begin{bmatrix} \tilde{\xi}^{(k)} \\ \tilde{\eta}^{(k)} \end{bmatrix} + \begin{bmatrix} \tilde{\xi}^{(k)} \\ \tilde{\eta}^{(k)} \end{bmatrix} = \begin{bmatrix} \xi^{(k)} \\ \eta^{(k)} \end{bmatrix}, \quad (4.5)$$

where $\mathbf{R}_v = R_v^2 \mathbf{I}$; R_v is the filter radius; \mathbf{I} is an identity matrix. $\tilde{v}^{(k)} = (\tilde{\xi}^{(k)}, \tilde{\eta}^{(k)})$ is the filtered orientation field. Then, the (unbounded) $\tilde{v}^{(k)}$ is projected back to the

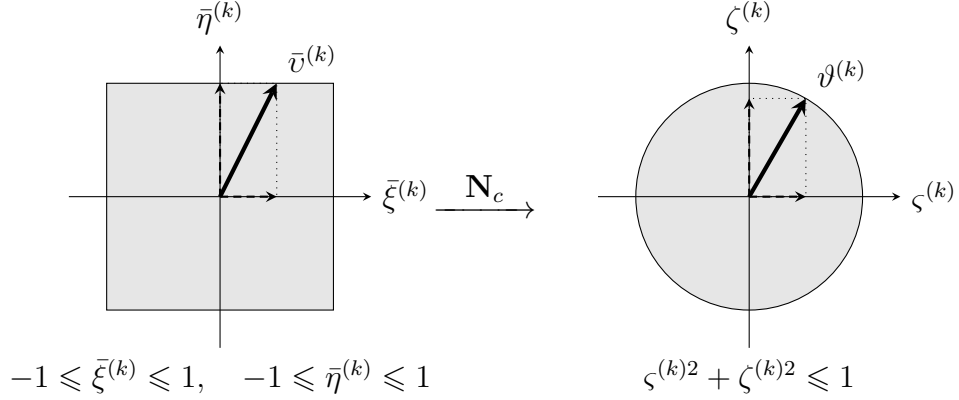


Figure 4.3: Coordinate transformation for the Cartesian orientation representation through an isoparametric projection method.

original box constraint with a regularized Heaviside function \tilde{H} :

$$\bar{v}^{(k)} = \begin{bmatrix} \bar{\xi}^{(k)} \\ \bar{\eta}^{(k)} \end{bmatrix} = \begin{bmatrix} 2\tilde{H}(\bar{\xi}^{(k)} - 1) \\ 2\tilde{H}(\bar{\eta}^{(k)} - 1) \end{bmatrix}. \quad (4.6)$$

As illustrated in Figure 4.3, the regularized orientation vector field $\bar{v}^{(k)}$ in a box domain is then projected to a circular domain through an isoparametric projection \mathbf{N}_c :

$$\vartheta^{(k)} = \mathbf{N}_c(\bar{v}^{(k)}) = \begin{bmatrix} N_{cx}(\bar{\xi}^{(k)}, \bar{\eta}^{(k)}) \\ N_{cy}(\bar{\xi}^{(k)}, \bar{\eta}^{(k)}) \end{bmatrix}. \quad (4.7)$$

where $\vartheta^{(k)} = (\zeta^{(k)}, \zeta^{(k)})$ is the projected orientation vector field. The transformation from a box domain to a circular domain eliminates the need of the quadratic constraint $\bar{\xi}^{(k)2} + \bar{\eta}^{(k)2} = 1$ for each design point, and ensures singularity-free numerical analyses. For the detailed implementation of the isoparametric projection \mathbf{N}_c , readers are referred to [105].

By setting different values for R_v in Equation (4.5), the maximum allowable curvature of the material orientation in each component k can be explicitly controlled. With a large enough R_v , the resulting material orientation can be unidirectional.

4.3.3 Component membership vector field

Following the similar regularization scheme as material density and orientation design fields, the original membership vector field $\mu^{(k)}$ is transformed to $\tilde{\mu}^{(k)}$ and then $\bar{\mu}^{(k)}$ through the Helmholtz PDE filter and regularized Heaviside projection. For each

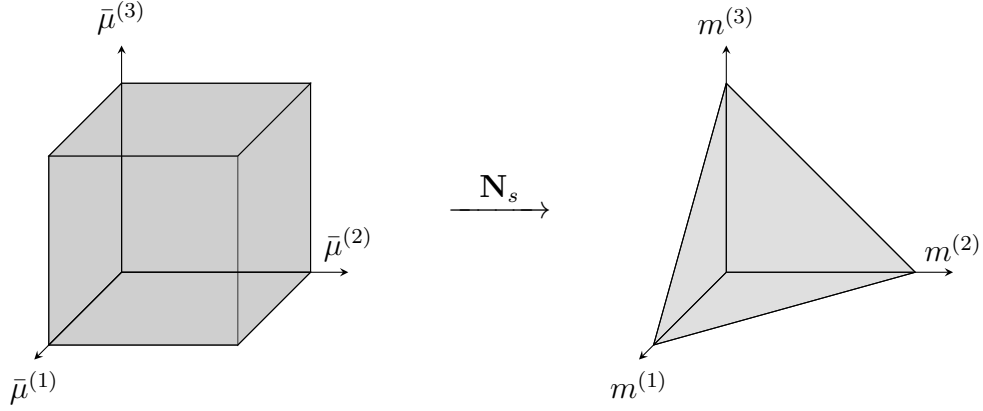


Figure 4.4: Coordinate transformation for the component membership design field through a K -dimensional cube-to-simplex projection for an example case of $K = 3$.

design point, the resulting $\bar{\boldsymbol{\mu}} = (\bar{\mu}^{(1)}, \bar{\mu}^{(2)}, \dots, \bar{\mu}^{(K)})$ is bounded by a K -dimensional unit cube $[0, 1]^K$. As illustrated in Figure 4.4, the regularized component membership vector field $\bar{\boldsymbol{\mu}}$ in a cube domain is then projected to a standard simplex domain through an isoparametric projection \mathbf{N}_s :

$$\mathbf{m} = \mathbf{N}_s(\bar{\boldsymbol{\mu}}) \quad (4.8)$$

where $\mathbf{m} = (m^{(1)}, m^{(2)}, \dots, m^{(K)})$ is the projected component membership vector field. The transformation from a cube domain to a standard simplex domain eliminates the need of unity constraint $m^{(1)} + m^{(2)} + \dots + m^{(K)} = 1$ for each design point and ensures singularity-free numerical analyses.

4.4 Cube-to-simplex projection method

The cube-to-simplex projection $\mathbf{N}_s = (N_s^{(1)}, N_s^{(2)}, \dots, N_s^{(K)})$ is defined as

$$m^{(k)} = N_s^{(k)}(\bar{\boldsymbol{\mu}}) = \sum_{i=1}^M s_i^{(k)} \left\{ (-1)^{(K + \sum_{k=1}^K c_i^{(k)})} \prod_{k=1}^K (\bar{\mu}^{(k)} + c_i^{(k)} - 1) \right\}, \quad (4.9)$$

where $M = 2^K$ and $c_i^{(k)} \in \{0, 1\}$ are the number of vertices and the k -th element of the i -th vertex of a K -dimensional unit cube, respectively, and $s_i^{(k)}$ is vertex $c_i^{(k)}$

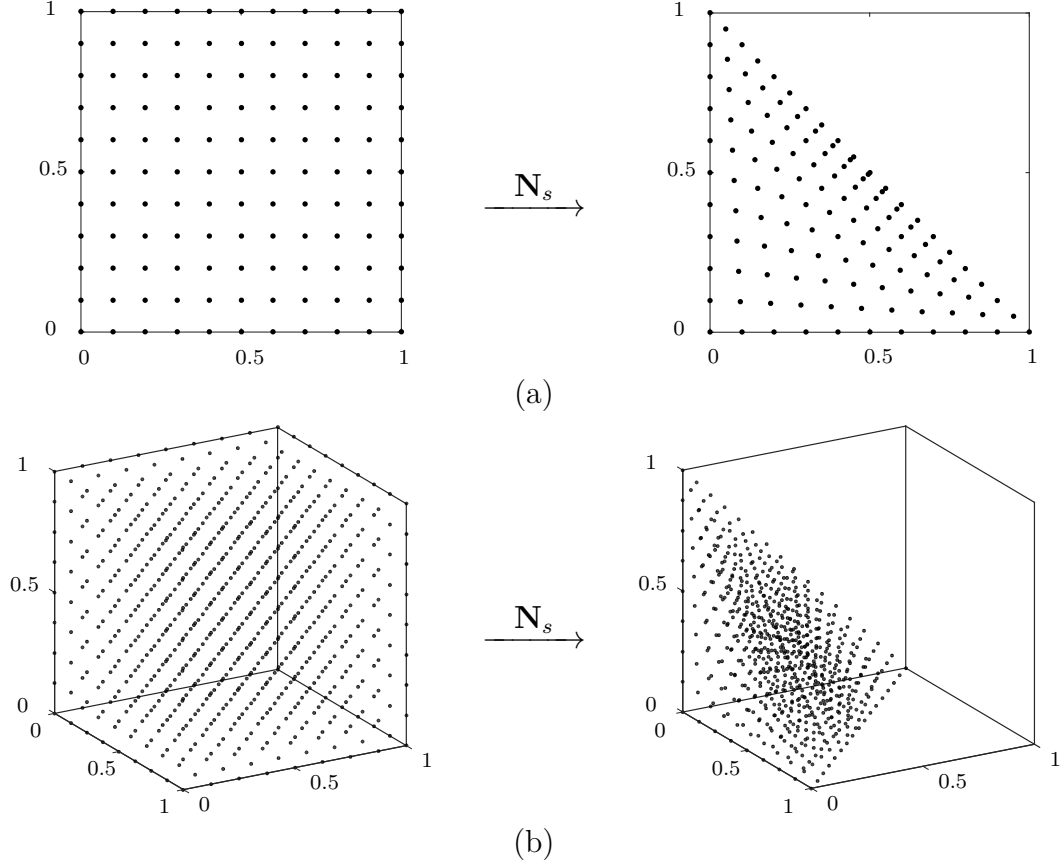


Figure 4.5: The cube-to-simplex projection examples for cases of (a) $K = 2$ and (b) $K = 3$.

projected to a K -dimensional standard simplex domain, given as:

$$s_i^{(k)} = \begin{cases} \frac{c_i^{(k)}}{\sum_{k=1}^K c_i^{(k)}} & \text{if } \sum_{k=1}^K c_i^{(k)} \geq 1 \\ 0 & \text{otherwise} \end{cases}. \quad (4.10)$$

Figure 4.5 illustrates the projection of sampled points in a unit cube using Equations (4.8)–(4.10). While the figure shows only for cases $K = 2$ and $K = 3$, the proposed cube-to-simplex projection in Equations (4.8)–(4.10) works for an arbitrary number of dimensions.

4.5 Elasticity tensor composition

By adopting the multi-phase SIMP-like formulation reported in past literature, the elasticity tensor at each design point can be composed by overlaying the elasticity

tensor for each component:

$$\mathbf{C} = \rho^{P_d} \sum_{k=1}^K (m^{(k)})^{P_m} \mathbf{C}^{(k)}, \quad (4.11)$$

where \mathbf{C} and $\mathbf{C}^{(k)}$ are the composed elasticity tensor and the elasticity tensor for component k , respectively, and P_d and P_m are the penalization parameters for density and component membership, respectively.

This way of composing the elasticity tensor for each phase (component in this case) was considered the simplest choice for multi-phase topology optimization according to [62]. However, it does not satisfy the unity constraint $m^{(1)} + m^{(2)} + \dots + m^{(K)} = 1$, which allows only one of phase fields (component membership fields in this case) $m^{(k)}$ converging to 1. Rather, Equation (4.11) often favors all phase fields (component membership fields in this case) $m^{(k)}$ converging to 1, since it would maximize the composed tensor \mathbf{C} with respect to $m^{(k)} \in [0, 1]$. To resolve this issue, different projection methods for phase fields have been proposed. Sigmund and colleagues [29, 106] originally proposed a two-phase formulation for topology optimization, which has later been extended to more phases. Stegmann and Lund (2005) proposed another projection method, termed the DMO [62]. The proposed cube-to-simplex projection discussed in Section 4.4 can be seen an alternative approach to satisfy the membership unity condition. Through the proposed cube-to-simplex projection, the vertices in a unit cube that violate the unity condition (i.e., the ones outside of a standard simplex attached to the cube) are projected inside of a cube and the convergence to them is discouraged by the power law penalization.

By incorporating the material orientation field $\vartheta^{(k)}$ into component elasticity tensor $\mathbf{C}^{(k)}$, the modified composed elasticity tensor \mathbf{C} can be rewritten as:

$$\mathbf{C} = \rho^{P_d} \sum_{k=1}^K (m^{(k)})^{P_m} \mathbf{C}^{(k)}(\vartheta^{(k)}), \quad (4.12)$$

with the transformed anisotropic tensor $\mathbf{C}^{(k)}(\vartheta^{(k)})$, given as:

$$\mathbf{C}^{(k)}(\vartheta^{(k)}) = \mathbf{C}_i + \hat{\mathbf{T}}^{-1}(\vartheta^{(k)}) \cdot (\mathbf{C}_u - \mathbf{C}_i) \cdot \hat{\mathbf{T}}'(\vartheta^{(k)}), \quad (4.13)$$

where \mathbf{C}_u is a unrotated anisotropic tensor; \mathbf{C}_i is an isotropic component. $\hat{\mathbf{T}}$ and $\hat{\mathbf{T}}'$ are transformations to rotate a tensor to a direction based on $\vartheta^{(k)}$. For the detailed explanation and derivation of the transformed anisotropic tensor, readers are referred

to [105].

4.6 Optimization formulation

The overall optimization problem of multi-component topology and material orientation design can be stated as follows:

$$\begin{aligned}
& \underset{\substack{\phi \\ \mu^{(1)}, \dots, \mu^{(K)} \\ v^{(1)}, \dots, v^{(K)}}}{\text{minimize}} & F(\mathbf{u}) \\
& \text{subject to} & g_1 := A_d - V^* \leq 0 \\
& & \phi \in [-1, 1]^D, \\
& & \text{for } k = 1, 2, \dots, K : \\
& & g_2^{(k)} := -B^{(k)} + (1 - \delta) \leq 0 \\
& & \mu^{(k)} \in [-1, 1]^D \\
& & v^{(k)} \in [-1, 1]^D \times [-1, 1]^D
\end{aligned} \tag{4.14}$$

where \mathbf{u} is the displacement field obtained by solving the static equilibrium equations; $F(\mathbf{u})$ is the objective function for a structural performance; K is the prescribed, maximum allowable number of components; g_1 is the material volume constraint with upper bound V^* ; $g_2^{(k)}$ is the constraint to ensure the material anisotropy for the k -th component with small constant δ ; and A_d and $B^{(k)}$ are given as:

$$\begin{aligned}
A_d &= \int_D \rho \, d\Omega \\
B^{(k)} &= \frac{1}{A_d} \int_D \rho \left\| \vartheta^{(k)} \right\| \, d\Omega
\end{aligned} \tag{4.15}$$

In the case of the minimization of structural compliance as discussed in the following examples, the objective function can be stated as:

$$F(\mathbf{u}) = \frac{1}{2} \int_D \boldsymbol{\sigma}^\top \boldsymbol{\epsilon} \, d\Omega, \tag{4.16}$$

Table 4.1: Material properties for the numerical examples.

Symbol	Value	Description
E_f	1	Young's modulus of reinforcement material
E_m	1/15	Young's modulus of matrix material
ν_f	0.22	Poisson ratio of reinforcement material
ν_m	0.38	Poisson ratio of matrix material
f_f	0.5	fiber fraction for anisotropic material

and the static equilibrium equations can be stated as:

$$\begin{aligned}
 -\nabla \cdot \boldsymbol{\sigma} &= \mathbf{0} && \text{in } D \\
 \mathbf{u} &= \mathbf{0} && \text{on } \Gamma_d, \\
 \boldsymbol{\sigma} \cdot \mathbf{n} &= \mathbf{t} && \text{on } \Gamma_n
 \end{aligned} \tag{4.17}$$

where $\boldsymbol{\sigma} = \mathbf{C} \cdot \boldsymbol{\epsilon}$ is the stress field; $\boldsymbol{\epsilon}$ is the strain field; Γ_d is the Dirichlet boundary defined by zero prescribed displacement; and Γ_n is the Neumann boundary defined by the normal \mathbf{n} and the prescribed traction \mathbf{t} .

4.7 Numerical results

This section presents several numerical examples in 2D on compliance minimization based on a simplified orthotropic material model per [107]:

$$\begin{aligned}
 E_1 &= f_f E_f + (1 - f_f) E_m \\
 E_2 &= \{f_f / E_f + (1 - f_f) / E_m\}^{-1} \\
 G_{12} &= \{f_f / G_f + (1 - f_f) / G_m\}^{-1} . \\
 \nu_{12} &= f_f \nu_f + (1 - f_f) \nu_m \\
 \nu_{21} &= \{f_f \nu_f + (1 - f_f) \nu_m\} \frac{E_2}{E_1}
 \end{aligned} \tag{4.18}$$

Table 4.1 summarizes the values of the material properties in Equation (4.18) used in the numerical examples.

The results obtained by the proposed multi-component topology and orientation optimization were compared to the ones by 1) the single-piece topology optimization with an isotropic material using the conventional SIMP method, and 2) the single-piece topology and continuous orientation optimization using [105]. For the single-piece topology optimization with an isotropic material, the equivalent material

property of randomly orientated discontinuous short fibers were used per [108]:

$$\begin{aligned}\tilde{E} &= \frac{3}{8}E_1 + \frac{5}{8}E_2 \\ \tilde{G} &= \frac{1}{8}E_1 + \frac{1}{4}E_2\end{aligned}\tag{4.19}$$

The nonlinear constrained optimization problem in Equation (4.14) was solved by the method of moving asymptotes [109] with the first derivatives of the objective and constraints. The sensitivity analysis followed the standard adjoint method, and was implemented using COMSOL Multiphysics. Interested readers are referred to [110] for the sensitivity analysis using this software.

The continuation method was applied to the two penalty parameters P_d and P_m and the anisotropy constraint parameter δ in Equation (4.14), based on a fixed continuation and convergence strategy. The density penalty P_d was initialized as 1.5, and updated to 2, 2.5, and 3 at iteration 60, 90, and 120 respectively. The membership penalty P_m was initialized as 1, and updated to 1.5, 2, 2.5, and 3 at iteration 60, 90, 120, and 150 respectively. The anisotropy constraint parameter δ was initialized as 1, and updated to 0.2, 0.1, and 0.02 at iteration 60, 90, and 120 respectively. The maximum number of iterations was set to 200. An alternative strategy for continuation and convergence can also be implemented based on relative measures, e.g., the maximum change in design variables and the first order optimality.

The initial density and component membership were uniformly set to $\rho = V^*$ and $m^{(k)} = 1/K$, respectively. The initial angle $\theta^{(k)}$ for each component k was set to:

$$\theta^{(k)} = \begin{cases} 0^\circ & \text{if } k = 1 \\ (k-1)(180/K)^\circ & \text{otherwise} \end{cases},\tag{4.20}$$

where the norm of orientation Cartesian components $\left\| \vartheta^{(k)} \right\|$ was initialized below 0.3, indicating weak initial anisotropy.

4.7.1 Single load: cantilever

The proposed method is first applied to a single load cantilever problem. Its design domain D and boundary conditions are presented in Figure 4.6. The left side of the cantilever is fixed in all degrees of freedom. A unit load is applied at the lower right corner.

A square grid mesh with a side length of 0.02 is used to discretize the design domain D using the Lagrange linear quadrilateral elements. The upper bound for

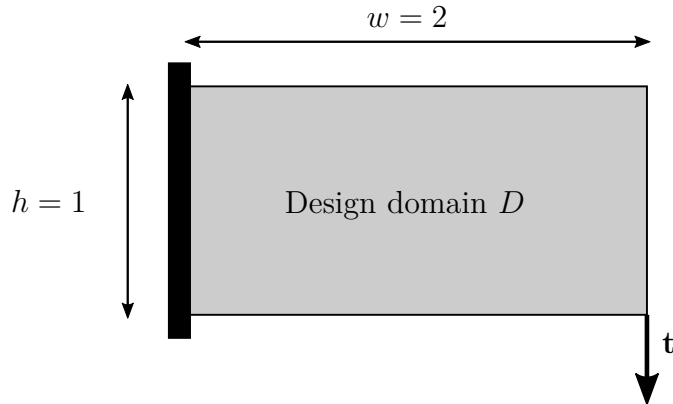


Figure 4.6: Design domain and boundary conditions for the single load cantilever problem.

the material volume fraction V^* is set as 0.5. The maximum allowable number of components is set as $K = 3$.

4.7.1.1 Iterative details

Figure 4.7 shows intermediate multi-component topologies at different iterations during the course of optimization. For each iteration, from left to right, the density field ρ , membership field $m^{(k)}$, component field (product of the two) $\rho m^{(k)}$, and material orientation field $\vartheta^{(k)}$ are shown. The filter radius R_ϑ in Equation (4.5) is set to a large enough value so the $\vartheta^{(k)}$ can become unidirectional within each component k . The colors of streamlines in orientation plots indicate the state of material anisotropy levels $\|\vartheta^{(k)}\|$ based on a color map whose scale is shown in the bottom.

As discussed earlier, the optimization was initialized with uniform density and membership distributions. The material anisotropy levels were initialized as very weak, as seen in Figure 4.7(a). The component partitioning started happening when the overall topology was not yet clear (Figure 4.7(b)), and finally converged at iteration 200 (Figure 4.7(d)). Both the angular values and anisotropy levels of the optimized orientations are different from their initializations.

To demonstrate the effectiveness of the proposed cube-to-simplex projection and penalization method, in Figure 4.8 (from left to right), the component membership field in the cube domain $\bar{\mu}^{(k)}$, in the projected simplex domain $m^{(k)}$, and in the penalized domain $\rho^{P_d}(m^{(k)})^{P_m}$ are visualized at different iterations during the optimization. With the cube-to-simplex projection and penalization method, undesired vertices in the original cube domain that do not satisfy the membership unity constraint have been eliminated. With the continuation on the penalization parameter

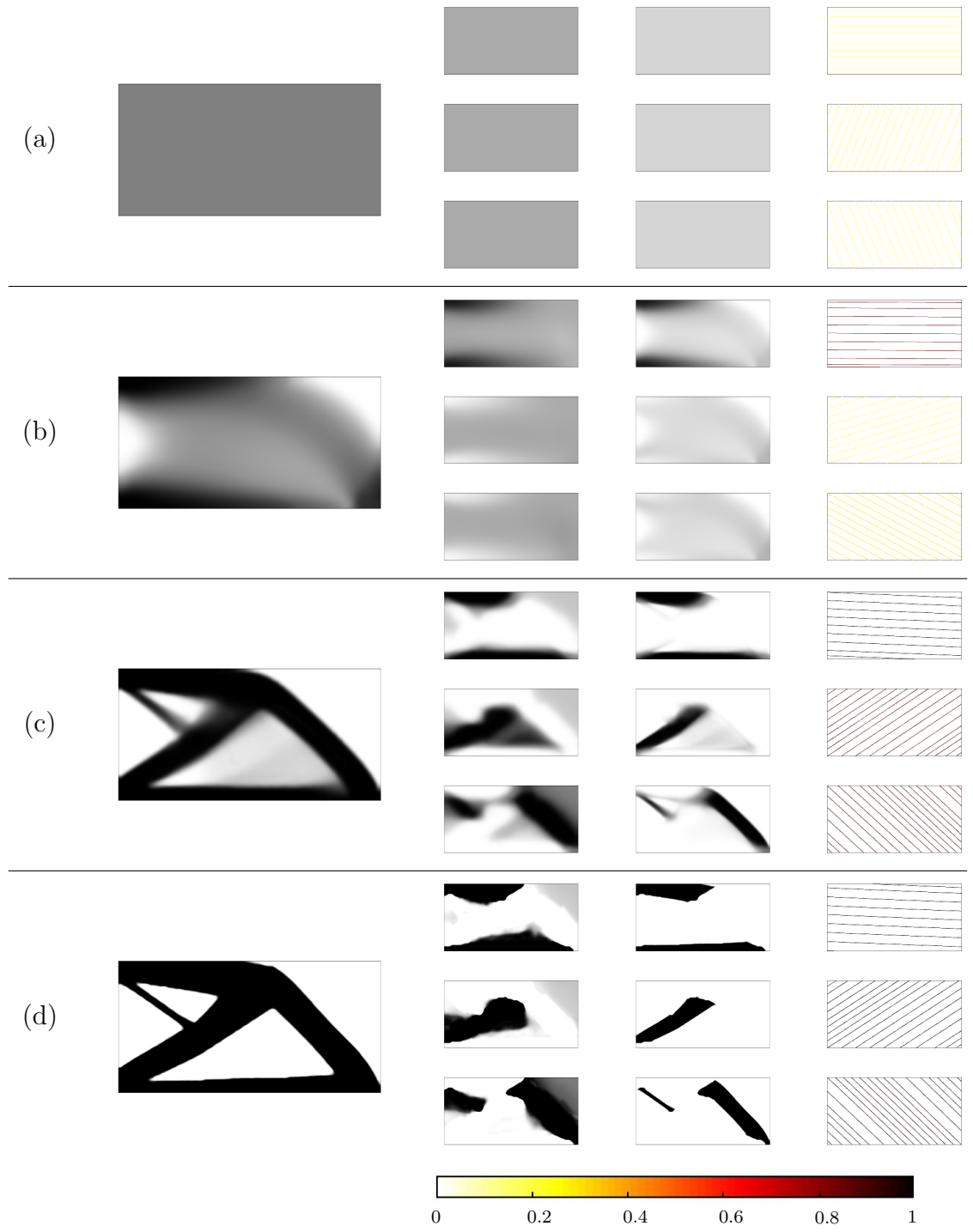


Figure 4.7: Iterative details of all design fields for the single load cantilever problem with $K = 3$ at (a) iteration 1; (b) iteration 5; (c) iteration 50; and (d) iteration 200.

P_m , the component membership field gradually converged to the three vertices with unique membership selections. The component partitioning at the end of optimization at iteration 200 in Figure 4.7(d) shows that a unique selection of memberships for each non-void design point is successfully achieved with the proposed cube-to-simplex projection and penalization method.

The resulting multi-component topology and its component-wise unidirectional orientations are plotted in Figure 4.9, by visualizing different components with colors. It is clearly seen that the resulting material orientations mostly align the longitudinal directions of beam-like substructures. This supports an empirical knowledge that the optimal material orientation should coincide with the major principal stress direction for compliance minimization problems. The resulting optimized structural compliance is 6.21. While desirable for economical production in large quantities, multi-component structures with component-wise unidirectional orientations like this cannot be obtained by existing continuous orientation methods or discrete orientation methods.

It is noticed that the isolated pieces can appear within one component phase k , which is the case for the green pieces in Figure 4.9. It is not an issue for MTO-C because there is no manufacturing constraint applied to each individual component. The resulting isolated pieces within one component phase will simply have the identical unidirectional material orientation. Such phenomenon is also naturally discouraged in the previous chapter for MTO-S and the later chapter for additive manufacturing because of the component size constraint. However, the explicit control of one single connected piece in each component phase can be critical for other applications. It is not explicitly considered in this dissertation, and therefore left for future research.

The convergence history of the optimization process is plotted in Figure 4.10. As seen in Figure 4.10(a), the local fluctuation of the compliance (objective function) was mainly caused by the continuation of the penalization parameters. Otherwise, it was almost monotonically decreasing. As seen in Figure 4.10(b), the volume constraint remained active throughout the optimization. As seen in Figure 4.10(c), the membership field also satisfied the unity constraints, because the unity measure $\int_D \rho \|\mathbf{m}\| d\Omega / A_d$ converged approximately to 1 at the end of optimization. As a result of the adopted penalization scheme, the membership unity measure was not necessary as an additional constraint in the optimization problem. It was plotted here just for the monitoring purpose. As seen in Figure 4.10(d), the material anisotropy constraints for all components were active at the end of optimization as well.

As a comparison, the optimized single-piece topology with an isotropic material

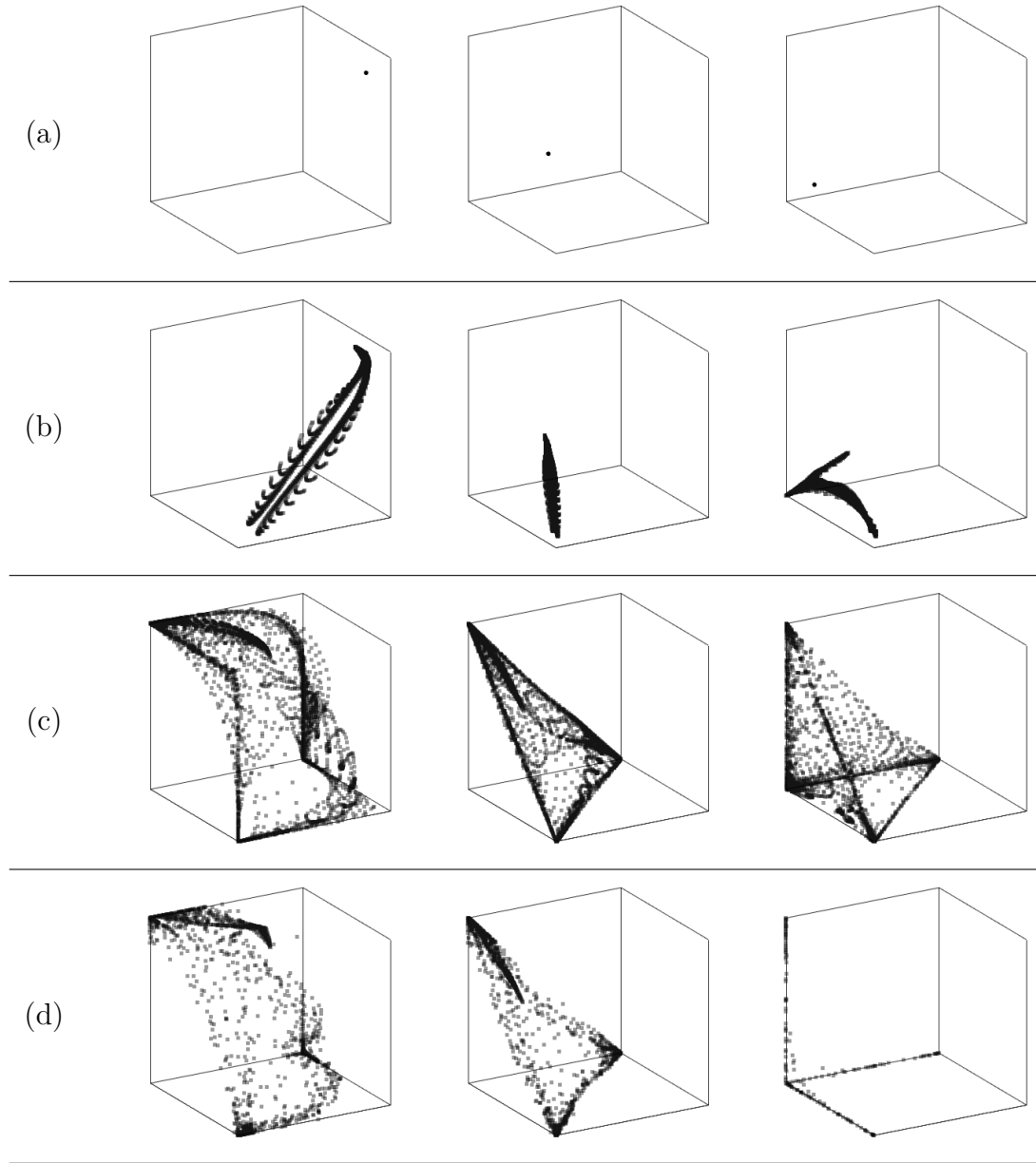


Figure 4.8: Iterative details for the convergence of the component membership field at (a) iteration 1; (b) iteration 5; (c) iteration 50; and (d) iteration 200.

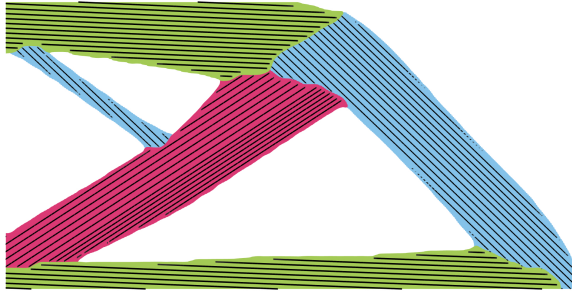


Figure 4.9: The optimized three-component topology with component-wise unidirectional orientations. Its optimized structural compliance is 6.21.

is presented in Figure 4.11(a) following the assumption of randomly oriented discontinuous short fibers in Equation (4.19). Its optimized structural compliance is 9.92, inferior to the anisotropic multi-component design. In addition, the optimized single-piece topology with the continuous orientation design is presented in Figure 4.11(b) following the method proposed in [105]. As expected, the resulting compliance is 4.07, which is superior than both cases discussed above.

4.7.1.2 Curvilinear fiber orientation

One way to further improve the performance of multi-component composite structures is to allow curvilinear fiber orientations within each component instead of enforcing unidirectional fiber orientations. By reducing the filter radius on the orientation vector field, one can control the maximum allowable curvature of the fiber orientation within each component. Figure 4.12(a) presents the optimized three-component topology design allowing a moderate level of curvature on fiber orientations. The structural compliance is improved to 5.65, as opposed to 6.21 in the three-component unidirectional case. Its design fields at the end of optimization are visualized in Figure 4.12(b-c).

It is noted that the overall base topology is different from that of the unidirectional case. This is due to the interaction between the density and membership fields with the additional freedom on orientation tailoring. It should also be noted that by allowing curvilinear orientations in composite structures, it is likely that more advanced composite processing techniques are required, which will come with a higher production cost than composite manufacturing processes with unidirectional prepreg preforms.

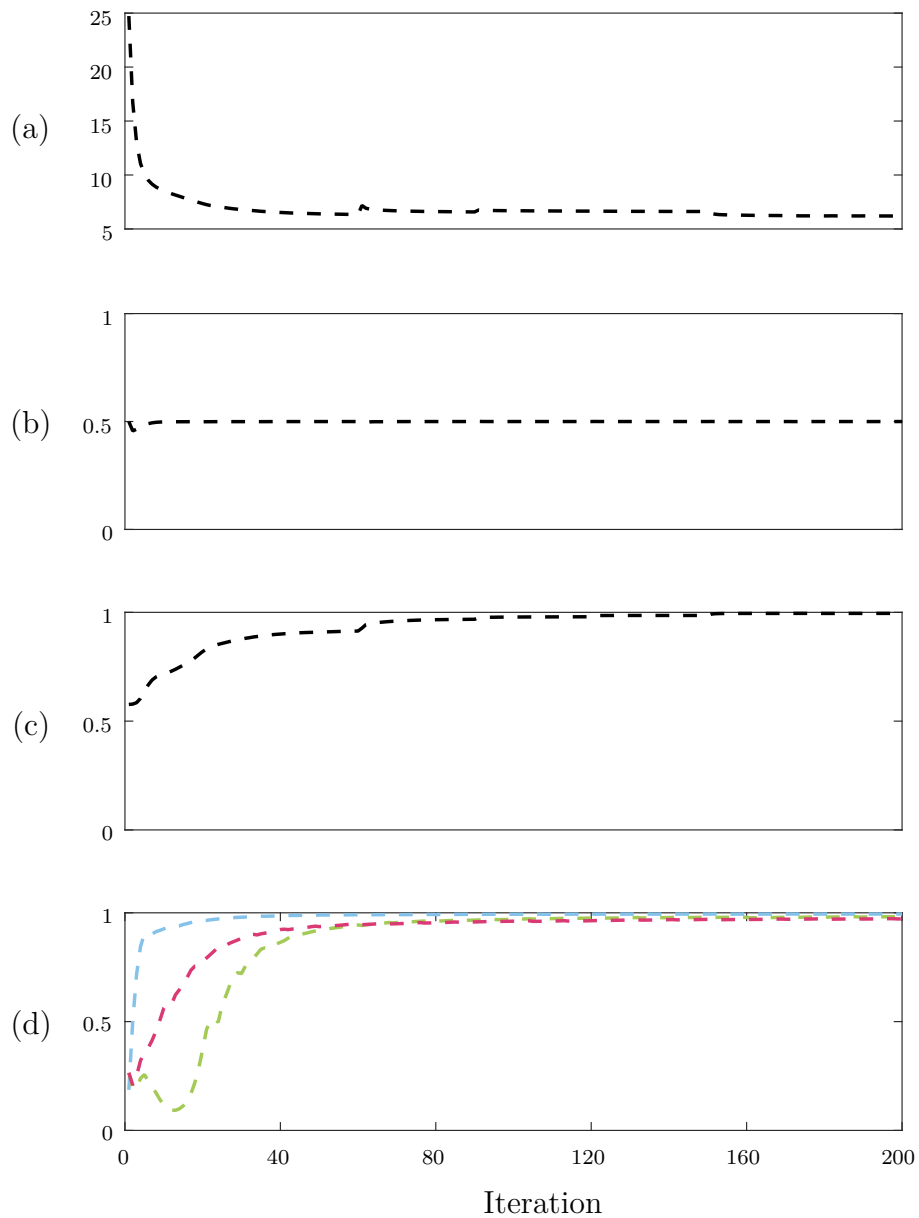


Figure 4.10: Convergence history for the single load cantilever problem with $K = 3$. (a) Compliance (objective function); (b) volume constraint; (c) membership unity measure; (d) material anisotropy constraints. (The membership unity measure is plotted for the monitoring purpose, which is not included as a constraint in the optimization.)

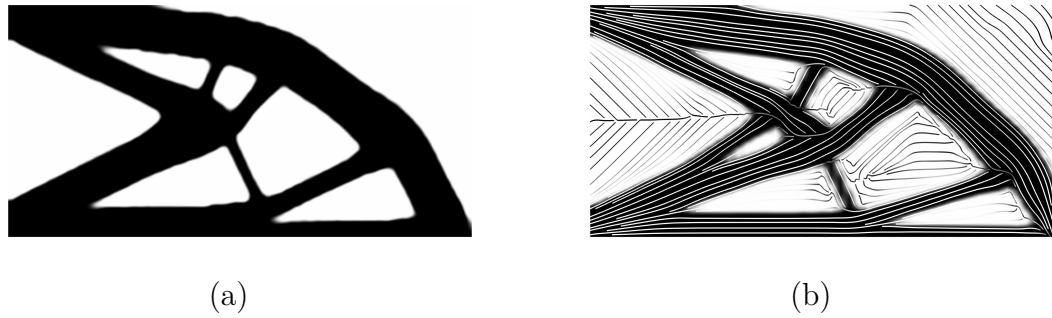


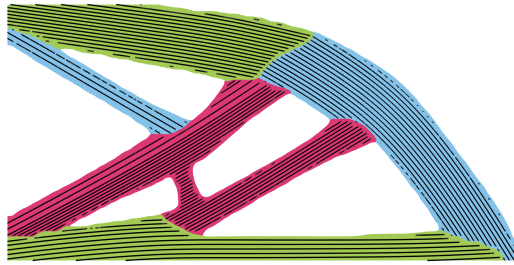
Figure 4.11: (a) Optimized single-piece topology with an isotropic material. Its optimized structural compliance is 9.92; (b) optimized single-piece topology with continuous material orientation. Its optimized structural compliance is 4.07.

4.7.1.3 Different number of components

The maximum allowable number of components K (i.e., the maximum allowable number of discrete orientations), is an input to the optimization. This section discusses the effect of setting different values of K on the optimization results.

Figure 4.13 shows the optimized multi-component topologies with K equals to 1 to 4. The case of $K = 3$ has been previously presented in Figure 4.9. The structural compliance improves as the maximum allowable number of discrete orientations increases. Their optimized compliance values are 9.92, 6.76, 6.21, and 5.83 for $K = 1$, $K = 2$, $K = 3$, and $K = 4$ respectively. Similar to the curvilinear study, the overall base topology adapts to different settings of K . It is not surprising to see that with the increase of K , the base topology becomes rather similar to that of the optimized single-piece topology with an isotropic material in Figure 4.11(a). The similar observation that the base topologies for the anisotropic and isotropic designs are almost identical for single load compliance minimization problems, was also reported in [105]. From the economical perspective, the fewer number of orientations will usually lead to less production cost in large quantities due to the reduced customization of unidirectional fiber fabrics, and the reduced labor cost on manual prepreg preform layups.

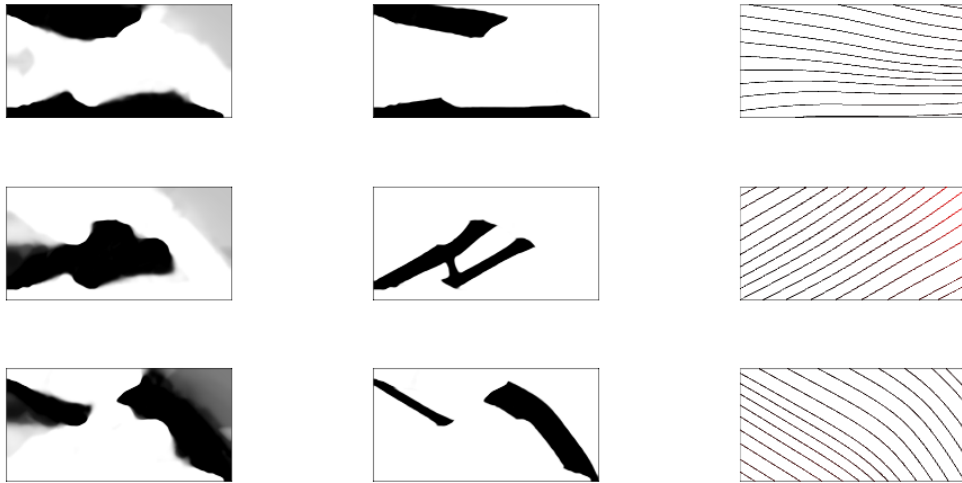
In summary, Table 4.2 compares the optimized structural performances for all numerical examples discussed in Section 4.7.1. The optimized single-piece topology with an isotropic material, assuming randomly oriented discontinuous short fibers, yields the worst structural performance. The optimized single-piece topology with the continuous material orientation based on [105] yields the best structural perfor-



(a)



(b)



(c)

Figure 4.12: The optimized three-component design allowing component-wise curvilinear orientations. Its optimized structural compliance is 5.65. (a) The optimized multi-component topology; (b) the optimized density field ρ ; (c) from left to right: the optimized membership field $m^{(k)}$, the optimized component field (product of the two) $\rho m^{(k)}$, and the optimized material orientation field $v^{(k)}$.

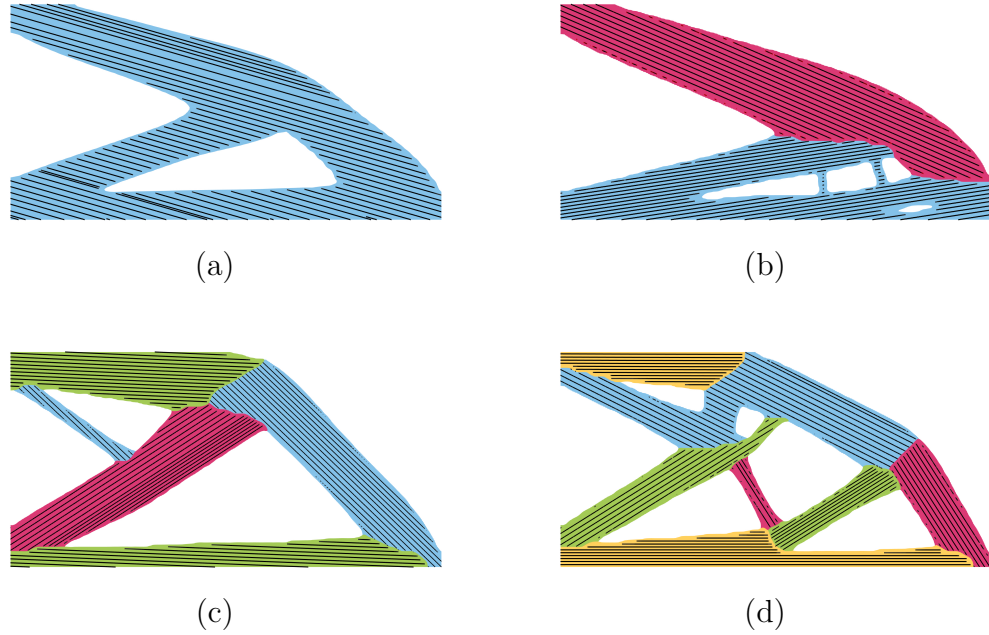


Figure 4.13: The optimized multi-component topologies with different number of components K settings. (a) $K = 1$; (b) $K = 2$; (c) $K = 3$; (d) $K = 4$.

Table 4.2: Summary of the structural performance and estimated mass-production cost of cantilever designs discussed in Section 4.7.1.

	Iso-tropic	MTO unidirectional				MTO curv	Con-tinuous
		$K = 1$	$K = 2$	$K = 3$	$K = 4$		
Compliance	9.92	9.27	6.75	6.21	5.83	5.65	4.07
Cost	low	med	med	med	med	med+	high

mance, followed by the optimized multi-component topology with curvilinear material orientations, and then the optimized multi-component topologies with different numbers of unidirectional material orientations. Though their production costs are not quantitatively modeled, the qualitative estimations are also listed in Table 4.2, which illustrate the trade-off between structural performance and mass production cost.

4.7.2 Multi-load: tandem bicycle frame

To demonstrate the applicability of the proposed method to more realistic anisotropic structural design problems, this section presents the design of a tandem bicycle frame. Regular bicycle frame examples have been found in the past literature on topology optimization [111, 112, 113]. It has served as a good academic example mainly because

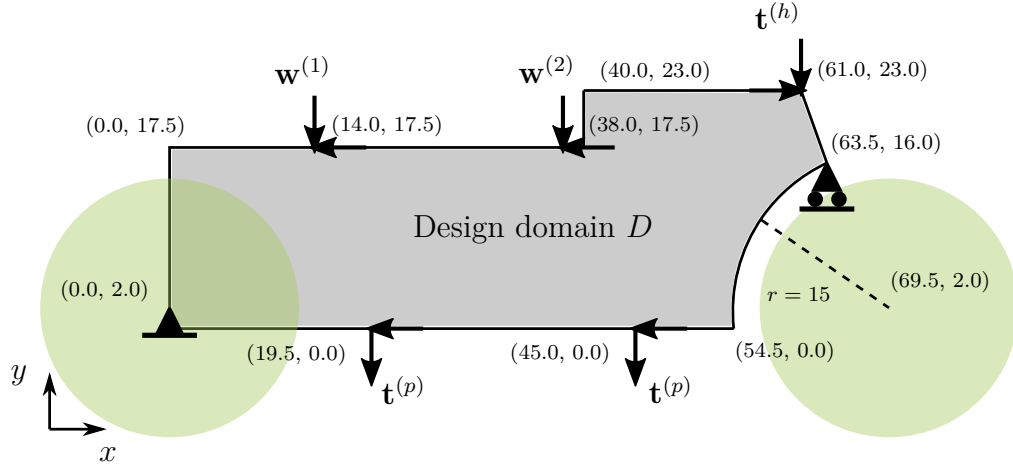


Figure 4.14: Design domain and boundary conditions for the multi-load tandem bicycle frame example, where $t_x^{(p)} = -1.5$; $t_y^{(p)} = -1.0$; $t_x^{(h)} = 1.0$; $t_y^{(h)} = -1.0$; $w_x = \{-1.0, -0.25\}$; and $w_y = \{-6.0, -1.5\}$. At location $(0.0, 2.0)$, both degrees of freedom in x and y are fixed. At location $(63.5, 16.0)$, only the degree of freedom in y is fixed. The lower left corner of the design domain is set as location $(0.0, 0.0)$.

1) it has an intuitive structure that everyone is familiar with; 2) it is a simplified 2D problem with only in-plane loading conditions; and 3) it has an irregularly-shaped design domain that requires irregular meshing, which adds some complexity to other examples with a rectangular domain. In addition to these properties, the design of a tandem bicycle frame is inherently a multi-load problem depending on whether the heavier rider is sitting in the front or in the rear, which is very suitable for testing anisotropic topology optimization.

Figure 4.14 shows the design domain and boundary conditions of a simplified tandem bicycle frame example. The design domain is discretized with 11052 free irregular quadrilateral elements. The example assumes that an adult and a child will be riding the bicycle. Depending on who is sitting in the front, there are two loading conditions. Each load is applied and solved independently. The objective for the multi-load problem is formulated as follows:

$$F_m = F_1 + F_2, \quad (4.21)$$

where F_m is the multi-load objective function; F_1 and F_2 are structural compliances for the two loading conditions.

Figure 4.15(a) presents the benchmark isotropic single-piece topology design assuming randomly oriented discontinuous short fibers with a resulting compliance value of 4952. Its deformation plots for the two loading conditions are also presented in

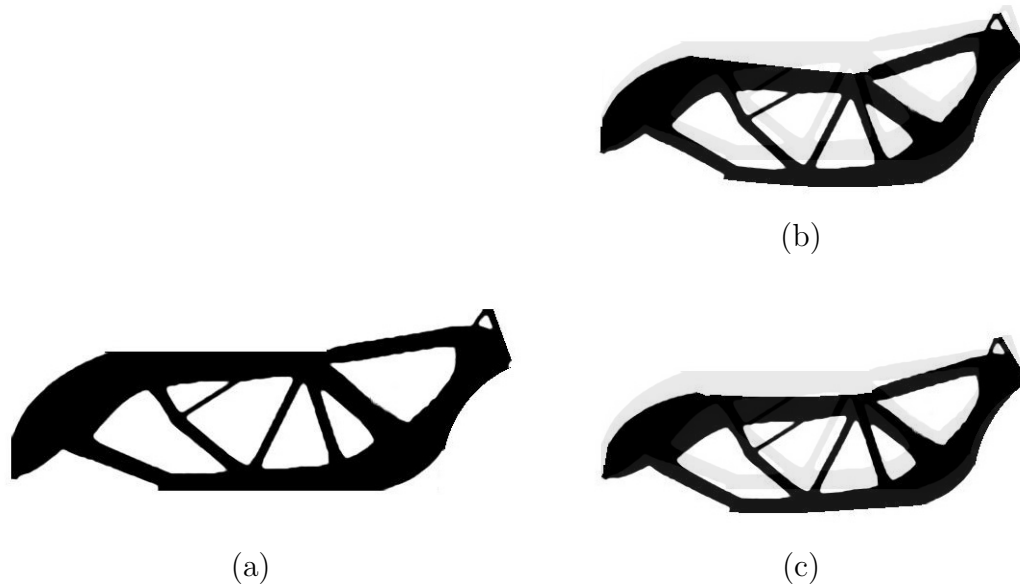


Figure 4.15: (a) The optimized single-piece tandem bicycle frame structure with an isotropic material; (b) the deformed structure under the heavy front loading condition; (c) the deformed structure under the heavy rear loading condition. Its optimized multi-load structural compliance is 4952.

Figure 4.15(b–c). Figure 4.16(a) presents the optimized multi-component topology with the material orientation design. Its design fields at the end of optimization are presented in Figure 4.16(b–c). For the anisotropic multi-component topology design, K is set as 3, and the unidirectional fiber orientation is enforced for each component by setting the orientation filter radius larger than the size of the design domain. As we have seen in previous results, the overall base topology is different from that of the isotropic case. The optimized unidirectional fiber orientations mostly align the longitudinal directions of beam-like substructures. The optimized multi-load compliance for the multi-component case is 3312, which is more than 30% improvement over the benchmark isotropic design.

4.8 Chapter summary

This chapter proposed a topology optimization method for structures made of multiple composite components (substructures) with tailored material orientations. The method was capable of simultaneously optimizing the overall topology, component partitioning, and unidirectional (or curvilinear) material orientation for each compo-

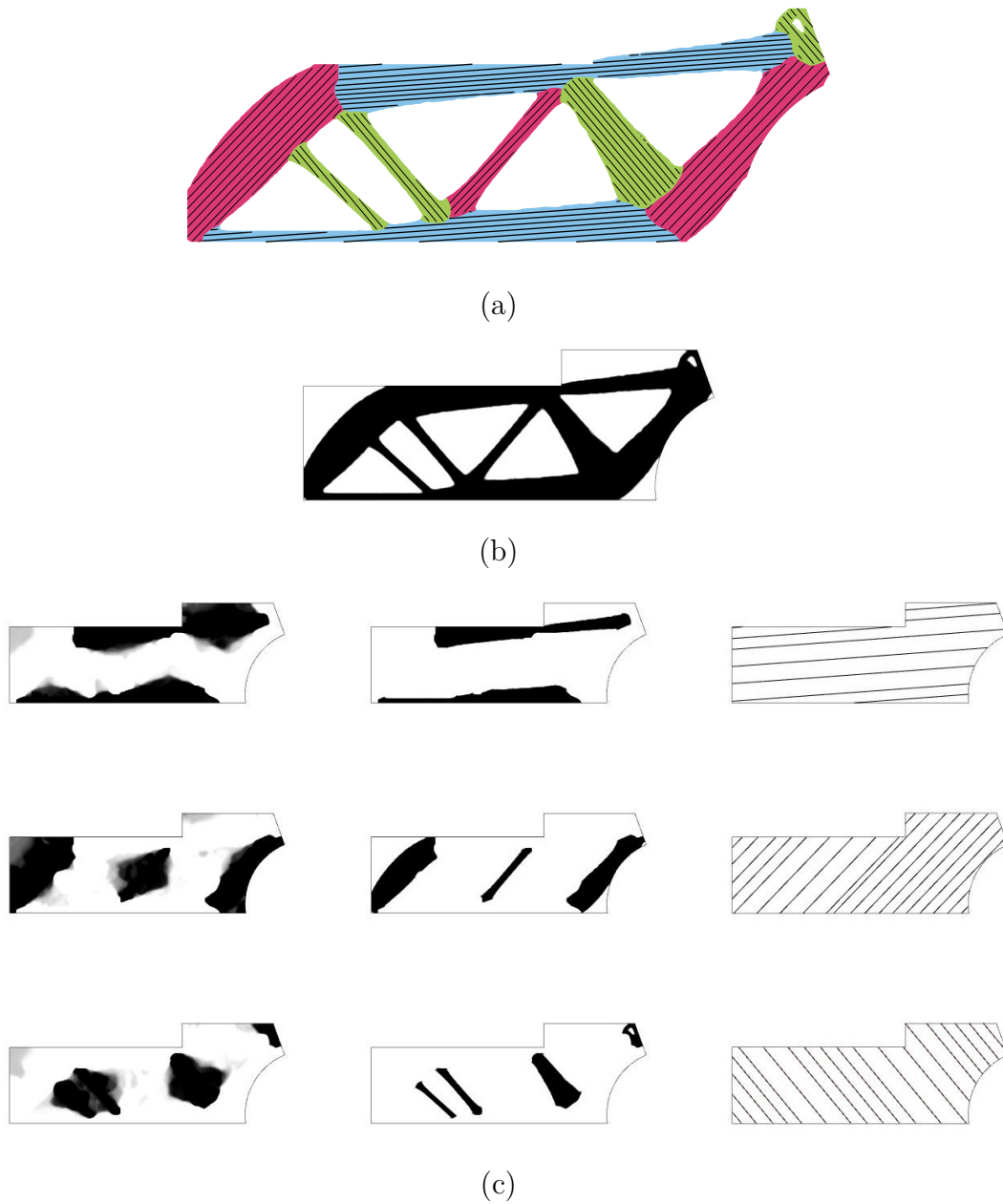


Figure 4.16: The optimized multi-component tandem bicycle frame structure with component-wise unidirectional material orientations. Its optimized multi-load structural compliance is 3312. (a) The optimized multi-component topology; (b) the optimized density field ρ ; (c) from left to right: the optimized membership field $m^{(k)}$, the optimized component field (product of the two) $\rho m^{(k)}$, and the orientation field $\vartheta^{(k)}$.

ment. In addition to the density and membership design fields in the general MTO formulation as discussed in Chapter 2, an orientation vector field was introduced to design the anisotropic material orientations. The proposed method was capable of generating multi-component composite structures with tailored material orientations for each component, without a prescribed set of alternative discrete angles. The outcome was a unique composite structural design solution that could not be accomplished by either existing continuous or discrete material orientation methods, and would be most suitable for economical composite manufacturing processes.

The proposed method was applied to several numerical examples with much higher resolution than previously reported. This was mainly due to the proposed cube-to-simplex projection and penalization method that eliminated the many equality constraints.

The results were compared to the designs optimized by a conventional, single-piece isotropic topology optimization method and a continuous orientation method. The comparison revealed that the proposed method produced unique multi-component topology designs with component-wise unidirectional material orientations. The proposed method consistently generated designs with better structural performance than single-piece, isotropic designs. Though the multi-component designs sacrifice on structural compliance compared to the single-piece designs with continuous material orientation, they demonstrated potentially large cost savings in mass production via economical composite manufacturing processes, which require a unidirectional orientation for each component. By allowing the curvilinear orientation in each component, the structural performance of the multi-component designs could be improved, at an expense of less economical, advanced composite manufacturing processes.

The interface between different components in this chapter was assumed perfectly bonded without structural performance degradation. In practice, the component interface location will often have overlapped composite fabrics. Such behavior was not modeled in this chapter.

CHAPTER 5

Multi-component topology optimization for additive manufacturing

This chapter presents the MTO application to structures assembled from components built by powder bed additive manufacturing, termed the Multi-component Topology Optimization for Additive manufacturing (MTO-A). Additive manufacturing is a class of manufacturing processes that build structures by adding layer-upon-layer of materials. It is capable of producing structures with “almost” any shapes, which can be difficult, if not impossible, for traditional manufacturing processes, e.g., machining and stamping. Additive manufacturing shares with topology optimization with a similar trait that facilitates innovative designs through the relaxation of constraints on component geometries. Topology optimization therefore has become a promising tool for designing additive manufacturing products (e.g., [114, 115, 116, 57, 117].)

Additive manufacturing can be categorized into two major classes, the powder bed process (e.g., selective laser sintering, direct metal melting) and the wire-fed process (e.g., fused deposition modeling, electrohydrodynamic jet). Though this chapter limits its scope in the former, most discussions are commonly applicable for both classes.

5.1 Why multiple components for powder bed additively manufactured structures

Although powder bed additive manufacturing is vastly more flexible than traditional processes in terms of what shapes can be made, there are still some restrictions as discussed below.

A component cannot be made if it physically exceeds the printer’s maximum allowable build volume. The build volume is defined as the maximum size (in length,

width and height) of an object that an additive manufacturing machine can produce. For powder bed processes, the build volume restriction is rather significant due to their strict powder bed size limits. This restriction has limited their applications to produce relatively small parts.

Complete hollow features should be avoided during part design. Because the unmelted powders trapped inside of any enclosed holes cannot be removed from the component once it has been built.

The minimum feature size should be explicitly controlled. This size is determined by the minimum printable feature size based on the machine specification.

If structures are designed in the multi-component manner, the design freedom dramatically increases due to the new interpretations of manufacturing restrictions. For example, a structure exceeding the maximum build volume, which cannot be made as a single piece, can now be produced as an assembly of multiple components. A multi-component structures with “global” hollow features can now be manufactured as well, as long as each component has no “local” enclosed holes therein. These new interpretations of manufacturing restrictions unlock the possibility of designing structures with more complex geometry and better performance, taking full advantage of the benefit of additive manufacturing and topology optimization. These benefits associated with the multi-component structures assembled from additively-manufactured components are discussed in a recent Formlab tutorial on “how to build bigger than the printer’s build volume” [118]. In the tutorial, however, the component partitioning is treated as an arbitrary manual decision after the overall structural design is complete, not as an outcome of a system-level optimization. The MTO-A method proposed in this chapter intends to realize the simultaneous optimization of base topology and component decomposition for structures assembled from additively-manufactured components.

5.2 Design field configuration

The design field configuration of MTO-A follows that of the general MTO, as discussed in Chapter 2. There are two layers, including the density field ρ and membership vector field $\mathbf{m} = (m^{(1)}, m^{(2)}, \dots, m^{(K)})$, where K is the maximum allowable number of components. As discussed in Chapter 4, the regularization of ρ and $m^{(k)}$ follows the framework detailed in [38], which includes the Helmholtz PDE filtering and Heaviside projection.

For details of the topology design representation, readers are referred to Section 4.3.1 of this dissertation. The resulting regularized density field ρ is bounded between 0 and 1.

The membership design representation follows the regularization scheme discussed in Section 4.3.3. However, to ensure the membership unity, instead of using the cube-to-simplex projection method proposed in Chapter 4, a different nonlinear projection method, the DMO method [62], is used in this chapter. DMO has been widely used in multi-material topology optimization studies. As discussed in Section 1.2.3, from a viewpoint of mathematical formulation, MTO is closely related to multi-material topology optimization. The successful use of a widely accepted multi-material topology optimization method to the MTO problem somewhat proved that argument.

As detailed in Section 4.3.3, after the original membership field $\mu^{(k)}$ is transformed to $\tilde{\mu}^{(k)}$ and $\bar{\mu}^{(k)}$, the resulting $\bar{\mu}^{(k)}$ preserves a clear bound between 0 and 1. The DMO projection is then applied to the regularized membership field $\bar{\mu}^{(k)}$ as follows:

$$m^{(k)} = \{\bar{\mu}^{(k)}\}^{P_m} \prod_{\substack{i=1 \\ i \neq k}}^K \left[1 - \{\bar{\mu}^{(i)}\}^{P_m} \right], \quad (5.1)$$

where P_m is a penalization parameter similar to the SIMP power law. The DMO projection method is effective in driving the membership convergence to 0 or 1, because an increase in the membership to one component always leads to a decrease in the membership of all other components. It also encourages that the membership to only one component converges to 1 while the memberships to all other components converge to 0. It is noted that the cube-to-simplex projection method discussed in Chapter 4 serves a similar purpose.

5.3 Manufacturing constraint modeling for powder bed additive manufacturing

This section discusses the modeling of two manufacturing constraints for powder bed additive manufacturing, including the maximum build volume and the elimination of enclosed holes. Both constraints are applied at the component level.

5.3.1 Maximum allowable build volume

The build volume of a powder bed additive manufacturing machine is usually given as a specification, defined by its maximum allowable length, width, and height. A designed part can only be produced if it physically fits inside the bounding box defined by these dimensions. There has been no previous work discussing constraining the additive manufacturing part size for topology optimization. It is, mainly, due to the fact that most existing topology optimization works assume the optimized structure will be produced as a single-piece, which has already been naturally bounded by its initial design domain. Therefore, there is no need for the build volume constraint. However, this is not the case for MTO, where the initial design domain bounding box is defined for the overall structure but not for the individual component. In the computer graphics community, there are recent works discussing partitioning 3D printable parts based on a specified maximum build volume limit (e.g., [119, 120]). However, these works only dealt with partitioning of given geometries. Also, the partitioning was treated as discrete problems, and generally solved by heuristic optimization methods.

Different from the stamping die-set material cost constraint discussed in Section 3.5.1, where the overall size of bounding boxes should be minimized, the build volume constraint needs to explicitly control the length, width, and height of each bounding box. Following the stamping die-set material cost constraint, OBB is used again to determine the component bounding box. However, an improved mesh-independent formulation is presented in this chapter.

As demonstrated in Figure 5.1, each design point in the design domain D is associated with K weights $w^{(k)} = \rho m^{(k)}$. \mathbf{x} is the centroid position of a design point. The weighted covariance matrix $\Sigma^{(k)}$ for each component k can be written as:

$$\Sigma^{(k)} = \frac{1}{A_w^{(k)}} \int_D \rho m^{(k)} \mathbf{x} \mathbf{x}^\top d\Omega, \quad (5.2)$$

where \mathbf{x} is assumed written as a column vector, and $A_w^{(k)} = \int_D \rho m^{(k)} d\Omega$. By applying the singular value decomposition to $\Sigma^{(k)}$, orthogonal principal components can be extracted. They will be used to determine the length, width and height directions (= the orientation of OBB), which are denoted as $\mathbf{u}_1^{(k)}$, $\mathbf{u}_2^{(k)}$, and $\mathbf{u}_3^{(k)}$ respectively.

For each component k , all design points \mathbf{x} are then projected to each principal direction. The approximate center of component k in the $\mathbf{u}_j^{(k)}$ direction can be com-

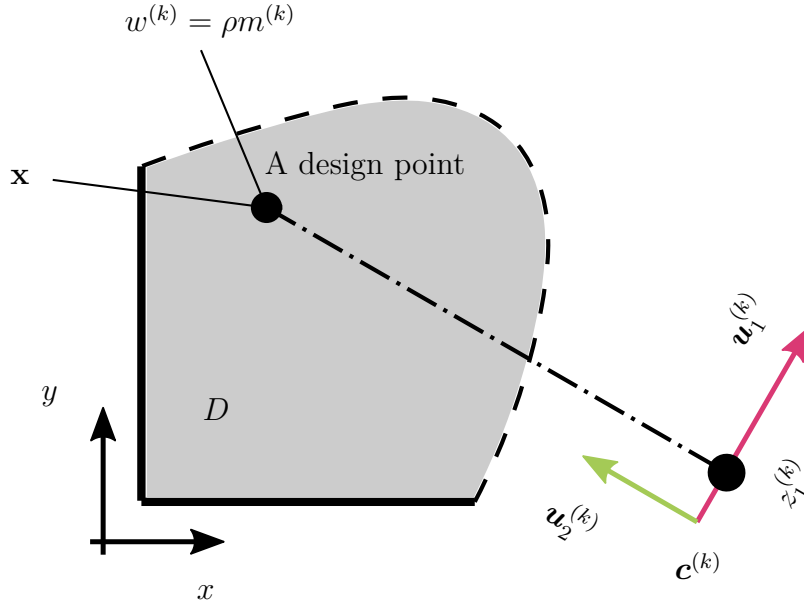


Figure 5.1: Computation of the bounding box. This is a mesh-independent formulation. (The mesh-dependent formulation was presented in Figure 3.4.)

puted as the weighted mean of all projected values:

$$c_j^{(k)} = \frac{1}{A_w^{(k)}} \int_D \rho m^{(k)} z_j^{(k)} d\Omega, \quad (5.3)$$

where $z_j^{(k)} = \mathbf{u}_j^{(k)\top} \mathbf{x}$ is the projection of \mathbf{x} on the $\mathbf{u}_j^{(k)}$ direction. The weighted squared distance between every projection and the center can be computed as:

$$d_j^{(k)} = \rho m^{(k)} \left\{ z_j^{(k)} - c_j^{(k)} \right\}^2. \quad (5.4)$$

Finally, the printer build volume constraint to bound the maximum allowable length, width and height of each component k is defined as:

$$\begin{aligned} l^{(k)} &= \max_{\mathbf{x} \in D} d_1^{(k)}(\mathbf{x}) \leq L^* \\ w^{(k)} &= \max_{\mathbf{x} \in D} d_2^{(k)}(\mathbf{x}) \leq W^*, \\ h^{(k)} &= \max_{\mathbf{x} \in D} d_3^{(k)}(\mathbf{x}) \leq H^* \end{aligned} \quad (5.5)$$

where L^* , W^* , and H^* are the squared halves of the length, width, and height limits,

respectively, imposed by the powder bed additive manufacturing machine specification.

To maintain the constraint differentiability for use with gradient-based optimization, the maximum operator in Equation (5.5) is approximated by the P-norm function as follows:

$$\max_{\mathbf{x} \in D} d_j^{(k)}(\mathbf{x}) \approx C_f \left[\frac{1}{A_0} \int_D \left\{ d_j^{(k)}(\mathbf{x}) \right\}^{P_n} d\Omega \right]^{1/P_n}, \quad (5.6)$$

where $A_0 = \int_D d\Omega$, and P_n is a numerical tuning parameter. A moderate value for P_n needs to be set to balance the numerical approximation accuracy and the function smoothness. Due to the discrepancy between the P-norm value and the “true” maximum value, an adaptive correction factor C_f is introduced, which is the ratio between the “true” maximum value and the P-norm value from the previous iteration. Similar correction strategy for the P-norm approximation was previously reported in [121].

5.3.2 Elimination of enclosed holes

For conventional, single-piece topology optimization, the virtual temperature method has been proposed to generate simply-connected topologies by constraining the maximum steady-state temperature of a fictitious thermal analysis [55, 56]. However, when enclosed holes are not allowed in a single-piece structure, the use of topology optimization becomes somewhat questionable, since the advantage of topology optimization over the sizing and shape optimization is its capability for adding (and removing) holes and exploring shapes with different connectivity. Designers may rather just use the sizing or shape optimization in order to design parts without holes.

To eliminate holes enclosed within each component, the virtual temperature method is generalized, to make it applicable to MTO. Instead of prohibiting enclosed holes in the entire single-piece structure, the generalized constraint only prevents hole formation within each component. A linear finite element analysis on fictitious heat conduction is conducted for each component at each optimization iteration. By bounding the steady-state maximum temperature in a component, the formation of holes enclosed within a component is indirectly discouraged during the course of optimization.

For each component k , the Neumann boundary condition of a constant (fictitious) heat flux is applied to every design point depending on its density field ρ :

$$Q = (1 - \rho) Q_0, \quad (5.7)$$

where Q_0 is the maximum heat flux that can be applied if the material density equals to zero. The Dirichlet boundary condition of zero temperature is applied to all boundaries of the initial design domain D .

The (fictitious) coefficient of thermal conductivity for each design point of component k is defined as:

$$K^{(k)} = \left(1 - \rho m^{(k)}\right)^{P_k} K_0, \quad (5.8)$$

where P_k is a penalization parameter similar to the SIMP power law, and K_0 is the maximum thermal conductivity that can be applied if the material density equals to zero or if the design point does not belong to component k . For each component k , the steady-state temperature field $t^{(k)}$ can be computed by solving the thermal equilibrium equation.

For a converged topology with only 0-or-1 densities and component memberships, for example, the fictitious heat flux Q is applied to only the design points with zero densities (i.e., voids) per Equation (5.7), which can conduct heat to the adjacent point belonging to the same component per Equation (5.8). The design points with density 1 (i.e., solid materials), on the other hand, cannot conduct heat to the adjacent point belonging to the same component, since they are regarded as a thermal insulator per Equation (5.8). As a result, if enclosed holes exist in a component, the heat will not be able to dissipate to the domain boundary, resulting in exponentially higher steady-state temperature compared to components without enclosed holes. Therefore, by constraining the maximum steady-state temperature in temperature field $t^{(k)}$, holes enclosed in component k will be indirectly discouraged during the course of optimization. The constraint for component k can be summarized as follows:

$$t_{max}^{(k)} = \max_{\mathbf{x} \in D} t^{(k)}(\mathbf{x}) \leq T^*, \quad (5.9)$$

where T^* is the constraint limit for the allowable maximum temperature. Similar numerical approximation for the maximum operator as described in Equation (5.6) is used to maintain the smoothness and differentiability of the constraint for use with gradient-based optimization.

5.4 Optimization formulation

The MTO-A problem is formulated as the minimization of structural compliance subject to constraints on the maximum allowable build volume and absence of enclosed holes for each component, as demonstrated in Figure 5.2. A design domain D is

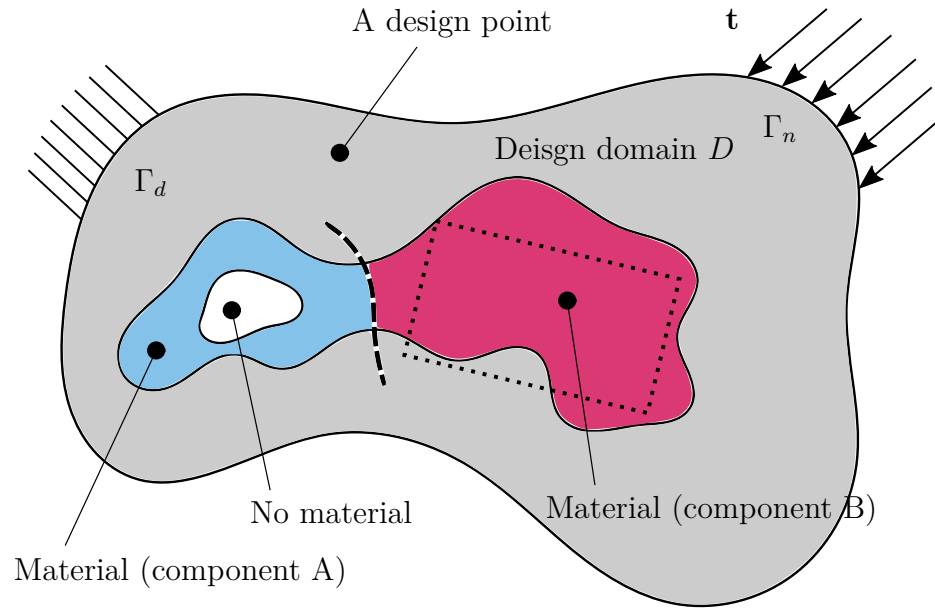


Figure 5.2: Problem description of multi-component topology optimization for powder bed additive manufacturing.

chosen so that loads and boundary conditions can be applied. Then the problem is defined as finding the optimal material distribution and component partitioning simultaneously within D . Suppose that A (in blue) and B (in red) in Figure 5.2 are two components, for instance, this particular partitioning is infeasible, since component A does not satisfy the enclosed hole constraint while component B does not satisfy the build volume constraint (assuming the dot rectangle is the prescribed, maximum allowable build volume).

The overall MTO-A problem can be formulated as follows:

$$\begin{aligned}
& \underset{\phi, \mu^{(1)}, \dots, \mu^{(K)}}{\text{minimize}} && F(\mathbf{u}) \\
& \text{subject to} && g_1 := \int_D \rho \, d\Omega - V^* \leq 0 \\
& && \phi \in [-1, 1]^D \\
& && \text{for } k = 1, 2, \dots, K : \\
& && g_2^{(k)} := l^{(k)} - L^* \leq 0 \\
& && g_3^{(k)} := w^{(k)} - W^* \leq 0 \\
& && g_4^{(k)} := h^{(k)} - H^* \leq 0 \\
& && g_5^{(k)} := t_{max}^{(k)} - T^* \leq 0 \\
& && \mu^{(k)} \in [-1, 1]^D
\end{aligned} \tag{5.10}$$

where \mathbf{u} is the displacement field obtained by solving static equilibrium equations; $F(\mathbf{u})$ is the objective function for a structural performance; K is the prescribed, maximum allowable number of components; g_1 is the volume fraction constraint; $g_2^{(k)}$ through $g_4^{(k)}$ are the maximum allowable build volume constraints for each component; $g_5^{(k)}$ is the constraint to avoid enclosed holes for each component.

In the case of the minimization of structural compliance as discussed in the following examples, the objective function can be stated as:

$$F(\mathbf{u}) = \int_D \frac{1}{2} \boldsymbol{\sigma}^\top \boldsymbol{\epsilon} \, d\Omega, \tag{5.11}$$

and the static equilibrium equations can be written as:

$$\begin{aligned}
\nabla \cdot \boldsymbol{\sigma} &= \mathbf{0} && \text{in } D \\
\mathbf{u} &= \mathbf{0} && \text{on } \Gamma_d, \\
\boldsymbol{\sigma} \cdot \mathbf{n} &= \mathbf{t} && \text{on } \Gamma_n
\end{aligned} \tag{5.12}$$

where $\boldsymbol{\sigma} = \mathbf{C} \cdot \boldsymbol{\epsilon}(\mathbf{u})$ is the stress field; $\boldsymbol{\epsilon}(\mathbf{u})$ is the strain field; \mathbf{C} is the elasticity tensor field; Γ_d is the Dirichlet boundary defined by zero prescribed displacement; and Γ_n is the Neumann boundary defined by the normal \mathbf{n} and the prescribed traction \mathbf{t} .

The elastic tensor is obtained by a material interpolation scheme similar to multi-

Table 5.1: Material properties and parameters for numerical examples.

Symbol	Value	Description
E	1	Young's modulus
ν	0.3	Poisson ratio
Q_0	$2e4$	fictitious heat flux
K_0	$2e3$	fictitious thermal conductivity
T^*	$1e3$	the maximum allowable temperature limit
P_d	3	penalty for the SIMP density power law
P_m	6	penalty for the membership power law
P_k	6	parameter in the thermal conductivity interpolation
P_n	6	parameter in the P-norm approximation

material topology optimization as follows:

$$\mathbf{C} = \rho^{P_d} \sum_{k=1}^K m^{(k)} \mathbf{C}_0, \quad (5.13)$$

where \mathbf{C}_0 is the full elasticity tensor; ρ and $m^{(k)}$ are the regularized material density field and component membership field; P_d is the penalization parameter for the SIMP power law.

5.5 Numerical results

Similar to MTO-C, the constrained optimization problem of MTO-A in Equation (5.10) was solved by the method of moving asymptotes [109] with only the first derivatives. The sensitivity analysis followed the standard adjoint method and was implemented using COMSOL Multiphysics. Interested readers are referred to [110] for the sensitivity analysis using the software.

The design field was uniformly initialized as $\rho = V^*$ and $m^{(k)} = 1/K$. The optimization would terminate when either the lower bound setting on the change of the objective function value or the prescribed, maximum number of iterations was satisfied.

Table 5.1 summarizes material properties and some parameters that are shared among all numerical examples presented in this section.

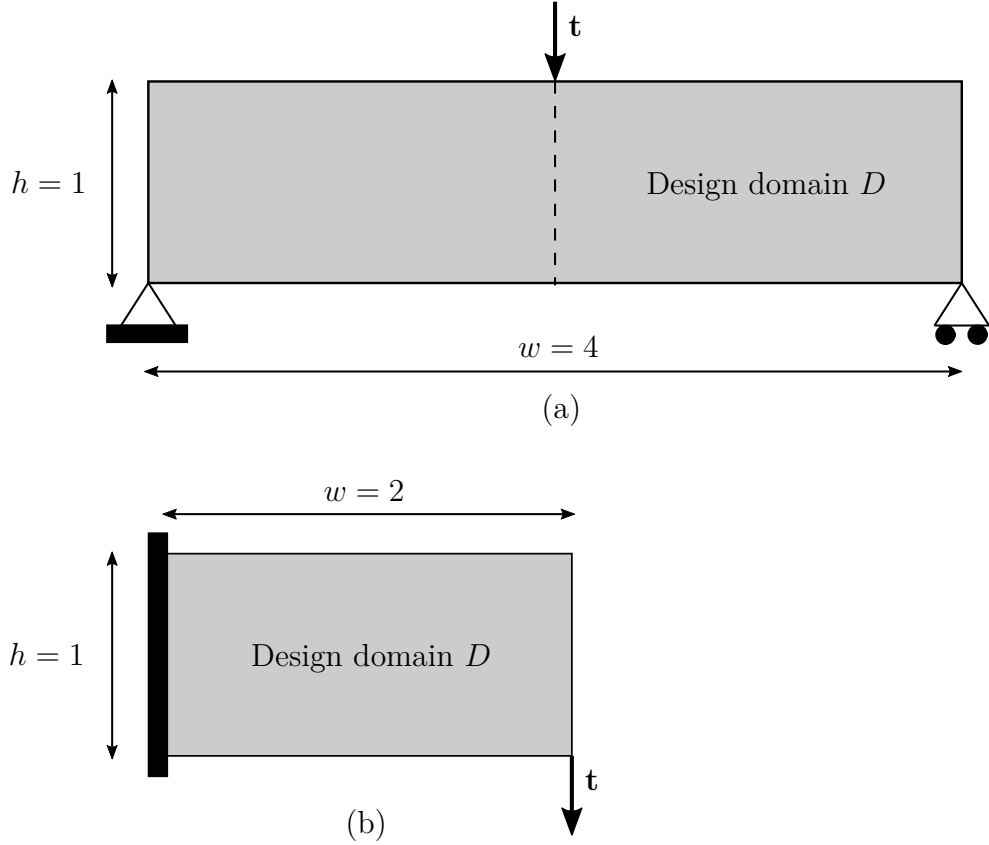


Figure 5.3: Design domain and boundary condition settings for the (a) Messerschmidt-Bölkow-Blohm beam example; (b) cantilever example.

5.5.1 Iterative details: Messerschmidt-Bölkow-Blohm beam

To show the optimization iterative details, the MBB beam example was used. Its design domain D and boundary condition settings are presented in Figure 5.3(a). Only half of the entire domain was optimized due to the symmetry, which was meshed with 100×50 quadrilateral finite elements. A prescribed partitioning cutting plane along the symmetry mid-boundary was assumed. This assumption is required for the appropriate modeling of the maximum build volume constraint, which is also beneficial to enhance the modularity of the optimized multi-component structures. The maximum allowable number of components was set as $K = 3$. The volume fraction constraint limit was set as $V^* = 0.5$. The maximum allowable length and width of the build volume is set as $L^* = 1.5$ and $W^* = 0.6$ respectively. In 2D examples, the constraint on the height limit H^* of the build volume was not needed. Figure 5.4 shows the evolution of the design field during the course of optimization at (a) iteration 1, (b) iteration 35, (c) iteration 80, and (d) iteration 311 (end of optimization). For each iteration, the density field ρ is plotted in the upper middle figure. The

membership field $m^{(k)}$ is plotted in the bottom three figures. By combining both design fields, the overall multi-component topology with intermediate decomposition $\rho \left(\sum_{k=1}^K m^{(k)} \right)$ is plotted in the left figure. At the beginning of optimization, all design fields were uniformly initialized (Figure 5.4(a)). The component decomposition happened when the overall base topology was not yet clear (Figure 5.4(b)). Then, component boundaries started to appear (Figure 5.4(c)), and finally converged at iteration 311 (Figure 5.4(d)).

As seen in Figure 5.4(d), a layer of gray transition zone was formed between component mating boundaries. In the finite element simulation model, smaller Young's moduli were assigned to those elements, which indicated less stiff structural performance than base materials. This behavior was caused by the regularization scheme applied to the membership design field, as explained in Figure 5.5. Based on the PDE filter radius and Heaviside function shape, the gray transition zone would appear surrounding all design field profiles. It is usually not an issue for conventional, single-piece topology optimization because this gray zone will only appear surrounding the overall topology profile, which will not significantly affect the structural performance evaluation. As for MTO, this gray zone also appeared surrounding membership design field profiles, which created gray component mating boundaries in the middle of a multi-component topology assembly. This behavior is actually preferred when a less stiff joining process is to be used to assemble the resulting multi-component structures, e.g., the spot-welding joint as discussed in Chapter 3. As a result, joint locations are somewhat also designed during the course of optimization as the placement of joints in structurally less stiff locations will be discouraged. However, for a more stiff joining process where the joint stiffness is as strong as base materials, such gray zone behavior is not desired. In this case, a continuation scheme can be adopted where the filter radius for the membership design field will be gradually decreased, and the Heaviside function shape will be gradually skewed toward a step function-like shape. Therefore, at the end of optimization, the gray zone between mating component boundaries will become negligibly thin and have little influence on the structural performance evaluation.

Figure 5.6 shows the evolution of manufacturing constraints during the course of optimization. For each iteration, intermediate components $\rho m^{(k)}$ are plotted in the first row. The weighted squared distances $d_j^{(k)}$ in both major and minor directions of bounding boxes are plotted in row 2 and 3 respectively. The last row presents the steady-state temperature distribution $t^{(k)}$ for the elimination of enclosed holes constraint. At the end of optimization, all manufacturing constraints were satisfied.

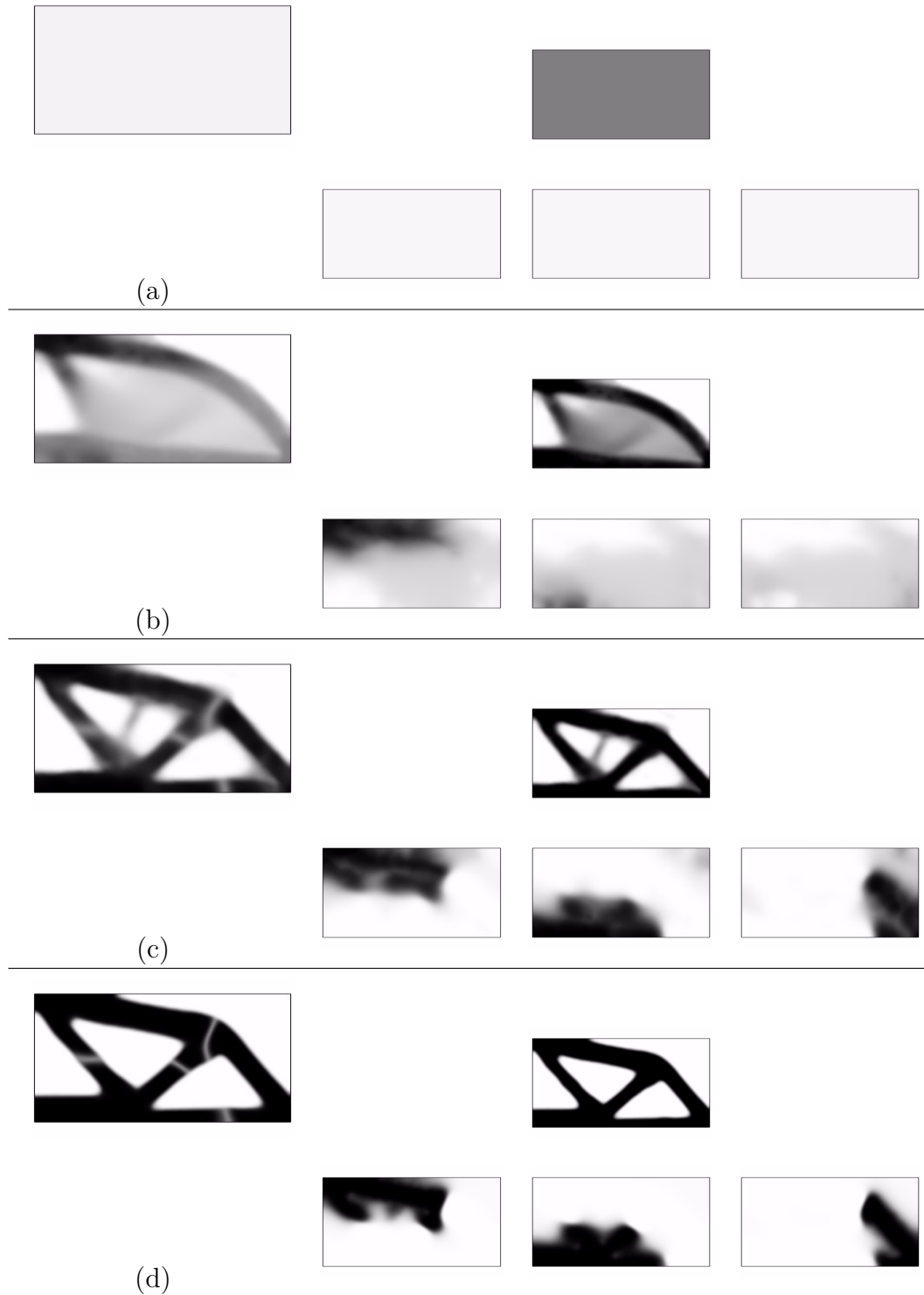


Figure 5.4: Design field iterative details for the Messerschmidt-Bölkow-Blohm beam example at (a) iteration 1; (b) iteration 35; (c) iteration 80; and (d) iteration 311.

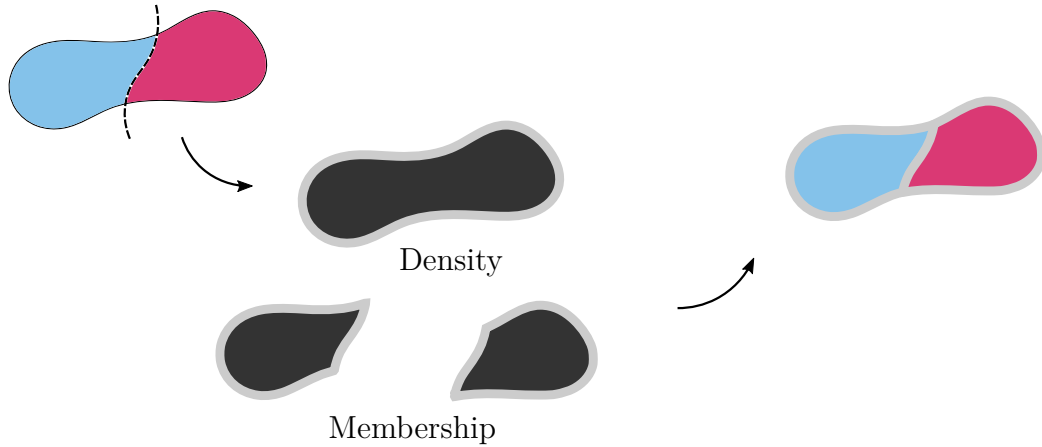


Figure 5.5: Component interface explanation. The gray zone between component boundaries is less stiff than regular base materials in the simulation model. Different colors indicate different components.

Figure 5.7 presents the optimized multi-component topology. Different colors indicate different components, each of which will be produced by a powder-bed additive manufacturing machine. The prescribed, maximum allowable build volume is plotted as dot rectangles. Each component is bounded by the prescribed, maximum allowable bounding box length and width. There are no enclosed holes in any individual component. It is also observed that enclosed holes can appear in the overall multi-component topology, which are acceptable according to the manufacturing constraints, and are indeed preferable in terms of structural performance. Joints are placed at the locations that will satisfy the build volume constraint and the hole constraint. For the sake of maximizing the overall structural stiffness, most joints (with less stiff materials) are placed in locations subject to primarily compression.

5.5.2 Different build volume limits: cantilever

To show the multi-component topologies optimized for different prescribed build volume limits, a cantilever example was used. Its design domain D and boundary condition settings are presented in Figure 5.3(b). The design domain was meshed with 100×50 quadrilateral finite elements. The maximum allowable number of components was set as $K = 4$. The volume fraction constraint limit was set as $V^* = 0.5$. The continuation scheme as described in Section 5.5.1 was applied to minimize the less stiff joint effect on the overall structural performance.

Figure 5.8 presents four designs with different prescribed build volume limits. Their maximum allowable build volume (defined as rectangles in this 2D example)

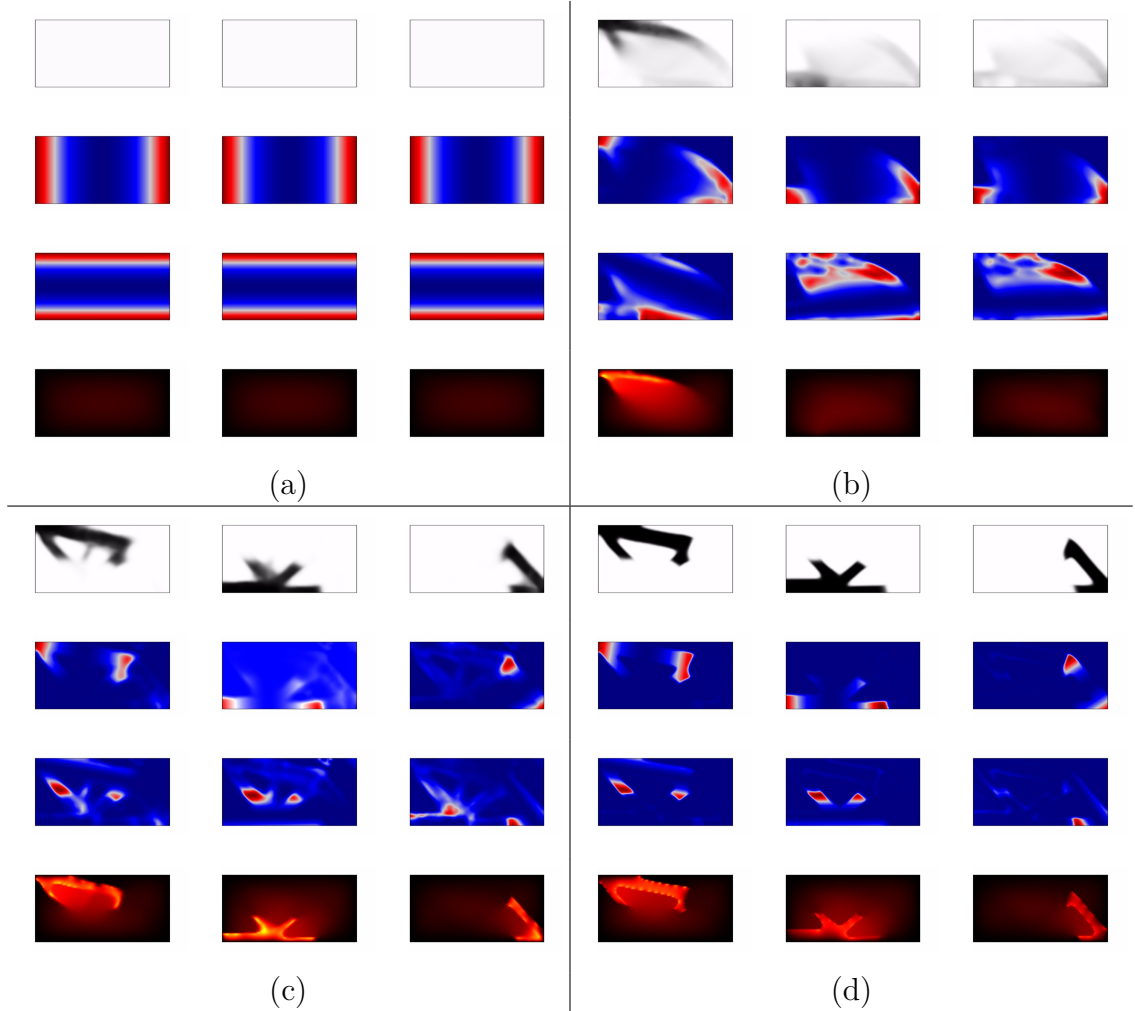


Figure 5.6: Manufacturing constraint iterative details for the Messerschmidt-Bölkow-Blohm beam example at (a) Iteration 1; (b) iteration 35; (c) iteration 80; and (d) iteration 311.

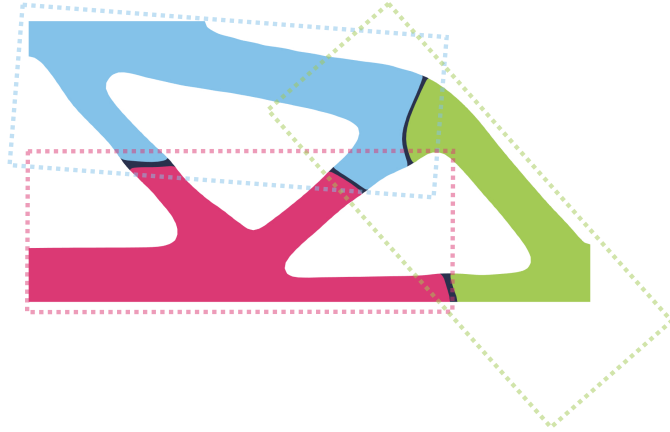


Figure 5.7: The optimized multi-component topology for the MBB beam example. The prescribed, maximum allowable build volume is plotted for each component. Different colors indicate different components.

is presented in Figure 5.8(e). Topology 5.8(a) was generated by conventional, single-piece topology optimization where a rectangle in the size of its initial design domain (2 by 1) was needed to cover the entire geometry. By prescribing the maximum allowable build volume as $L^* = 1.5$ and $W^* = 0.6$, a three-component topology 5.8(b) was obtained. The outcome number of components was less than the maximum number allowed as one of the components becomes unused. It demonstrated the robustness of the formulation that the outcome number of components could converge to a number different from the prescribed K . This was not the case for topology 5.8(c) where the prescribed build volume was too small to have a three-component design with good structural performance. Therefore, a four-component design was generated with the prescribed limit set as $L^* = 1.0$ and $W^* = 0.4$. Finally, a narrow build volume was set as $L^* = 2.5$ and $W^* = 0.3$ for the case 5.8(d). For all multi-component designs 5.8(b-d), there were no enclosed holes in any decomposed component. However, the conventional, single-piece design 5.8(a) had four enclosed holes, which did not satisfy the powder-bed additive manufacturing constraints. The four designs had different base topologies in order to satisfy the corresponding prescribed build volume limits while maximizing their structural performance.

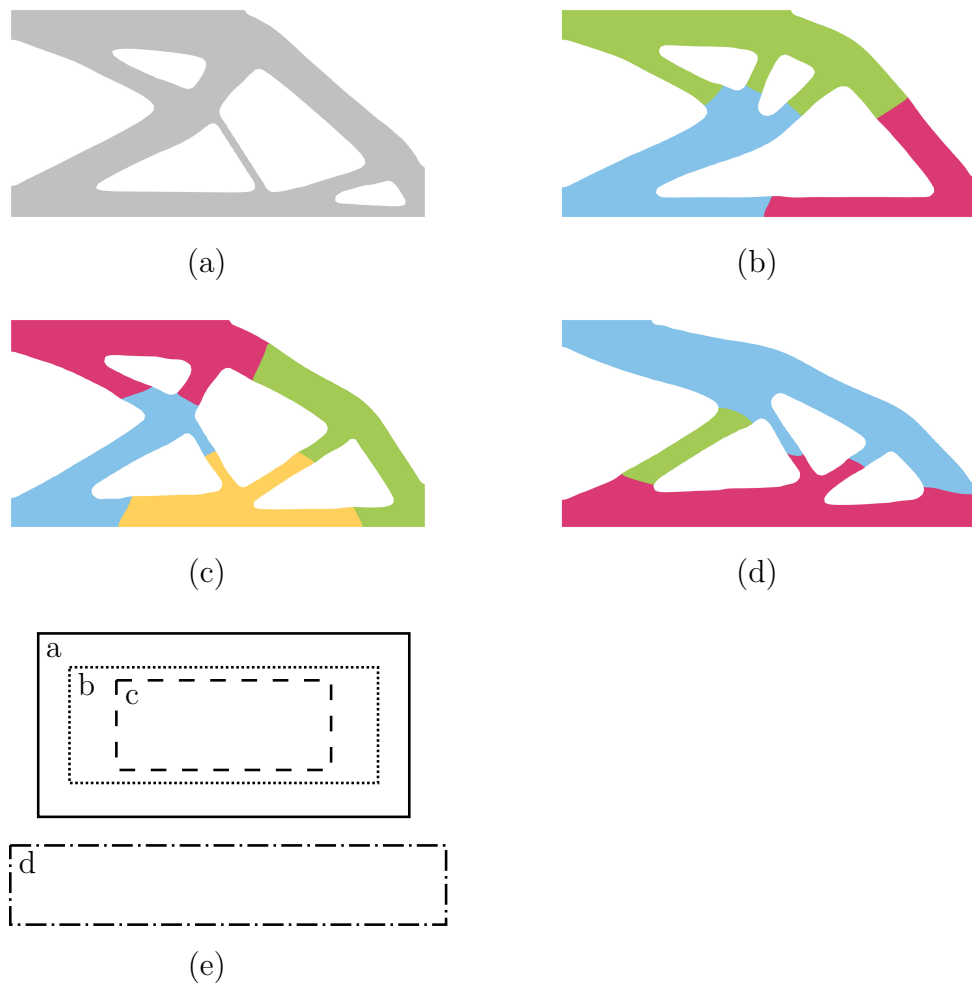


Figure 5.8: The optimized topologies for the cantilever example with different prescribed maximum allowable build volume: (a) 2.0×1.0 ; (b) 1.5×0.6 ; (c) 1.0×0.4 ; (d) 2.5×0.3 ; (e) the prescribed maximum allowable build volume for (a-d).

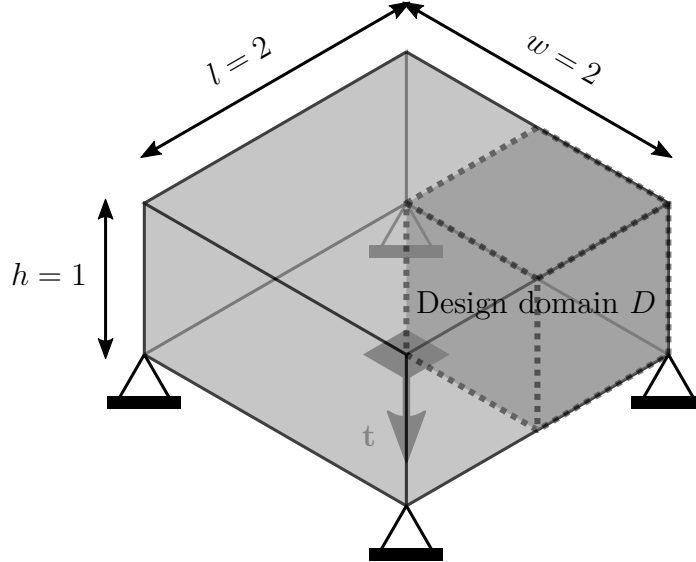


Figure 5.9: Design domain and boundary condition settings for the 3D simply-supported center loading example.

5.5.3 3D example: simply-supported center loading

To show the proposed MTO-A method applied to a 3D problem, a simply-supported center loading example is used. Its design domain and boundary condition settings are presented in Figure 5.9. The maximum allowable number of components was set as $K = 3$. The volume fraction constraint limit was set as $V^* = 0.3$. For comparison, conventional topology optimization (without manufacturing constraints) was used to generate the single-piece result, as shown in Figure 5.10. Due to the symmetry, only the quarter design domain D (denoted as a dot cube in Figure 5.9) was optimized. The quarter design domain was meshed with $30 \times 30 \times 30$ hexahedron finite elements. An enclosed hole was generated in the middle of the optimized structure. According to the powder-bed additive manufacturing constraint, un-melted powders will be trapped inside, and cannot be removed from the component once it is built. It has also previously been reported that for ultra-high resolution topology optimization results, many local hollow features can be generated [122]. The build volume required for this part is equal to its initial design domain bounding box in the size of $2 \times 2 \times 1$. The multi-component topology shown in Figure 5.11 was optimized in the full $2 \times 2 \times 1$ domain without applying any symmetry boundary conditions. The entire domain was meshed with $30 \times 30 \times 15$ hexahedron finite elements. A smaller and narrow rectangular build volume limit of $L^* = 3.0$, $W^* = 1.2$, and $H^* = 0.8$ was specified. By slicing the larger blue component, it can be seen that there is no enclosed hole

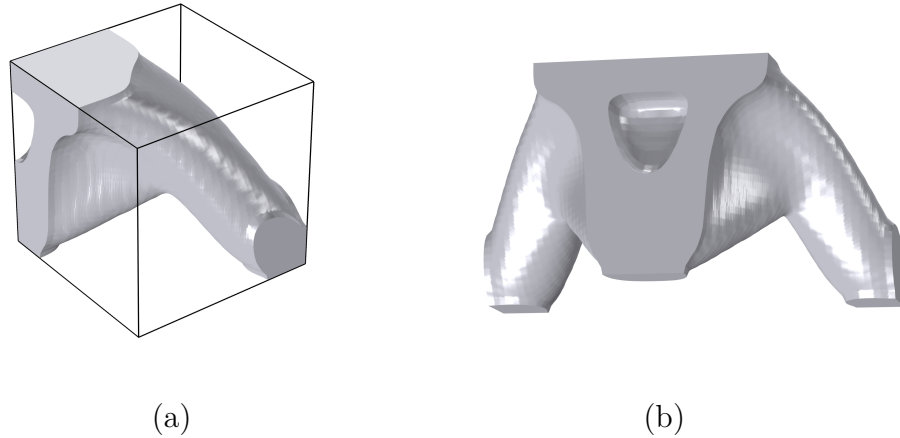


Figure 5.10: The conventional, single-piece optimized topology for the 3D simply-supported center loading example without applying manufacturing constraints. (a) The quarter domain optimized structure; (b) the mirrored half domain structure.

inside. Therefore, its overall base topology is different from that of the single-piece topology in order to satisfy the prescribed build volume limit and elimination of enclosed holes manufacturing constraints.

5.6 Chapter summary

This chapter presented the MTO application for structures assembled from components produced by powder bed additive manufacturing. The weighted principal component analysis was adopted to bound the size of each component to be kept within the prescribed build volume limit. To avoid the formation of holes enclosed within each component, the modified virtual temperature method was implemented. The minimum length scale was controlled by the design field regularization.

Another well-studied manufacturing constraint for additive manufacturing is the control of overhang features. The integration of this constraint into conventional, single-piece topology optimization has been well studied (e.g., [48, 49, 50, 51, 52, 53, 54]). The constraint on overhangs was not included in this chapter, because for powder bed processes, loose powders can support overhang features while printing. The overhang consideration for the multi-component topology design is left for future research. However, it is expected that the MTO concept discussed in this dissertation will be beneficial even for wire-fed additive manufacturing processes where the overhang design is critical, since the multiple build directions allowed in a multi-

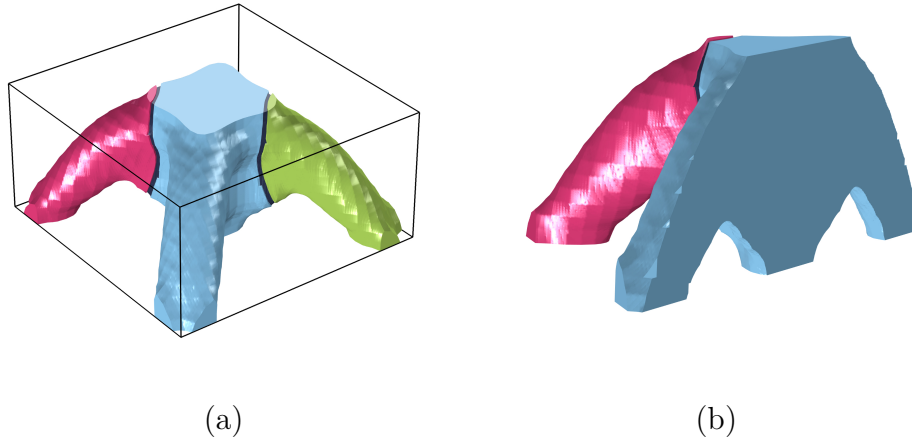


Figure 5.11: The full domain optimized multi-component topology for the 3D simply-supported center loading example with manufacturing constraints. (a) The full domain optimized multi-component structure; (b) the sliced half domain multi-component structure.

component design can largely relax the design space compared with existing methods assuming only a single build direction.

The design field regularization of MTO-A followed that of MTO-C with the Helmholtz PDE filter and Heaviside projection. However, to ensure the membership unity, unlike in MTO-C where the cube-to-simplex projection was used, this chapter used the DMO method. DMO is a widely-accepted method for multi-material topology optimization. The successful use of DMO to an MTO problem somewhat proved that they indeed share a similar mathematical root.

Several 2D examples and the first reported 3D example of MTO were presented to demonstrate the MTO-A method.

CHAPTER 6

Summary

6.1 Dissertation conclusion

This dissertation proposed a continuously relaxed gradient-based formulation for MTO. The conventional density-based representation was used to relax the overall topology design. The concept of fractional memberships was introduced to relax the component decomposition design. Three different methods were implemented to handle the membership unity requirement, which only allows one unique selection of memberships at the end of optimization for each design point. They are the equality constraint method (Chapter 3), the cube-to-simplex projection method (Chapter 4), and the DMO projection method (Chapter 5).

The proposed continuously relaxed gradient-based MTO formulation was applied to designing multi-component structures made by three different manufacturing processes. They are the sheet metal stamping (MTO-S in Chapter 3), the composite manufacturing (MTO-C in Chapter 4), and the additive manufacturing (MTO-A in Chapter 5). For each manufacturing process, the corresponding manufacturing constraints were modeled and integrated into the general MTO formulation discussed in Chapter 2.

Several numerical examples were provided, which demonstrated the trade-off between the structural performance and manufacturability. The proposed multi-component concept also showed advantages in further improving the manufacturability of structures designed by topology optimization. Because most existing topology optimization methods assumed that the outcome optimized structures would be produced as a single piece.

6.2 Contributions

This dissertation covers a multidisciplinary research topic between topology optimization and design for manufacturability. Its contributions can be summarized in two folds.

- A continuously relaxed gradient-based formulation for MTO was proposed. Prior MTO methods were limited to discrete formulations solved by genetic algorithms (e.g., [83, 84, 85]). Due to the use of efficient gradient-based optimization enabled by the proposed continuous MTO formulation, scalable multi-component topology design solutions became possible.
- In addition to the stamping process that has been investigated extensively in previous MTO research (e.g., [79, 83, 84, 85]), this dissertation expanded the MTO method to composite and additive manufacturing.

The contributions regarding the gradient-based continuous MTO formulation are summarized as follows.

- The concept of fractional memberships was introduced, which made the continuous relaxation of component decomposition possible. (Chapter 2, 3, 4, 5)
- The cube-to-simplex projection and penalization method was proposed to handle the membership unity requirement. (Chapter 4)
- The weighting scheme including both the density and membership design fields was proposed to resolve the challenge of evaluating manufacturing constraints with intermediate “blurry” overall topology and “blurry” component partitioning during the course of optimization. It also enabled the evaluation of manufacturing constraints for each component while existing methods only applied manufacturing constraints to the overall topology. (Chapter 3, 4, 5)
- An explicit mesh-dependent joint stiffness model was proposed based on the continuously relaxed design fields. (Chapter 3)
- An implicit mesh-independent component interface identification phenomenon was observed and explained. This can be the foundation for the mesh-independent joint stiffness model. (Chapter 5)
- As a result of the continuous relaxation, the manufacturability-driven MTO problem was, for the first time, solved by efficient gradient-based optimization. (Chapter 3, 4, 5)

The contributions regarding the expansion of the MTO method to different manufacturing processes are summarized as follows.

- A weighted principal component analysis was proposed to determine the orientation of a component bounding box for MTO, which was the key to the stamping die-set material cost modeling, and the additive manufacturing build volume constraint modeling. (Chapter 3, 5)
- The MTO-C method enabled the design of anisotropic multi-component composite structures. The component-wise anisotropic material orientation design was achieved. The outcome design solutions are unique and cannot be obtained by existing anisotropic topology optimization methods. It is most suitable for economical production with the conventional high-volume composite manufacturing processes. (Chapter 4)
- The MTO-A method enabled the design of additively manufactured structures larger than the printer’s build volume for powder bed additive manufacturing. Prior methods were limited to single-piece topology designs smaller than the printer’s build volume. (Chapter 5)

6.3 Future research

To further refine the proposed gradient-based continuous MTO formulation, the following immediate improvements are suggested.

- Joint stiffness specification for the mesh-independent MTO formulation
Though the joint stiffness specification can be prescribed for the mesh-dependent MTO formulation as discussed in Chapter 3, it is not the case for the mesh-independent MTO formulation, as discussed in Chapter 4 and 5. The current mesh-independent formulation only takes the option of either considering less stiff joints or assuming perfect bonding. Future research can follow the observation, briefly discussed in Chapter 5, that intermediate component boundaries (= joint locations) are automatically identified in the regularized membership field.
- Strength-based joint modeling
The proposed joint models in this dissertation will not be directly applicable for stress and fatigue problems. Interested readers are referred to [123] for an example of strength-based joint modeling in a level-set and XFEM framework.

- Stress-based multi-component topology optimization

This dissertation only discussed the stiffness-based structural design. However, the stress-based structural design is critical for certain applications.

- Elimination of disconnected components in each membership phase

The current MTO formulation does not have a mechanism to discourage the appearance of disconnected components to appear in a single membership phase. However, this is not always an issue. For example, in MTO-C, if two disconnected components appeared in one membership phase, they would just have the same material orientation. In MTO-A, if several disconnected components appeared in one membership phase, they would still be produced in a powder bed machine at the same time, and would not violate the build volume limit. For some other manufacturing constraints, however, a single component for each membership phase may be required.

To further expand the scope of MTO, the following future research topics are suggested.

- The extension of MTO to other manufacturing processes

One immediate possible extension is the wire-fed additive manufacturing, which will allow multiple flexible build directions to eliminate overhangs.

- The extension of MTO to incorporate material and process selections

This dissertation assumes a single manufacturing process and a single material for all components. In light of the recent emphasis on the high-performance, lightweight structures integrating multiple materials, the design synthesis of Multi-component Multi-material Multi-process Topology Optimization (M3TO) would be of great interests. The outcome of M3TO is expected to be an assembly of multiple components with different materials each of which is optimized for a certain manufacturing process.

- The implementation of MTO in an ultra-high resolution and fully parallel topology optimization framework

From the prior non-gradient discrete formulation to a continuously relaxed gradient-based formulation, this dissertation has taken a significant step in the right direction for MTO to be used for real-world scalable structural system designs. The next step is to enable the use of high performance computing

and parallel computing. Interested readers are referred to [122] for an example parallel topology optimization framework.

BIBLIOGRAPHY

- [1] Toyota. How many parts is each car made of. <http://www.toyota.co.jp/en/kids/faq/d/01/04/>. Online; accessed: 10-March-2018.
- [2] Boeing. A world of service for the boeing 737. <http://boeing.mediaroom.com/2003-04-15-A-World-of-Service-for-the-Boeing-737>. Online; accessed: 10-March-2018.
- [3] Scholastic. Unearthing dinosaur bones and fossils. <https://www.scholastic.com/teachers/articles/teaching-content/unearthing-dinosaur-bones-and-fossils/>. Online; accessed: 10-March-2018.
- [4] Bendsøe, M. P., and Sigmund, O., 2004. topology optimization theory, methods, and applications. Springer.
- [5] Cheng, K.-T., and Olhoff, N., 1981. “An investigation concerning optimal design of solid elastic plates”. *International Journal of Solids and Structures*, 17(3), pp. 305–323.
- [6] Bendsøe, M. P., and Kikuchi, N., 1988. “Generating optimal topologies in structural design using a homogenization method”. *Computer methods in applied mechanics and engineering*, 71(2), pp. 197–224.
- [7] Bendsøe, M. P., 1989. “Optimal shape design as a material distribution problem”. *Structural and multidisciplinary optimization*, 1(4), pp. 193–202.
- [8] Rozvany, G. I., Zhou, M., and Birker, T., 1992. “Generalized shape optimization without homogenization”. *Structural and Multidisciplinary Optimization*, 4(3), pp. 250–252.
- [9] Xie, Y. M., and Steven, G. P., 1993. “A simple evolutionary procedure for structural optimization”. *Computers & structures*, 49(5), pp. 885–896.
- [10] Sokolowski, J., and Zochowski, A., 1999. “On the topological derivative in shape optimization”. *SIAM journal on control and optimization*, 37(4), pp. 1251–1272.
- [11] Sethian, J. A., and Wiegmann, A., 2000. “Structural boundary design via level set and immersed interface methods”. *Journal of computational physics*, 163(2), pp. 489–528.

- [12] Wang, M. Y., Wang, X., and Guo, D., 2003. “A level set method for structural topology optimization”. *Computer methods in applied mechanics and engineering*, 192(1-2), pp. 227–246.
- [13] Allaire, G., Jouve, F., and Toader, A.-M., 2004. “Structural optimization using sensitivity analysis and a level-set method”. *Journal of computational physics*, 194(1), pp. 363–393.
- [14] Chapman, C. D., Saitou, K., and Jakiela, M. J., 1994. “Genetic algorithms as an approach to configuration and topology design”. *Journal of mechanical design*, 116(4), pp. 1005–1012.
- [15] Hajela, P., and Lee, E., 1995. “Genetic algorithms in truss topological optimization”. *International journal of solids and structures*, 32(22), pp. 3341–3357.
- [16] Guo, X., Zhang, W., and Zhong, W., 2014. “Doing topology optimization explicitly and geometrically—a new moving morphable components based framework”. *Journal of Applied Mechanics*, 81(8), p. 081009.
- [17] Eschenauer, H. A., and Olhoff, N., 2001. “Topology optimization of continuum structures: a review”. *Applied Mechanics Reviews*, 54(4), pp. 331–390.
- [18] Rozvany, G. I., 2009. “A critical review of established methods of structural topology optimization”. *Structural and Multidisciplinary Optimization*, 37(3), pp. 217–237.
- [19] Sigmund, O., and Maute, K., 2013. “Topology optimization approaches”. *Structural and Multidisciplinary Optimization*, 48(6), pp. 1031–1055.
- [20] Deaton, J. D., and Grandhi, R. V., 2014. “A survey of structural and multidisciplinary continuum topology optimization: post 2000”. *Structural and Multidisciplinary Optimization*, 49(1), pp. 1–38.
- [21] Sigmund, O., 2011. “On the usefulness of non-gradient approaches in topology optimization”. *Structural and Multidisciplinary Optimization*, 43(5), pp. 589–596.
- [22] Alexandersen, J., Sigmund, O., and Aage, N., 2016. “Large scale three-dimensional topology optimisation of heat sinks cooled by natural convection”. *International Journal of Heat and Mass Transfer*, 100, pp. 876–891.
- [23] Dilgen, C. B., Dilgen, S. B., Fuhrman, D. R., Sigmund, O., and Lazarov, B. S., 2018. “Topology optimization of turbulent flows”. *Computer Methods in Applied Mechanics and Engineering*, 331, pp. 363–393.
- [24] Nomura, T., Sato, K., Taguchi, K., Kashiwa, T., and Nishiwaki, S., 2007. “Structural topology optimization for the design of broadband dielectric resonator antennas using the finite difference time domain technique”. *International Journal for Numerical Methods in Engineering*, 71(11), pp. 1261–1296.

- [25] Stromberg, L. L., Beghini, A., Baker, W. F., and Paulino, G. H., 2011. “Application of layout and topology optimization using pattern gradation for the conceptual design of buildings”. *Structural and Multidisciplinary Optimization*, 43(2), pp. 165–180.
- [26] Sardan, O., Eichhorn, V., Petersen, D., Fatikow, S., Sigmund, O., and Bøggild, P., 2008. “Rapid prototyping of nanotube-based devices using topology-optimized microgrippers”. *Nanotechnology*, 19(49), p. 495503.
- [27] Diaz, A., and Sigmund, O., 1995. “Checkerboard patterns in layout optimization”. *Structural and Multidisciplinary Optimization*, 10(1), pp. 40–45.
- [28] Haber, R. B., Jog, C. S., and Bendsøe, M. P., 1996. “A new approach to variable-topology shape design using a constraint on perimeter”. *Structural and Multidisciplinary Optimization*, 11(1), pp. 1–12.
- [29] Sigmund, O., 1997. “On the design of compliant mechanisms using topology optimization”. *Journal of Structural Mechanics*, 25(4), pp. 493–524.
- [30] Bruns, T. E., and Tortorelli, D. A., 2001. “Topology optimization of non-linear elastic structures and compliant mechanisms”. *Computer Methods in Applied Mechanics and Engineering*, 190(26), pp. 3443–3459.
- [31] Bourdin, B., 2001. “Filters in topology optimization”. *International Journal for Numerical Methods in Engineering*, 50(9), pp. 2143–2158.
- [32] Sigmund, O., 2007. “Morphology-based black and white filters for topology optimization”. *Structural and Multidisciplinary Optimization*, 33(4-5), pp. 401–424.
- [33] Niordson, F., 1983. “Optimal design of elastic plates with a constraint on the slope of the thickness function”. *International Journal of Solids and Structures*, 19(2), pp. 141–151.
- [34] Ambrosio, L., and Buttazzo, G., 1993. “An optimal design problem with perimeter penalization”. *Calculus of Variations and Partial Differential Equations*, 1(1), pp. 55–69.
- [35] Petersson, J., and Sigmund, O., 1998. “Slope constrained topology optimization”. *International Journal for Numerical Methods in Engineering*, 41(8), pp. 1417–1434.
- [36] Zhou, M., Shyy, Y., and Thomas, H., 2001. “Checkerboard and minimum member size control in topology optimization”. *Structural and Multidisciplinary Optimization*, 21(2), pp. 152–158.
- [37] Lazarov, B. S., and Sigmund, O., 2011. “Filters in topology optimization based on Helmholtz-type differential equations”. *International Journal for Numerical Methods in Engineering*, 86(6), pp. 765–781.

- [38] Kawamoto, A., Matsumori, T., Yamasaki, S., Nomura, T., Kondoh, T., and Nishiwaki, S., 2011. “Heaviside projection based topology optimization by a PDE-filtered scalar function”. *Structural and Multidisciplinary Optimization*, 44(1), pp. 19–24.
- [39] Zhou, M., Fleury, R., Shyy, Y.-K., Thomas, H., and Brennan, J., 2002. “Progress in topology optimization with manufacturing constraints”. In 9th AIAA/ISSMO Symposium on Multidisciplinary Analysis and Optimization, p. 5614.
- [40] Xia, Q., Shi, T., Wang, M. Y., and Liu, S., 2010. “A level set based method for the optimization of cast part”. *Structural and Multidisciplinary Optimization*, 41(5), pp. 735–747.
- [41] Allaire, G., Jouve, F., and Michailidis, G., 2016. “Molding direction constraints in structural optimization via a level-set method”. In *Variational Analysis and Aerospace Engineering*. Springer, pp. 1–39.
- [42] Sato, Y., Yamada, T., Izui, K., and Nishiwaki, S., 2017. “Manufacturability evaluation for molded parts using fictitious physical models, and its application in topology optimization”. *The International Journal of Advanced Manufacturing Technology*, 92(1-4), pp. 1391–1409.
- [43] Li, Q., Chen, W., Liu, S., and Fan, H., 2018. “Topology optimization design of cast parts based on virtual temperature method”. *Computer-Aided Design*, 94, pp. 28–40.
- [44] Li, H., Li, P., Gao, L., Zhang, L., and Wu, T., 2015. “A level set method for topological shape optimization of 3d structures with extrusion constraints”. *Computer Methods in Applied Mechanics and Engineering*, 283, pp. 615–635.
- [45] Zhang, S., Norato, J. A., Gain, A. L., and Lyu, N., 2016. “A geometry projection method for the topology optimization of plate structures”. *Structural and Multidisciplinary Optimization*, 54(5), pp. 1173–1190.
- [46] Zhang, S., Gain, A. L., and Norato, J. A., 2017. “Stress-based topology optimization with discrete geometric components”. *Computer Methods in Applied Mechanics and Engineering*, 325, pp. 1–21.
- [47] Zhou, Y., and Saitou, K., 2017. “Topology optimization of composite structures with data-driven resin filling time manufacturing constraint”. *Structural and Multidisciplinary Optimization*, 55(6), pp. 2073–2086.
- [48] Gaynor, A. T., and Guest, J. K., 2016. “Topology optimization considering overhang constraints: Eliminating sacrificial support material in additive manufacturing through design”. *Structural and Multidisciplinary Optimization*, 54(5), pp. 1157–1172.

- [49] Langelaar, M., 2016. “Topology optimization of 3d self-supporting structures for additive manufacturing”. *Additive Manufacturing*, 12, pp. 60–70.
- [50] Mirzendehtel, A. M., and Suresh, K., 2016. “Support structure constrained topology optimization for additive manufacturing”. *Computer-Aided Design*, 81, pp. 1–13.
- [51] Driessen, A., 2016. “Overhang constraint in topology optimisation for additive manufacturing: A density gradient based approach”. Master’s thesis, Delft University of Technology.
- [52] Qian, X., 2017. “Undercut and overhang angle control in topology optimization: A density gradient based integral approach”. *International Journal for Numerical Methods in Engineering*, 111(3), pp. 247–272.
- [53] Langelaar, M., 2017. “An additive manufacturing filter for topology optimization of print-ready designs”. *Structural and Multidisciplinary Optimization*, 55(3), pp. 871–883.
- [54] Guo, X., Zhou, J., Zhang, W., Du, Z., Liu, C., and Liu, Y., 2017. “Self-supporting structure design in additive manufacturing through explicit topology optimization”. *Computer Methods in Applied Mechanics and Engineering*, 323, pp. 27–63.
- [55] Liu, S., Li, Q., Chen, W., Tong, L., and Cheng, G., 2015. “An identification method for enclosed voids restriction in manufacturability design for additive manufacturing structures”. *Frontiers of Mechanical Engineering*, 10(2), pp. 126–137.
- [56] Li, Q., Chen, W., Liu, S., and Tong, L., 2016. “Structural topology optimization considering connectivity constraint”. *Structural and Multidisciplinary Optimization*, 54(4), pp. 971–984.
- [57] Wu, J., Clausen, A., and Sigmund, O., 2017. “Minimum compliance topology optimization of shell–infill composites for additive manufacturing”. *Computer Methods in Applied Mechanics and Engineering*, 326, pp. 358–375.
- [58] Wu, J., Aage, N., Westermann, R., and Sigmund, O., 2018. “Infill optimization for additive manufacturing—approaching bone-like porous structures”. *IEEE transactions on visualization and computer graphics*, 24(2), pp. 1127–1140.
- [59] Liu, J., and Ma, Y., 2016. “A survey of manufacturing oriented topology optimization methods”. *Advances in Engineering Software*, 100, pp. 161–175.
- [60] Vatanabe, S. L., Lippi, T. N., de Lima, C. R., Paulino, G. H., and Silva, E. C., 2016. “Topology optimization with manufacturing constraints: A unified projection-based approach”. *Advances in Engineering Software*, 100, pp. 97–112.

- [61] Wang, M. Y., and Wang, X., 2004. ““Color” level sets: a multi-phase method for structural topology optimization with multiple materials”. *Computer Methods in Applied Mechanics and Engineering*, 193(6), pp. 469–496.
- [62] Stegmann, J., and Lund, E., 2005. “Discrete material optimization of general composite shell structures”. *International Journal for Numerical Methods in Engineering*, 62(14), pp. 2009–2027.
- [63] Zuo, W., and Saitou, K., 2017. “Multi-material topology optimization using ordered SIMP interpolation”. *Structural and Multidisciplinary Optimization*, 55(2), pp. 477–491.
- [64] Zhang, X. S., Paulino, G. H., and Ramos, A. S., 2017. “Multi-material topology optimization with multiple volume constraints: a general approach applied to ground structures with material nonlinearity”. *Structural and Multidisciplinary Optimization*, pp. 1–22.
- [65] Da, D., Cui, X., Long, K., and Li, G., 2017. “Concurrent topological design of composite structures and the underlying multi-phase materials”. *Computers & Structures*, 179, pp. 1–14.
- [66] Liu, J., and Ma, Y., 2018. “A new multi-material level set topology optimization method with the length scale control capability”. *Computer Methods in Applied Mechanics and Engineering*, 329, pp. 444–463.
- [67] Qian, Z., and Ananthasuresh, G., 2004. “Optimal embedding of rigid objects in the topology design of structures”. *Mechanics Based Design of Structures and Machines*, 32(2), pp. 165–193.
- [68] Zhu, J., Zhang, W., Beckers, P., Chen, Y., and Guo, Z., 2008. “Simultaneous design of components layout and supporting structures using coupled shape and topology optimization technique”. *Structural and Multidisciplinary Optimization*, 36(1), pp. 29–41.
- [69] Zhu, J., Zhang, W., and Beckers, P., 2009. “Integrated layout design of multi-component system”. *International journal for numerical methods in engineering*, 78(6), pp. 631–651.
- [70] Xia, L., Zhu, J., Zhang, W., and Breitkopf, P., 2013. “An implicit model for the integrated optimization of component layout and structure topology”. *Computer Methods in Applied Mechanics and Engineering*, 257, pp. 87–102.
- [71] Wang, Y., Luo, Z., Zhang, X., and Kang, Z., 2014. “Topological design of compliant smart structures with embedded movable actuators”. *Smart Materials and Structures*, 23(4), p. 045024.
- [72] Gao, H.-H., Zhu, J.-H., Zhang, W.-H., and Zhou, Y., 2015. “An improved adaptive constraint aggregation for integrated layout and topology optimization”. *Computer Methods in Applied Mechanics and Engineering*, 289, pp. 387–408.

- [73] Kang, Z., Wang, Y., and Wang, Y., 2016. “Structural topology optimization with minimum distance control of multiphase embedded components by level set method”. *Computer Methods in Applied Mechanics and Engineering*, 306, pp. 299–318.
- [74] Johanson, R., Kikuchi, N., and Papalambros, P., 1994. “Simultaneous topology and material microstructure design”. *Advances in Structural Optimization*, pp. 143–149.
- [75] Chickermane, H., and Gea, H., 1997. “Design of multi-component structural systems for optimal layout topology and joint locations”. *Engineering with Computers*, 13(4), pp. 235–243.
- [76] Jiang, T., and Chirehdast, M., 1997. “A systems approach to structural topology optimization: designing optimal connections”. *Journal of Mechanical Design*, 119(1), pp. 40–47.
- [77] Li, Q., Steven, G. P., and Xie, Y., 2001. “Evolutionary structural optimization for connection topology design of multi-component systems”. *Engineering Computations*, 18(3/4), pp. 460–479.
- [78] Yetis, F. A., and Saitou, K., 2002. “Decomposition-based assembly synthesis based on structural considerations”. *Journal of Mechanical Design*, 124(4), pp. 593–601.
- [79] Lyu, N., and Saitou, K., 2003. “Decomposition-based assembly synthesis for structural stiffness”. *Journal of Mechanical Design*, 125(3), pp. 452–463.
- [80] Cetin, O. L., and Saitou, K., 2004. “Decomposition-based assembly synthesis for maximum structural strength and modularity”. *Journal of Mechanical Design*, 126(2), pp. 244–253.
- [81] Lyu, N., and Saitou, K., 2005. “Decomposition-based assembly synthesis of a three-dimensional body-in-white model for structural stiffness”. *Journal of mechanical design*, 127(1), pp. 34–48.
- [82] Lyu, N., and Saitou, K., 2006. “Decomposition-based assembly synthesis of space frame structures using joint library”. *Journal of Mechanical Design*, 128(1), pp. 57–65.
- [83] Lyu, N., and Saitou, K., 2005. “Topology optimization of multicomponent beam structure via decomposition-based assembly synthesis”. *Journal of Mechanical Design*, 127(2), pp. 170–183.
- [84] Yildiz, A. R., and Saitou, K., 2011. “Topology synthesis of multicomponent structural assemblies in continuum domains”. *Journal of Mechanical Design*, 133(1), p. 011008.

- [85] Guirguis, D., Hamza, K., Aly, M., Hegazi, H., and Saitou, K., 2015. “Multi-objective topology optimization of multi-component continuum structures via a kriging-interpolated level set approach”. *Structural and Multidisciplinary Optimization*, 51(3), pp. 733–748.
- [86] Boothroyd, G., Dewhurst, P., and Knight, W. A., 2010. *Product design for manufacture and assembly*. CRC Press.
- [87] Hvejsel, C. F., and Lund, E., 2011. “Material interpolation schemes for unified topology and multi-material optimization”. *Structural and Multidisciplinary Optimization*, 43(6), pp. 811–825.
- [88] Kennedy, G. J., and Martins, J. R., 2013. “A laminate parametrization technique for discrete ply-angle problems with manufacturing constraints”. *Structural and Multidisciplinary Optimization*, 48(2), pp. 379–393.
- [89] Malen, D. E., 2011. *Fundamentals of automobile body structure design*. Society of Automotive Engineers.
- [90] O’Rourke, J., 1985. “Finding minimal enclosing boxes”. *International Journal of Computer & Information Sciences*, 14(3), pp. 183–199.
- [91] Barequet, G., and Har-Peled, S., 2001. “Efficiently approximating the minimum-volume bounding box of a point set in three dimensions”. *Journal of Algorithms*, 38(1), pp. 91–109.
- [92] Chan, C., and Tan, S., 2001. “Determination of the minimum bounding box of an arbitrary solid: an iterative approach”. *Computers & Structures*, 79(15), pp. 1433–1449.
- [93] Dimitrov, D., Knauer, C., Kriegel, K., and Rote, G., 2009. “Bounds on the quality of the pca bounding boxes”. *Computational Geometry*, 42(8), pp. 772–789.
- [94] Le Riche, R., and Haftka, R. T., 1993. “Optimization of laminate stacking sequence for buckling load maximization by genetic algorithm”. *AIAA journal*, 31(5), pp. 951–956.
- [95] Nagendra, S., Jestin, D., Gürdal, Z., Haftka, R. T., and Watson, L. T., 1996. “Improved genetic algorithm for the design of stiffened composite panels”. *Computers & Structures*, 58(3), pp. 543–555.
- [96] Liu, B., Haftka, R. T., Akgün, M. A., and Todoroki, A., 2000. “Permutation genetic algorithm for stacking sequence design of composite laminates”. *Computer Methods in Applied Mechanics and Engineering*, 186(2), pp. 357–372.
- [97] Haftka, R. T., and Gürdal, Z., 2012. *Elements of structural optimization 3rd edition*, Vol. 11. Springer Science & Business Media.

- [98] Niu, B., Olhoff, N., Lund, E., and Cheng, G., 2010. “Discrete material optimization of vibrating laminated composite plates for minimum sound radiation”. *International Journal of Solids and Structures*, 47(16), pp. 2097–2114.
- [99] Sørensen, S. N., Sørensen, R., and Lund, E., 2014. “DMTO-a method for discrete material and thickness optimization of laminated composite structures”. *Structural and Multidisciplinary Optimization*, 50(1), pp. 25–47.
- [100] Bruyneel, M., 2011. “SFP-a new parameterization based on shape functions for optimal material selection: application to conventional composite plies”. *Structural and Multidisciplinary Optimization*, 43(1), pp. 17–27.
- [101] Gao, T., Zhang, W., and Duysinx, P., 2012. “A bi-value coding parameterization scheme for the discrete optimal orientation design of the composite laminate”. *International Journal for Numerical Methods in Engineering*, 91(1), pp. 98–114.
- [102] Kiyono, C., Silva, E., and Reddy, J., 2017. “A novel fiber optimization method based on normal distribution function with continuously varying fiber path”. *Composite Structures*, 160, pp. 503–515.
- [103] Bruyneel, M., and Fleury, C., 2002. “Composite structures optimization using sequential convex programming”. *Advances in Engineering Software*, 33(7), pp. 697–711.
- [104] Lindgaard, E., and Lund, E., 2011. “Optimization formulations for the maximum nonlinear buckling load of composite structures”. *Structural and Multidisciplinary Optimization*, 43(5), pp. 631–646.
- [105] Nomura, T., Dede, E. M., Lee, J., Yamasaki, S., Matsumori, T., Kawamoto, A., and Kikuchi, N., 2015. “General topology optimization method with continuous and discrete orientation design using isoparametric projection”. *International Journal for Numerical Methods in Engineering*, 101(8), pp. 571–605.
- [106] Gibiansky, L. V., and Sigmund, O., 2000. “Multiphase composites with extremal bulk modulus”. *Journal of the Mechanics and Physics of Solids*, 48(3), pp. 461–498.
- [107] Hull, D., and Clyne, T., 1996. *An introduction to composite materials*. Cambridge university press.
- [108] Hosford, W. F., 2013. *Elementary materials science*. ASM International.
- [109] Svanberg, K., 1987. “The method of moving asymptotes-a new method for structural optimization”. *International Journal for Numerical Methods in Engineering*, 24(2), pp. 359–373.

- [110] Olesen, L. H., Okkels, F., and Bruus, H., 2006. “A high-level programming-language implementation of topology optimization applied to steady-state navier-stokes flow”. *International Journal for Numerical Methods in Engineering*, 65(7), pp. 975–1001.
- [111] Chirehdast, M., Gea, H.-C., Kikuchi, N., and Papalambros, P., 1994. “Structural configuration examples of an integrated optimal design process”. *Journal of Mechanical Design*, 116(4), pp. 997–1004.
- [112] Kumar, A., and Gossard, D., 1996. “Synthesis of optimal shape and topology of structures”. *Journal of Mechanical Design*, 118, pp. 68–74.
- [113] Zegard, T., and Paulino, G. H., 2013. “Toward gpu accelerated topology optimization on unstructured meshes”. *Structural and Multidisciplinary Optimization*, 48(3), pp. 473–485.
- [114] Dede, E. M., Joshi, S. N., and Zhou, F., 2015. “Topology optimization, additive layer manufacturing, and experimental testing of an air-cooled heat sink”. *Journal of Mechanical Design*, 137(11), p. 111403.
- [115] Osanov, M., Carstensen, J. V., Tromme, E., Guest, J. K., and Williams, C., 2016. “Topology optimization for additive manufacturing: new projection-based design algorithms”. In *17th AIAA/ISSMO Multidisciplinary Analysis and Optimization Conference*, p. 3213.
- [116] Zegard, T., and Paulino, G. H., 2016. “Bridging topology optimization and additive manufacturing”. *Structural and Multidisciplinary Optimization*, 53(1), pp. 175–192.
- [117] Zhu, B., Skouras, M., Chen, D., and Matusik, W., 2017. “Two-scale topology optimization with microstructures”. *ACM Transactions on Graphics*, 36(5), p. 164.
- [118] Formlab, 2016. *How to Create Models Larger than Your 3D Printer’s Build Volume*. <https://goo.gl/9mz1Zb>. Online; accessed 24-January-2018.
- [119] Luo, L., Baran, I., Rusinkiewicz, S., and Matusik, W., 2012. “Chopper: partitioning models into 3D-printable parts”. *ACM Transactions on Graphics*, 31(6), Nov., pp. 129:1–129:9.
- [120] Attene, M., 2015. “Shapes in a box: Disassembling 3d objects for efficient packing and fabrication”. *Computer Graphics Forum*, 34(8), pp. 64–76.
- [121] Moon, S. J., and Yoon, G. H., 2013. “A newly developed qp-relaxation method for element connectivity parameterization to achieve stress-based topology optimization for geometrically nonlinear structures”. *Computer Methods in Applied Mechanics and Engineering*, 265, pp. 226–241.

- [122] Aage, N., Andreassen, E., and Lazarov, B. S., 2015. “Topology optimization using petsc: An easy-to-use, fully parallel, open source topology optimization framework”. *Structural and Multidisciplinary Optimization*, 51(3), pp. 565–572.
- [123] Liu, P., Luo, Y., and Kang, Z., 2016. “Multi-material topology optimization considering interface behavior via XFEM and level set method”. *Computer Methods in Applied Mechanics and Engineering*, 308, pp. 113–133.